Ghent University
Faculty of Sciences
Department of Inorganic and Physical Chemistry

New Insights in the Synthesis and Surface Chemistry of Colloidal Quantum Dots

Kim De Nolf

Thesis submitted in fulfillment
of the requirements of the degree of
Doctor in Science: Chemistry
2016

Ghent University
Faculty of Sciences
Department of Inorganic and Physical Chemistry

Promotors	Department
Prof. Dr. Ir. Zeger Hens	Inorganic and Physical Chemistry
Prof. Dr. José C. Martins	Organic en Macromolecular Chemistry

Jury members	Affiliation
Prof. Dr. I. Infante	VU Amsterdam
Prof. Dr. S. De Feyter	KU Leuven
Prof. Dr. Ir. P. Van der Meeren	UGent
Prof. Dr. R. Van Deun	UGent
Prof. Dr. R. Hoogenboom	UGent

This work was realized with the support of
the Research Foundation - Flanders (FWO)

I don't know where I'm going from here,
but I promise it won't be boring.

-

David Bowie

Contents

List of Acronyms

BAc Behenic acid

$Cd(OAc)_2$ Cadmium oleate

COM Center of mass

COSY Correlation spectroscopy

DAc Decanoic acid

$DDNH_2$ Dodecyl amine

DOSY Diffusion ordered spectroscopy

FTIR Fourier transform infrared

$HDNH_2$ Hexadecyl amine

HDA 2-hexyldecanoic acid

HIS Hot injection synthesis

HMBC Heteronuclear multiple-bond correlation

HSQC Heteronuclear single-quantum correlation

LEDs Light emitting diodes

M Monomers

MAc Myristic acid

MS Mass spectrometry

NCs Nanocrystals

NMR Nuclear magnetic resonance spectroscopy

nOe Nuclear Overhauser effect

NOESY Nuclear Overhauser effect spectroscopy

ODNH$_2$ Octadecyl amine

OAc Oleic acid

ODESe 1-octadecene selenium

OlNH$_2$ Oleylamine

P Precursors

PLQY Photoluminescence quantum yield

PTMS Tris(trimethylsilyl) phosphine

QDs Quantum dots

RBS Rutherford backscattering spectrometry

SAM Self-assembled monolayers

TEM Transmission electron microscopy

TDNH$_2$ Tetradecyl amine

TBPO Tri-*n*-butylphosphine oxide

TOCSY Total correlation spectroscopy

TOPSe Trioctylphosphine selenium

TOPO Tri-*n*-octylphosphine oxide

XPS X-ray photoelectron spectroscopy

Nederlandse samenvatting
–Summary in Dutch–

Colloïdale nanokristallen zijn een klasse materialen met een enorm potentieel om de huidige problemen het hoofd te bieden.[1] Het zijn extreem kleine kristallijne deeltjes met een grootte vergelijkbaar aan die van moleculaire clusters en bulk vaste stoffen. Hun toepassingen varïeren van lichtgevende diodes (LED)[2], tot zonnecellen[1] en zelfs fotodetectoren[1]. Halfgeleider nanokristallen worden kwantumstippen genoemd. Deze kwantumstippen hebben unieke elektrische en optische eigenschappen aangezien ze de brug slaan tussen atomen en bulk halfgeleiders in termen van elektronische energieniveaus. Zo zal bijvoorbeeld de absorptie en emissie naar kortere golflengten verschuiven wanneer de grootte van de kwantumstip verkleint. Dit unieke gedrag maakt kwantumstippen extreem nuttig voor allerlei toepassingen.[2;3]

Nanokristallen worden momenteel aangewend als modelsystemen om de eigenschappen van materialen op nanoschaal te onderzoeken en hun nut in een verscheidenheid aan verschillende toepassingen te onderzoeken en te begrijpen. Een controle op de productie van deze colloïdale nanokristallen is hierbij essentieel.

Om controle te verkrijgen over de productie van nanokristallen is de kennis van het reactieproces noodzakelijk. Mechanistische studies spelen daardoor een prominente rol binnen het onderzoeksveld.

- In het eerste hoofdstuk werd de vorming van InP nanokristallen uit de reactie van aminofosfines (tris(diethylamino)fosfine of tris(dimethylamino)fosfine) en een indium halide ($InCl_3$, $InBr_3$ or InI_3) bestudeerd. Deze reactie is niet vanzelfsprekend door het oxidatiegetal van indium en fosfor. De reactie van In^{III} met P^{III} moet voorafgegaan worden

door de reductie van P^{III} naar P^{-III}. Mogelijke intermediaire reacties tijdens de vorming van InP nanokristallen werden onderzocht door de uitstoot van de synthese te schrobben met een oplossing van waterstofchloride in methanol en op te vangen als een zout. Na herkristallisatie in ethylacetaat werd het zout door X-straal diffractie geïdentificeerd als dimethylammonium chloride voor een reactie waarbij tris(dimethylamino)fosfine wordt gebruikt als precursor. Dit resultaat suggereert een uitwisseling tussen de amines die gebruikt werden als solvent en de amino groepen van de originele fosfor precursor. Vervolgens werd dit bevestigd door NMR spectroscopie op $P(NEt_2)_3$ gemengd met dodecylamine onder inerte atmosfeer. De initïele resonantie van $P(NEt_2)_3$ bij 118 ppm verdween bijna volledig door transaminatie na een uur. Nieuwe resonanties bij 111 en 98 ppm, en wat kleinere resonanties rond 11 ppm verschenen. Deze species werden aan een uitgebreide NMR analyse onderworpen om hun identiteit te achterhalen. Daarnaast werd de synthese uitgetest in verschillende solventen. Enkel de reactie in primaire amines leidde tot de vorming van InP nanokristallen.

De InP synthese bereikte volledige conversie in verhouding tot de hoeveelheid indium wanneer de verhouding tussen het aminofosfine en het indium halide 4:1 bereikt. Op dit punt maken we de hypothese dat de fosfor precursor in overmaat nodig is voor een volledige conversie van de reactie omdat het aminofosfine twee rollen speelt tijdens de synthese. De reactievergelijking werd voorgesteld als:

$$InX_3 + 4\,P(NHR)_3 \rightleftharpoons InP + 3\,P(NHR)_4X \qquad (1)$$

In deze vergelijking wordt één aminofosfine gebruikt om de InP eenheid te vormen waarbij het gereduceerd wordt van P^{III} naar P^{-III}. De drie overblijvende aminofosfines dienen als reducerend agens en worden dus omgezet in fosfonium zouten (P^{V}). Een eerste bevestiging van deze voorgestelde reactievergelijking werd gegeven door NMR analyse van reactiefracties die genomen worden in de loop van de synthese. Deze spectra onthullen de vorming van een bijproduct, verschillend van de transaminatieproducten. Dit bijproduct wordt gevormd aan dezelfde snelheid als de InP formatie. Ten tweede werd het geïsoleerd bijproduct geïdentificeerd met massaspectroscopie en NMR als zijnde

het volledig getransamineerde fosfonium zout. Finaal werd een reactiemechanisme voorgesteld. In overeenstemming met de dubbele rol van fosfor gaat dit mechanisme uit van een nucleofiele aanval op het fosfor centrum van één van de aminofosfines. Een adduct van $InCl_3$ en $P(NHR)_3$ wordt gevormd tijdens de eerste stap gezien het volledig getransamineerde $P(NHR)_3$ de enige reactant is. Daarna wordt een nucleofiele aanval gepleegd op het stikstof door een tweede $P(NHR)_3$, wat resulteert in de vorming van een InP-intermediair en een eerste equivalent van het amino fosfine $P(NHR)_4Cl$. Nog twee equivalenten van $P(NHR)_3$ reduceren de fosfor in het intermediair verder wat resulteert in de vorming van één InP eenheid en alles samen drie fosfonium zouten.

- In het tweede hoofdstuk onderzochten we de relatie tussen de ketenlengte van de gebruikte liganden en de grootte van de gevormde CdSe nanokristallen tijdens de hete injectie synthese. Bij twee verschillende CdSe nanokristalsyntheses vonden we consistent dat langere carbonzuren kleinere nanokristallen met kleinere dispersie op de grootte opleveren. In tegenstelling tot het idee dat dit fenomeen afkomstig zou zijn van een vermindering in de reactiesnelheid, toonden wij aan dat de variatie van de ketenlengte de reactiesnelheid onveranderd laat. De snelheid van de nucleatie en groei werd bepaald door de snelheid van monomeervorming. Onder dergelijke condities kon de gewenste grootte van de nanokristallen gemanipuleerd worden door te variëren in het punt waarop de monomeerconsumptie door de groei primeert op de monomeerconsumtie door nucleatie.[4]

  De hamvraag was dus hoe de kentenlengte dit punt van overname kan beïnvloeden. Om deze vraag te beantwoorden startten we van de uitdrukkingen voor de snelheid van nanokristal nucleatie J_N (het aantal gevormde nuclei per seconde) en de nanokristal groei J_G (de verandering in nanokristal diameter per seconde). Beiden hangen af van parameters zoals de diffusie coëfficiënt D van het monomeer, het volume van de monomeer molecule v_0, de oppervlaktespanning γ, het molair volume van het gevormde materiaal V_m, de straal van de nanokristallen r, de snelheidsconstantes k_g^∞ en k_d^∞ voor monomeeradsorptie en -desorptie, de transfer coëfficiënt α voor monomeer adsorptie en de supersaturatie S, die gedefinieerd wordt als de verhouding tussen de

effectieve concentratie en de oplosbaarheid $[M]_0$ van het monomeer.[5]

Door middel van een diepgaand experimenteel onderzoek werd de relatie tussen de ketenlengte en de grootte van het nanokistal bepaald. Eerst werd de hoeveelheid oliezuur in stapjes verhoogd tijdens verschillende syntheses waarbij decaanzuur wordt gebruikt. In de plaats van een stijgende d_{NC} en σ_d leidde de toevoeging van oliezuur aan een op decaanzuur gebaseerde synthese tot een verminderde d_{NC} en σ_d. Deze trends staan in constrast met de stijging van deze parameters wanneer de hoeveelheid oliezuur werd verhoogd bij een op oliezuur gebaseerde synthese. Dit wil zeggen dat het veranderen van de ligand ketenlengte in een hete injectie synthese andere parameters dan de monomeer oplosbaarheid, die een invloed hebben op de balans tussen de nucleatie- en groeisnelheid, beïnvloedt. Ten tweede werd het effect van de ligand ketenlengte op de oppervlaktespanning onderzocht door een synthese uit te voeren met oliezuur en decaanzuur in dezelfde hoeveelheid. Het NMR spectrum van deze deeltjes toont aan dat evenveel oleaat als decanoaat gebonden was aan het oppervlak. De afwezigheid van een duidelijke voorkeur gaf aan dat de ligand ketenlengte geen significante invloed heeft op de oppervlaktespanning van het nanokristal. Ten derde werd de diffusie coëfficiënt van verschillende liganden en cadmium oleaat opgemeten met NMR spectroscopie. We konden besluiten dat de diffusie coëfficiënten een trend volgen beschreven door een functie van een vrij roterend staafvormig object. Dit resultaat toonde aan dat er een directe link bestaat tussen de verandering van de ligand ketenlengte en de variatie van de difussie coëfficiënt van het monomeer.

We kwamen tot het algemeen besluit dat de grootte-regeling een gevolg is van een samenspel tussen de diffusie coëfficiënt en de oplosbaarheid van het monomeer. De relatie tussen de grootte-regeling door de ligand ketenlengte en de coördinatie van het monomeer door de liganden werd verder nagegaan door deze studie uit te breiden naar amines en fosfine oxides. Vooral in het geval van de amines had de ketenlengte geen merkbaar effect op d_{NC}, wat aangaf dat er weinig interactie is met het monomeer. Dit lag in lijn met de zwakke, dynamische stabilisatie van CdSe nanokristallen door amines. Deze studie toonde dus aan dat de verandering van de ligand ketenlengte een praktische

manier is om de diameter van het nanokristal te regelen bij volledige conversie van de hete injectie synthese. Bovendien kan de ketenlengte van het ligand dienen om de interactie tussen het additief en het monomeer te voorspellen, wat kan leiden tot een beter inzicht in de hete injectie synthese zelf.

Kwantumstippen worden bekomen als colloïdale suspensie waarbij de nanokristallen sterisch gestalibilseerd worden door moleculen die in het vakjargon liganden worden genoemd. Ze zijn veelal organische moleculen met een functionele groep en een lange alifatische staart en spelen een belangrijke rol tijdens de synthese.[6;7] Het is voordelig om na de synthese de anorganische/organische barrière van de kwantumstippen te bestuderen. Ten slotte bepalen deze liganden een groot deel van de fysicochemische eigenschappen van de kwantumstippen, zoals de fotoluminescentie kwantum opbrengst, de colloïdale stabiliteit en de procesbaarheid.[8–11] Bijgevolg is een diepgaande kennis van de oppervlaktechemie vereist om kwantumstippen van hoge kwaliteit te produceren.

- In het derde hoofdstuk beschreven we een NMR methode die ons inzicht geeft in de liganddistributie op het nanokristal oppervlak. Spectrale gatbrandingsexperimenten werden gebruikt om de oppervlaktechemie van PbSe en CdSe nanokristallen bedekt met oleaat liganden te onderzoeken. Deze oleaat liganden zijn zeer geschikt voor deze NMR studie aangezien ze beschikken over een geïsoleerde alkeen resonantie bij $\approx 5.6 - 5.7$ ppm. Een spectraal gatbrandingsexperiment werd uitgevoerd waarbij het midden van de alkeen resonantie het doelwit is. Het verschijnen van een spectraal gat geeft aan dat de resonantie heterogeen verbreed is. Wanneer de gatbrandingspositie werd gewijzigd, wijzigde de positie van het gat ook. Dit geeft aan dat de ligandenschil bestaat uit een continue reeks van oleaat groepen met verschillende chemische omgevingen. Vervolgens werden spectrale gatbrandingsherstel experimenten opgenomen om informatie te winnen in verband met de structuur van de ligandenschil. Om zo'n spectraal gatbrandingsherstel experiment te verkrijgen, werd de wachttijd verhoogd tussen het satureren en het opnemen van een 1D ^{1}H spectrum. Voor PbSe kwantumstippen werd zelfs bij de bestraling van slechts een smal deel van de resonantie een significant gat gebrand en de signaal intensiteit van de volledige resonantie was verzwakt. Bovendien herstelde de in-

tensiteit rond het initieel gat zich sneller dan de volledige intensiteit van de resonantie. Dit is het bewijs van snelle saturatietransfer naar andere delen van de resonantie. De hoge en lage veldkant van de resonantie vertoonden beiden dezelfde vorm als de originele resonantie maar met een verschillende evenredigheidsconstante. Deze observaties gaven een tegenstijdige uitkomst: de saturatie werd snel verspreid van het gat naar beide zijden van de resonantie en toch was er geen thermalisatie tussen beide zijden. Dit gedrag komt voor wanneer de resonantie uit (minstens) twee verzamelingen bestaat, die beiden een overlap vertonen met de bestraalde frequentie en heterogeen verbreed zijn. De saturatie transfer gebeurde in dit geval snel in elke verzameling, maar was afwezig tussen de verzamelingen. Deze twee (of meer) verzamelingen konden gelinkt worden aan twee (of meer) facetten met vergelijkbare liganddensiteit.

Net als PbSe kwantumstippen waren de resonanties van CdSe kwantumstippen heterogeen verbreed en bestond de resonantie uit een continue verzameling van resonanties. De spectrale gatbranding resulteerde hier in een duidelijker initieel gat. Bovendien leek het gat van vorm te veranderen en bleef, na het initieel snel herstel van de regio rond het gat, het gat nog steeds zichtbaar. Dit gaf aan dat CdSe/oleaat twee verzamelingen heeft met een duidelijk verschillend relaxatiegedrag. Het relaxatiegedrag van de verzameling aan de lage veldkant was zeer vergelijkbaar met dat van de PbSe/oleaat verzamelingen. De verzameling aan de hoge veldkant daarentegen gedroeg zich anders. Tijdens het spectraal gatbranden aan de hoge veldkant van de resonantie, bleef een gat zichtbaar na het initieel herstel. Daarenboven was het volledig herstel van de resonantie veel trager. Om deze reden leek de verzadigingsoverdracht minder efficiënt of zelfs onbestaande in de deelverzameling aan de hoge veldzijde van de resonantie. Dit verklaart mogelijks de vormwijziging van het spectrale gat in het midden van de resonantie. Anderzijds veranderde de vorm van het spectrale gat aan de hoge veldzijde van de resonantie niet gedurende het herstel. Dit wijst erop dat de deelverzameling aan de hoge veldzijde van de resonantie degene is waar thermalisatie ontbreekt. Het feit dat zo een deelverzameling aanwezig is, ligt in lijn met het verschil tussen de verkregen intensiteit op de bestralingsfrequentie en het globale intensiteitsverlies na het branden van het gat. In het geval van CdSe/oleaat,

waar het spectrale gat dieper ligt, is het immers zo dat de globale signaalintensiteit ook minder daalt dan bij PbSe/oleaat. Wanneer we kijken naar het spectrale gat aan de lage veldzijde en in het centrum, kunnen we stellen dat de tweede deelverzameling zich over de gehele resonantie spreidt en zich gelijkaardig gedraagt als de beide deelverzamelingen bij PbSe/oleaat. De andere resonantie, meer aan de hoge veldzijde, is nog steeds een heterogene deelverzameling, aangetoond door de verzadigingspositie te wijzigen.

De deelverzamelingen werden gelinkt aan twee kristalvlakken door middel van klassieke Moleculaire Dynamica berekeningen. De resultaten toonden aan dat de liganden de hoogste affiniteit hebben voor de (100) vlakken. De liganden op deze vlakken waren allen in dezelfde richting georiënteerd. De randen van de Cd-rijke (111) vlakken waren ligandrijk, met enkele mobiele liganden in het midden van deze vlakken. Op de Se-rijke (111) vlakken waren slechts enkele liganden gebonden. De geïsoleerde liganden op de Cd- of Se-rijke (111) vlakken zijn vermoedelijk meer gesolvateerd dan dicht gepakte liganden. Dit zou kunnen leiden tot een meer gelijkaardige chemische omgeving voor de geïsoleerde liganden waardoor deze deelverzameling een kleinere chemische shift vertoont dan de deelverzameling van dicht gepakte liganden. Door de grote onderlinge afstand, kunnen de geïsoleerde liganden op de (111) vlakken hun verzadiging niet overbrengen naar andere liganden waardoor het spectrale gat enkel verdwijnt door tragere spin-rooster relaxatie, aan hetzelfde tempo als de relaxatie van de volledige resonantie. Dit is precies wat we waarnemen in onze experimenten met CdSe kwantumstippen.

- In het finale hoofdstuk combinerden we een experimentele en theoretische studie op twee-component ligandenschillen van collïdale kwantumstippen. Startende van het modelsysteem van CdSe kwantumstippen bedekt met oleaat liganden [12], toonden we via NMR spectroscopie aan dat blootstelling aan andere carbonzuren resulteert in een één-voor-één uitwisseling tussen de liganden waarbij de verhouding ligand/overmaat Cd gelijk blijft. De één-voor-één uitwisseling werd vastgesteld tussen twee liganden die bij NMR spectrocopie apart konden gevolgd worden, oliezuur en 1-undecaanzuur. Daarna werd vastgesteld dat de samenstelling van de ligandenschil gelijk is aan de samenstelling

van het mengsel in oplossing bij drie verschillende systemen, met drie verschillende carbonzuren met een enkelvoudige koolstofketen. Bijvoorbeeld, als een equivalent myristinezuur werd toegevoegd aan een CdSe/oleaat dispersie, bestond de ligandenschil uit evenveel oliezuur als myristinezuur. Schrijven we de CdSe kwantumstip kern als [CdSe], een carbonzuur in het algemeen als HX en een cadmium carboxylaat als (CdX_2), dan kunnen we de uitwisselingsvergelijking schrijven als volgt:

$$[\mathrm{CdSe}](\mathrm{CdX_2}) + \mathrm{HX'} \rightleftharpoons [\mathrm{CdSe}](\mathrm{CdXX'}) + \mathrm{HX} \tag{2}$$

Een andere observatie werd waargenomen als een vertakt carbonzuur werd toegevoegd aan de CdSe/oleaat dispersie. Slechts 22% van het oliezuur kon worden vervangen wanneer 2-hexyldecaanzuur werd toegevoegd in grote overmaat. Dit wordt toegeschreven aan de één-voor-één uitwisseling in combinatie met het groter volume van het vertakt carbonzuur. Het oppervlak van het origineel systeem kan beschreven worden als een willekeurig mengsel van roosterplaatsen die worden bezet door een oleaat of die onbezet zijn. De laatste stellen de overgebleven vrije plaatsen in de ligandenschil voor. Terwijl de uitwisseling van oleaat naar een lineair carbonzuur het aantal onbezette plaatsen ongemoeid laat, zal dit niet zo zijn voor een uitwisseling naar vertakte carbonzuren. Indien er van uitgegaan wordt dat 2-hexyldecanoaat 2 roosterplaatsen bezet, kunnen we de oliezuur/2-hexyldecaanzuur uitwisseling schrijven als een reactie waarin gebonden oleaat en een onbezette plaats worden uitgewisseld voor één gebonden 2-hexyldecanoaat:

$$\mathrm{OAc}_b + \mathrm{HDAc}_f + \bigcirc \rightleftharpoons \mathrm{HDAc}_b + \mathrm{OAc}_f \tag{3}$$

Simulaties, uitgevoerd door de groep van Ivan Infante aan de VU Amsterdam, hielpen ons om de oorsprong van dit gedrag te bepalen. Eerst werd een simulatie uitgevoerd om te zien of alle vertakte carbonzuren genoeg ruimte hebben om aan het oppervlak te binden. De simulatie bewees dat volledige bezetting door het vertakte zuur mogelijk is. Vervolgens werden er simulaties uitgevoerd bij verschillende HDAc fracties $x_{\mathrm{HDAc,b}}$. Het toonde dat voornamelijk de (100) facetten zeer compact bezet worden als pure oleaat subdomeinen. Daarenboven waren er gemengde subdomeinen (OAc/HDAc) te vinden op

de Cd-(111) facetten, terwijl de randen en de Se-(111) facetten voornamelijk bezet werden door 2-hexyldecanoaten. Fasescheiding blijkt gunstig, zowel enthalpisch, door intermoleculaire interacties, als entropisch, door betere mobiliteit van de oleaten in de homogene fasen. Alle simulatieresultaten suggereren dat de experimenteel lage uitwisseling van vertakte liganden kan verantwoord worden door het bestaan van domeinscheidingen van organische moleculen op het nanokristal oppervlak. Deze studie bevestigd dat binaire ligandschillen van twee lineaire carbonzuren op een simpele manier kunnen bekomen worden door de liganden in de gewenste verhouding toe te voegen aan de dispersie. Voor een volumineus ligand daarentegen bewijst deze studie dat het bekomen van een gemengde ligandenschil niet zo eenvoudig is. Het benadrukt het belang van mengbaarheid van de gebonden en uitwisselende species wanneer een experiment ontworpen wordt.

Referenties

[1] Dmitri V. Talapin, Jong-Soo Lee, Maksym V. Kovalenko, and Elena V. Shevchenko. *Prospects of Colloidal Nanocrystals for Electronic and Optoelectronic Applications.* Chemical Reviews, 110(1):389–458, 2010. PMID: 19958036.

[2] Talha Erdem and Hilmi Volkan Demir. *Color Science of nanocrystal quantum dots for lighting and displays.* Nanophotonics, 2(1):57–81, 2013.

[3] P. Martyniuk and Antoni Rogalski. *Quantum-dot infrared photodetectors: Status and outlook.* Progress in Quantum Electronics, 32(3-4):89–120, 2008.

[4] Sofie Abe, Richard K. Capek, Bram De Geyter, and Zeger Hens. *Reaction Chemistry/Nanocrystal Property Relations in the Hot Injection Synthesis, the Role of the Solute Solubility.* ACS Nano, 7(2):943–949, Feb 2013.

[5] Dmitri V. Talapin, Andrey L. Rogach, Markus Haase, and Horst Weller. *Evolution of an ensemble of nanoparticles in a colloidal solution: Theoretical study.* Journal of Physical Cemistry B, 105(49):12278–12285, Dec 13 2001.

[6] Yadong Yin and Paul Alivisatos. *Colloidal nanocrystal synthesis and the organic-inorganic interface.* Nature, 437(7059):664–670, Sep 29 2005.

[7] Liberato Manna, Erik C. Scher, and A. Paul Alivisatos. *Synthesis of Soluble and Processable Rod-, Arrow-, Teardrop-, and Tetrapod-Shaped CdSe Nanocrystals.* Journal of the American Chemical Society, 122(51):12700–12706, 2000.

[8] Jonathan Owen. *The coordination chemistry of nanocrystal surfaces.* Science, 347(6222):615–616, Feb 6 2015.

[9] Jong-Soo Lee, Maksyn V. Kovalenko, Jing Huang, Dae Sung Chung, and Dmitri V. Talapin. *Band-like transport, high electron mobility and high photoconductivity in all-inorganic nanocrystal arrays.* Nature Nanotechnology, 6(6):348–352, 2011.

[10] Jacek Jasieniak and Paul Mulvaney. *From Cd-rich to Se-rich - The manipulation of CdSe nanocrystal surface stoichiometry.* Journal of the American Chemical Society, 129(10):2841–2848, Mar 14 2007.

[11] Nicholas C. Anderson, Mark P. Hendricks, Joshua J. Choi, and Jonathan S. Owen. *Ligand Exchange and the Stoichiometry of Metal Chalcogenide Nanocrystals: Spectroscopic Observation of Facile Metal-Carboxylate Displacement and Binding.* Journal of the American Chemical Society, 135(49):18536–18548, Dec 11 2013.

[12] Bernd Fritzinger, Richard K. Capek, Karel Lambert, José C. Martins, and Zeger Hens. *Utilizing Self-Exchange To Address the Binding of Carboxylic Acid Ligands to CdSe Quantum Dots.* Journal of the American Chemical Society, 132(29):10195–10201, 2010. PMID: 20608680.

English summary

Colloidal nanocrystals are a class of materials with enormous potential for solving a lot of issues we face today[1]. They are extremely small crystalline particles with a size between that of bulk solids and molecular clusters. Their applications range from Light emitting diodes[2] to solar cells[1] and even photodetectors[1]. Semi-conductor nanocrystals are called quantum dots (QDs). These quantum dots display unique electrical and optical properties since they form a bridge between an atom and bulk material in terms of the electronic energy level density. For example, the absorption and emission shift to shorter wavelengths as the size of the QD decreases. This makes them extremely useful for all kinds of applications.[2;3]

Following the widespread use of colloidal nanocrystals as a model system to explore and understand the properties of nanoscale materials and their implementation as active material in various applications, a good control over their production is necessary. To gain control over their production, knowledge about the reaction is crucial. Therefore, mechanistic studies have become a hot topic in our field.

- In the first chapter, the reaction of aminophosphines (tris(dimethylamino)phosphine or tris(diethylamino)phosphine) and indium halides ($InCl_3$, $InBr_3$ or InI_3) to form InP nanoparticles was studied. This reaction is not straightforward due to the oxidation states of the indium and phosphorous. The reaction of In^{III} and P^{III} has to be preceded by a reduction of P^{III} to P^{-III}. To investigate possible intermediate reaction steps involved in the formation of InP out of aminophosphine and $InCl_3$, the exhaust gasses of an InP QD synthesis were scrubbed using a methanolic solution of hydrogen chloride to enable us to trap the exhaust gasses as a salt. After recrystallization in ethyl acetate, this salt was identified by single crystal X-ray diffraction as dimethylammonium chloride for a reaction where $P(NMe_2)_3$ was used as the

phosphorus precursor. This points towards an exchange between the amines used as a solvent in the synthesis and the amino groups coordinating to phosphorus in the original precursor. Subsequently, this was confirmed by NMR spectroscopy by mixing $P(NEt_2)_3$ and dodecylamine in a vial under an inert atmosphere. The initial solution featured a single resonance of $P(NEt_2)_3$ at 118 ppm. This had almost completely vanished after 1 h of reaction due to transamination and new resonances appeared at 111 and 98 ppm, next to several less intense resonances especially at around 11 ppm. These species were subjected to an elaborate NMR study to determine their identity. In addition, the InP synthesis was performed in several solvents which shows that InP was only formed when a primary amine is used.

The InP synthesis reached full yield with respect to indium when the ratio between the aminophosphine and the indium halide is 4:1. At this point, we hypothesized that a phosphorus precursor excess is needed to obtain full chemical yield because the aminophosphine plays more than one role in the synthesis. Hence, a reaction equation was formulated:

$$InX_3 + 4\,P(NHR)_3 \rightleftharpoons InP + 3\,P(NHR)_4X \tag{4}$$

In this reaction, one aminophosphine is used to form the InP unit and is reduced from P^{III} to P^{-III}. The three remaining aminophosphines serve as reducing agents and are thus transformed into phosphonium salts (P^{V}). A first confirmation of this reaction equation was provided by NMR measurements of aliquots taken during the synthesis. These spectra reveal the formation of a byproduct, different from the transamination products. This byproduct was formed at the same rate as the InP formation. Secondly, The byproduct was isolated and identified by means of mass spectrometry and NMR as being a fully transaminated phosphonium salt. Finally, a reaction mechanism was proposed. In accordance with the double role of phosphorus, this mechanism assumes a nucleophilic attack by the phosphorus center of one aminophosphine on an amino group of another aminophosphine. Considering that the fully transaminated $P(NHR)_3$ is the actual reactant, an adduct of $InCl_3$ and $P(NHR)_3$ is formed in a first step. Subsequently, a nucleophilic attack on the nitrogen by a second $P(NHR)_3$ results in the formation of an InP intermediate and a first equivalent of

the $P(NHR)_4Cl$ phosphonium salt. Two more equivalents of $P(NHR)_3$ further reduce the phosphorus in the InP intermediates and result in the formation of 1 equivalent of InP.

- In the second chapter, We investigated the relation between the chain length of ligands used and the size of the CdSe nanocrystals formed in the hot injection synthesis. With two different CdSe nanocrystal syntheses, we consistently found that longer chain carboxylic acids resulted in smaller nanocrystals with improved size dispersions. However, opposite from the idea that this results from a reduction of the reaction rate, we showed that varying the carboxylic acid chain length leaves the reaction rate unchanged. The rate of nucleation and growth of nanocrystals is set by the rate of solute formation. Under these conditions, nanocrystals with different sizes can be obtained by shifting the point where the solute consumption by nanocrystal growth overtakes the solute consumption by nucleation.[4] Hence the question as to how the ligand chain length affects this takeover. To analyze this question, we started from the expressions for the rate of nanocrystal nucleation J_N (*i.e.*, the number of nuclei formed per second) and nanocrystal growth J_G (*i.e.*, the change of the NC radius per second). Both depend on parameters such as the diffusion coefficient D of the solute, the volume of a solute molecule v_0, the surface tension γ, the molar volume V_m of the material formed, the nanocrystal radius r, the rate constants k_g^∞ and k_d^∞ for solute adsorption and desorption, the transfer coefficient α for solute adsorption and the supersaturation S, which is defined as the ratio between the actual concentration and the solubility $[M]_0$ of the solute[5]

  With an in-depth experimental investigation, the relation between the acid chain length and the nanocrystal size was determined. First, the amount of oleic acid was gradually increased in different syntheses run with decanoic acid. Rather than increasing d_{NC} and σ_d, the addition of oleic acid to a decanoic acid-based synthesis systematically reduced both d_{NC} and σ_d. These trends strongly contrast with the increase of both parameters when the amount of oleic acid in an oleic acid-based synthesis was raised. Hence, changing the ligand chain length in a hot injection synthesis affects other parameters, next to the solute solubility, that have an influence on the balance between the nucleation and

growth rate. Second, the effect of ligand chain length on the surface tension was investigated by performing a synthesis with both oleic and decanoic acid in equal amounts. The NMR spectrum of these particles showed that equal amounts of oleate and decanoate are bound to the surface. The absence of preferential adsorption indicates that the ligand chain length had no significant effect on the nanocrystal surface tension. Third, the diffusion coefficient of several ligands and cadmium oleate was measured with NMR spectroscopy. We can conclude that the obtained diffusion coefficients follow a trend described by a function for freely rotating rod-like objects. This result indicates that we can directly link a change in the carboxylic acid chain length to a variation of the diffusion coefficient of the solute.

we come to the overall conclusion that this size tuning is due to a change in the diffusion coefficient and the solubility of the solute. The relation between size tuning by the ligand chain length and the coordination of the solute by the ligands was further explored by expanding the study to amines and phosphine oxides. Especially in the case of amines, the ligand chain length had no noticeable effect on d_{NC}, suggesting little interaction with the solute in line with the weak, dynamic stabilization of CdSe nanocrystals by amines. Hence, this study showed that changing the ligand chain length provides a practical way to tune the nanocrystal diameter at full yield in a hot injection synthesis and enhance the size dispersion, which is key to the application of nanocrystals as light emitters, for example in display applications. Moreover, the ligand chain length can be used to probe the interaction between a reaction additive and the solute, which can lead to better insight in the hot injection synthesis itself.

Quantum dots are obtained as a colloidal suspension which is sterically stabilized by molecules that are called ligands in the jargon. They are often organic molecules, with a functional head group and a long aliphatic chain, that play a very important role in deciding the shape and size of the nanocrystals during the synthesis.[6;7] Afterwards, It is beneficial to have information about the inorganic/organic interface. After all, these ligands determine a great deal of the physicochemical properties of the quantum dots like the photoluminescence quantum yield, the colloidal stability and the processability.[8–11] Consequently, an in-depth knowledge of the surface

chemistry is mandatory for fabricating high quality of QDs.

- In the third chapter, we described an NMR method for gaining insight in the ligand distribution on the nanocrystal surface. Spectral hole burning experiments were used to examine the surface chemistry of CdSe and PbSe quantum dots capped with oleate ligands. These oleates are very suitable for this NMR study thanks to their isolated alkene resonance at $\approx 5.6 - 5.7$ ppm. A spectral hole burning experiment was conducted whereby the middle of the alkene resonance was targeted. The appearance of a spectral hole indicates heterogeneous broadening. When the hole burning position was varied, the position of the spectral hole varied as well. This indicates that the ligand shell is composed of a continuous range of oleate moieties with different chemical environments. Subsequently, spectral hole burning recovery experiments were recorded to gain information about the ligand shell structure since it reflects the loss of irradiation induced transparency. To acquire a hole burning recovery series, the 1D ^{1}H spectrum recorded after every hole burning was delayed by increasing delay times. For PbSe quantum dots, it was found that a significant hole is burnt and the signal intensity of the complete resonance attenuated although only a small part was saturated. In addition, the initial hole recovers faster than the complete intensity of the resonance. This was evidence of rapid saturation transfer to other parts of the resonance. The upfield and downfield side of the resonance were both proportional to the completely recovered spectrum, yet with different proportionality constants. These observations thus left us with the apparently contradictory outcome that saturation is rapidly transferred from the spectral hole to either the downfield or the upfield side of the resonance, whereas both sides do not thermalize. Such behavior will occur, however, when the manifold of alkene resonances consists of (at least) two separate parts that are both heterogeneously broadened and overlap with the irradiated frequency. In the case that saturation transfer is rapid within these submanifolds yet absent between them, the observed relaxation behavior occurs. These two (or more) submanifolds can be linked to two (or more) types of facets on the nanocrystal surface with comparable ligand densities.

  Just like the PbSe QDs, the resonance of the CdSe QDs was hetero-

geneously broadened and consisted out of a manifold of alkene resonances since a spectral hole was formed at the position of irradiation during each experiment. Here, the spectral hole burning resulted in a more distinct initial spectral hole. During the recovery the spectral hole seemed to change shape. Moreover, after the initial rapid recovery, the spectral hole had not completely disappeared. This indicates that, opposite from PbSe/Oleate, CdSe/Oleate featured two frequency submanifolds with a markedly different saturation relaxation behavior. The behavior of the downfield submanifold was similar to the PbSe/oleate submanifolds. The upfield submanifold, however, displayed a different behavior. During the spectral hole burning at the upfield side, the spectral hole persisted after the initial fast recovery and the overall recovery was characterized by a lower rate constant. Therefore, it seemed like the saturation transfer in the submanifold at the upfield side of the resonance was less efficient or even non-existing. This can explain the change in shape of the spectral hole in the center of the resonance. Importantly, during the recovery of the spectral hole at the upfield side of the resonance, the shape of the spectral hole did not change. This indicates that the submanifold lacking thermalization is located at the upfield side of the resonance. The presence of such a subset is in line with the difference between the intensity attained at the irradiation frequency and the overall intensity loss after spectral hole burning. Indeed, whereas in the case of CdSe/oleate, the spectral hole was slightly deeper, the overall signal intensity droped less than for PbSe/oleate. It can be said that - looking at the spectral hole burning at the downfield side and in the center - the second submanifold spread over the entire resonance and behaved in much the same way as either of the submanifolds found in PbSe/oleate. The other resonance, more localized at upfield shifts, was still a heterogeneous subset as can be observed when the saturation position is varied.

The submanifolds were linked to two facets with different properties by Classical Molecular Dynamics simulations. The result showed that the oleate ligands have the highest affinity towards the (100) facets. These ligands were all oriented in the same direction on the (100) facets. The edges of the Cd-rich (111) facets were rich in ligands, with a few ligands mobile ligands in the center of these facets. Only few ligands were bound to the the Se-rich (111) facets. The ligands

isolated on the Cd-rich (111) and the Se-rich (111) facets were probably more solvated than densely packed ligands. This could lead to a more similar chemical environment for all isolated ligands and thus the submanifold would cover a smaller chemical shift range than packed ligands. It is straightforward that the ligands isolated on the Cd-rich (111) and the Se-rich (111) facets cannot transfer saturation to other ligands since the distance between the resonances is too large. The hole will disappear more slowly by spin-lattice relaxation, at the pace of the relaxation of the complete resonance. This is exactly what we saw in the experiments performed on CdSe QDs.

- In the final chapter, we proposed a combined experimental and theoretical study on two-component ligand shells of colloidal quantum dots made by ligand exchange. Taking oleate-capped CdSe quantum dots as a model system,[12] we first showed by NMR spectroscopy that exposure to other fatty acids results in a one-for-one exchange that leaves the net ligand/excess cadmium balance unchanged. First, a one-for-one exchange was observed between two ligands that can be monitored separately by NMR spectroscopy, oleic acid and 1-undecenoic acid. Subsequelty, it was found that the ligand shell composition equals that of the dispersion for single chain carboxylic acid systems, oleic acid / myristic acid, oleic acid / 1-undecenoic acid and oleic acid / nonanoic acid. For example, when one equivalent of myristic acid was added to a CdSe/oleate dispersion, the ligand shell contained equal amounts of oleates and myristates. Writing the core CdSe QD as [CdSe], a carboxylic acid in general as HX and a surface cadmium carboxylate as (CdX_2), the presumed exchange reaction can then be written as:

$$[\mathrm{CdSe}](\mathrm{CdX_2}) + \mathrm{HX'} \rightleftharpoons [\mathrm{CdSe}](\mathrm{CdXX'}) + \mathrm{HX} \tag{5}$$

A different observation was made when a branched carboxylic acid was added to the CdSe/oleate dispersion. For 2-hexyldecanoic acid, only a small part of the oleates was replaced, even when adding a huge excess of the branched carboxylic acid. This was attributed to the tit-for-tat exchange in combination with the larger volume of the branched carboxylic acid. The surface of the original, oleate-capped QDs can be described as a random mixture of lattice sites occupied

by oleate ligands and unoccupied sites, the latter reflecting the remaining available space in the ligand shell. Whereas the exchange of oleate for a primary carboxylate will leave the number of unoccupied sites unchanged, this will be different if oleate is replaced by a branched carboxylate like 2-hexyldecanoate. Assuming that bound 2-hexyldecanoate occupies 2 lattice sites, we can than rewrite the oleic acid/2-hexyldecanoic acid exchange as a reaction in which bound oleate and a free site are exchanged for bound 2-hexyldecanoate:

$$\mathrm{OAc}_b + \mathrm{HDAc}_f + \bigcirc \rightleftharpoons \mathrm{HDAc}_b + \mathrm{OAc}_f \tag{6}$$

Simulations performed by the group of Ivan Infante at the VU Amsterdam helped us to understand the origin of this behavior. First, a simulation was performed to check if all branched carboxylic acids have enough space to bind to the nanocrystal surface. Indeed, the simulation showed that complete coverage of the nanocrystal by 2-hexyldecanoates was sterically allowed. Subsequently, simulations were performed at a different HDAc fractions $x_{\mathrm{HDAc,b}}$. It showed that oleates mostly occupied (100) facets, creating very compact, almost pure sub-domains. In addition, sub-domains of mixed composition (OAc/HDAc) were usually found at the Cd-(111) facets, whereas edges and the Se-(111) facets were covered with mainly 2-hexyldecanoates. Phase separation appeared as being favored both enthalpically, due to better intermolecular interactions, and entropically, because of the greater mobility of oleates in the homogeneous phase. All results provided by simulations strongly suggest that the experimental low exchange of branched ligands (HDAc) can be explained by the existence of a domain separation of the organic ligands at the nanocrystal surface. This study confirms that binary ligand shells can be accomplished by simply adding a ligand mixture with desired composition to the nanocrystal dispersion when working with single chain carboxylic acids. However, for more voluminous ligands, this study proves that obtaining a mixed ligand shell is not that straightforward. Hence, it stresses the importance of the miscibility of the bound and the exchanging species in designing an efficient ligand exchange reaction.

References

[1] Dmitri V. Talapin, Jong-Soo Lee, Maksym V. Kovalenko, and Elena V. Shevchenko. *Prospects of Colloidal Nanocrystals for Electronic and Optoelectronic Applications.* Chemical Reviews, 110(1):389–458, 2010. PMID: 19958036.

[2] Talha Erdem and Hilmi Volkan Demir. *Color Science of nanocrystal quantum dots for lighting and displays.* Nanophotonics, 2(1):57–81, 2013.

[3] P. Martyniuk and Antoni Rogalski. *Quantum-dot infrared photodetectors: Status and outlook.* Progress in Quantum Electronics, 32(3-4):89–120, 2008.

[4] Sofie Abe, Richard K. Capek, Bram De Geyter, and Zeger Hens. *Reaction Chemistry/Nanocrystal Property Relations in the Hot Injection Synthesis, the Role of the Solute Solubility.* ACS Nano, 7(2):943–949, Feb 2013.

[5] Dmitri V. Talapin, Andrey L. Rogach, Markus Haase, and Horst Weller. *Evolution of an ensemble of nanoparticles in a colloidal solution: Theoretical study.* Journal of Physical Cemistry B, 105(49):12278–12285, Dec 13 2001.

[6] Yadong Yin and Paul Alivisatos. *Colloidal nanocrystal synthesis and the organic-inorganic interface.* Nature, 437(7059):664–670, Sep 29 2005.

[7] Liberato Manna, Erik C. Scher, and A. Paul Alivisatos. *Synthesis of Soluble and Processable Rod-, Arrow-, Teardrop-, and Tetrapod-Shaped CdSe Nanocrystals.* Journal of the American Chemical Society, 122(51):12700–12706, 2000.

[8] Jonathan Owen. *The coordination chemistry of nanocrystal surfaces.* Science, 347(6222):615–616, Feb 6 2015.

[9] Jong-Soo Lee, Maksyn V. Kovalenko, Jing Huang, Dae Sung Chung, and Dmitri V. Talapin. *Band-like transport, high electron mobility and high photoconductivity in all-inorganic nanocrystal arrays.* Nature Nanotechnology, 6(6):348–352, 2011.

[10] Jacek Jasieniak and Paul Mulvaney. *From Cd-rich to Se-rich - The manipulation of CdSe nanocrystal surface stoichiometry.* Journal of the American Chemical Society, 129(10):2841–2848, Mar 14 2007.

[11] Nicholas C. Anderson, Mark P. Hendricks, Joshua J. Choi, and Jonathan S. Owen. *Ligand Exchange and the Stoichiometry of Metal Chalcogenide Nanocrystals: Spectroscopic Observation of Facile Metal-Carboxylate Displacement and Binding.* Journal of the American Chemical Society, 135(49):18536–18548, Dec 11 2013.

[12] Bernd Fritzinger, Richard K. Capek, Karel Lambert, José C. Martins, and Zeger Hens. *Utilizing Self-Exchange To Address the Binding of Carboxylic Acid Ligands to CdSe Quantum Dots.* Journal of the American Chemical Society, 132(29):10195–10201, 2010. PMID: 20608680.

1 Introduction

In the introduction basic principles about quantum dots and the hot injection synthesis will be explained. Subsequently, knowledge about surface chemistry of quantum dots will be illustrated, together with the possible surface chemistry analysis techniques. Finally, an outline of the thesis will be presented.

1.1 Introduction

Technology never stops. Every day advances in certain fields are accomplished yet we still face numerous challenges before those advances are made. Think about photodetectors for example. There are excellent photodetectors available operating in the visible range of the electromagnetic spectrum, but detectors for the infrared are limited by high noise levels or difficult processing techniques. [1] Telecommunication, for example, lags behind because of this.

Light emitting diodes (LEDs) are another example. LEDs are used in lighting and displays. They face challenges like poor color purity or limited lifetimes. Issues such as readsorption of the produced light, internal reflections and unradiative recombination of the injected electron-hole pair all diminish the chances of certain materials to be used in LEDs. [2]

The depletion of energy resources leads to a high demand for new, oil-free energy solutions[1]. Therefore, solar cells are a highly researched topic. Commercial silicon based solar cells are available but since silicon has an indirect band gap, a lot of material is required to obtain sufficient efficiency. A lot of alternatives for commercial solar cells are extremely expensive or involve dangerous fabrication processes.

Imagine a class of materials that could solve all these issues. A class of materials with a tunable band gap from the visible region all the way up to the infrared. And on top of that, a class of materials which is relatively cheap to fabricate and can be processed in an easy, solution-based way. Such a class of materials actually exists: Nanocrystals (NCs). They are extremely small crystalline particles with a size between that of bulk solids and molecular clusters. The nanocrystal class can be subdivided by the type of material (*e.g.* metal, semiconductor or oxide nanocrystals) or by their properties (electronic, optical or magnetic). The focus of this work lays on semiconductor nanocrystals, called quantum dots (QDs).

The diameter of any nanocrystal can vary anywhere between one and a few hundreds of nanometers. Due to their extremely small size, they exhibit extraordinary properties as compared to the bulk material. First of all, nanocrystals display unique electronic properties since they form a bridge between an atom and bulk material in terms of the electronic energy level density. The electronic energy levels of an atom are known to be discrete whereas a bulk semiconductor, for example, has a valence band and a conduction band, separated by a bandgap (Figure 1.1).[3] These bands are continuous since the level spacing is smaller than the thermal energy at operating temperatures. The semiconductor nanocrystals or quantum dots (QDs), can be compared with the quantum mechanical particle in a box model.[4] Here, a particle is confined between x=0 and x=a by high potential energy barriers. By solving the Schrödinger equation with these boundary conditions, the eigenenergies in Equation 1.1 are found. Consequently, the eigenenergy will increase when the size of the box becomes smaller and more energy will be needed to confine a particle in this smaller region. For the quantum dot, the exciton is confined by the dimensions of the particle, leading to a transition from continuous to discrete energy levels. In addition, the band gap increases as the quantum dot size gets smaller (Figure 1.1).

$$E_n = \frac{\hbar^2 n^2 \pi^2}{2mr^2} \tag{1.1}$$

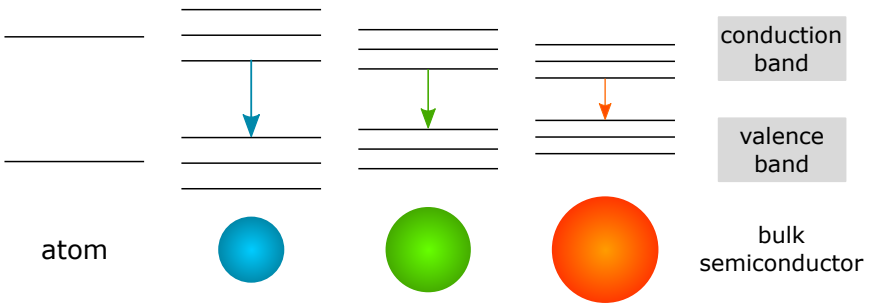

Figure 1.1: Schematic illustration of the density of states in an atom, QDs and a bulk semiconductor.

In this equation,

E_n	is the nth energy level,
$\hbar$	is Plank's constant devided by 2*π,
m	is the mass of the electron,
and r	is the nanocrystal radius,

The confinement can be associated with the Bohr exciton radius as well, which is the distance between an electron-hole pair in bulk semiconductors (Equation 1.2)[5].

$$r_B = \frac{\epsilon h^2}{\mu_{eff} \pi e^2} \tag{1.2}$$

Here, μ_{eff} is the reduced effective mass of the electron-hole pair and ϵ is the dielectric coefficient of the semiconductor. When the quantum dot radius is of the same order as the Bohr exciton radius, the exciton is confined by the dimensions of the particle, leading to the above described transition from continuous to discrete energy levels. With decreasing size, more energy is needed to create the exciton and the band gap will thus increases as well.

The quantum confinement effects will affect the optical features of the quantum dots. More energy is needed to create an electron-hole pair when the particle is smaller and more energy is released upon their recombination.[6] In other words, the crystals will emit a different color upon UV excitation (Figure 1.2). Indeed, the adsorption and emission features shift to shorter wavelengths as the size of the QD decreases.

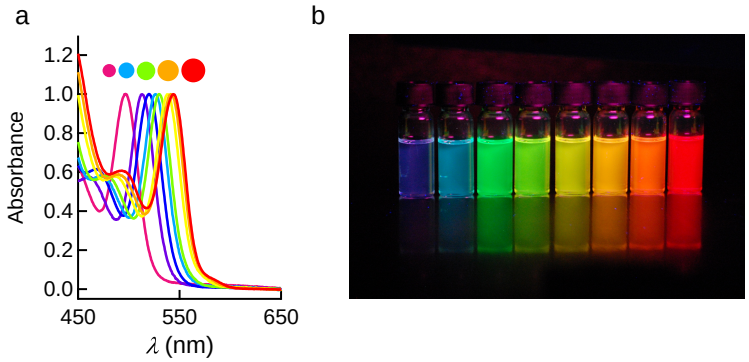

Figure 1.2: a) Absorption spectra of QDs with increasing size, as indicated by the dots in the same colors as the spectra. b) CdSe based QDs of different sizes ranked from small (left) to large (right), emitting a different color.

The unique electronic and optical properties of quantum dots allow them to be good candidates for a wide range of applications. As mentioned earlier, they can be the key for solving numerous challenges faced in science. For example, depending on the band gap tunability, QDs can be used in infrared detectors. Materials as InAs, PbSe and HgTe QDs are explored intensely in that field.[7] CdSe and InP are perfectly suited for LED fabrication when imbedded in a core/shell structure. In fact, by tuning their size, one can obtain very narrow emission of the preferred color in the complete visible range of the spectrum. They exhibit excellent photo luminescence properties and are color pure.[2] Nowadays, multinationals like Samsung and Sony use quantum dot technology for their displays.

1.2 The hot injection synthesis: nucleation and growth of colloidal nanocrystals

Before being able to use the quantum dots in different kinds of applications, they have to be synthesized. Over 20 years ago, the hot injection synthesis (HIS) was mentioned for the first time in literature by Murray, Norris and Bawendi.[8] It produces a colloidal quantum dot dispersion, stabilized by organic molecules called ligands. The HIS is based on rapidly injecting so-called precursors (P), inorganic salts or organometallic compounds, into a hot solvent with a sequential drop in temperature. The injection of pre-

cursors leads to instantaneous formation of monomers (M), which in turn are consumed by nucleation and growth to form the actual quantum dots (QDs):

$$\mathrm{P} \longrightarrow \mathrm{M} \rightleftharpoons \mathrm{QD} \tag{1.3}$$

The synthesis produces high quality, monodisperse colloidal nanocrystals with a well-defined size. Ever since, it has become a well established method for the formation of monodisperse, sterically stabilized colloidal nanocrystals. Moreover, numerous adaptations were reported by several research groups to improve the quality, reach even smaller size dispersions and expand the range of materials produced with the HIS.[9–12] The size and shape of the nanocrystals were adjusted by using various stabilizing ligands.[13;14] In addition, various core/shell structures were produced with a consequential increase of photoluminescence quantum yield.[15–17] By changing the initial precursors, it was found that the reaction kinetics or the outcome of the synthesis changed. A very nice example of such an adaptation was the tunable library of substituted thiourea precursors for metal sulfide nanocrystals, published in 2015 by Jonathan Owen and coworkers.[18]

The current understanding of the HIS mechanism relies on theories defined as early as the 1950's. These introduce terms as nucleation rate J_N, growth rate J_G and the critical radius r_c. The concept of *monomers* (M) is indispensable for these theories. These minimal building blocks of the nanocrystals can either form the crystals or dissolve back into solution. They simplify the theoretical approaches without having to identify their composition or structure. In this section, it will become apparent that J_N, J_G and r_c all depend on the supersaturation, a time-dependent variable. It is defined as the ratio between the actual monomer concentration ($[M]$) and the monomer equilibrium concentration, often referred to as the monomer solubility ($[M]_0$).

In the classical nucleation theory, a nucleus is considered to be a sphere and its free energy can be described by thermodynamics.[19] Since the surface/volume ratio is much larger for the nanoparticle, its Gibbs free energy will differ from the bulk Gibbs free energy. Therefore it is described by a surface term that depends on the surface tension (γ) and the surface area ($A(n)$), and a volume term as function of the chemical potential ($\mu^\circ(s)$) of a monomer in the bulk solid (Equation 1.4). Subsequently the surface area $A(n)$ can be written as function of the radius of the particle r and the volume term as a function of the monomer volume V_m (Equation 1.6). Figure 1.3a shows that both contributions have opposite signs and their sum will only decrease after a certain radius is reached. This implies that all nuclei smaller than this radius will be unstable, whereas the nuclei with a larger

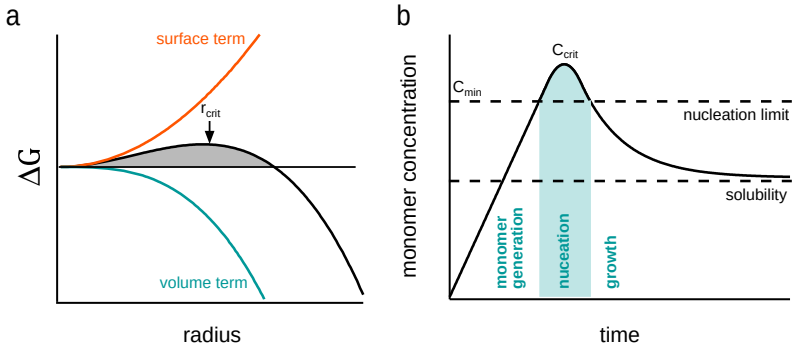

Figure 1.3: a) Schematic representation of gibbs free energy of a nanocrystal in function of its radius. b) Schematic representation of monomer concentration before and after nucleation as a function of time.

radius will survive. This particular radius is called the critical radius and acts as an activation barrier for nucleation (Equation 1.7).

$$G(r) = n\mu^{\circ}(s) + A(n)\gamma \tag{1.4}$$

$$= \frac{4}{3}\frac{\pi r^3}{V_m}\mu^{\circ}(s) + 4\pi r^2\gamma \tag{1.5}$$

$$= \frac{4}{3}\frac{\pi\ k_B T\ lnS\ r^3}{V_m} + 4\pi r^2\gamma \tag{1.6}$$

$$r_c = \frac{3\gamma}{k_B T\ lnS} \tag{1.7}$$

In these equations,

k_B	is the Boltzmann constant,
T	is the temperature,
S	is the supersaturation
V_m	is the molar volume,
r	is the nanocrystal radius,
and γ	is the surface tension.

The expression for the nucleation rate J_N in the classical nucleation theory is defined as:

$$J_N = \frac{2D}{v_0^{5/3}} exp\left(-\frac{16\pi\gamma^3 V_m^2 N_A}{3(RT)^3(\ln S)^2}\right) \tag{1.8}$$

Here,

D	is the monomer diffusion coefficient,
and v_0	is the monomer volume.

The supersaturation plays an important role here. A small change in S will cause a large variation in J_N.[20] The monomer diffusion constant D on the other hand, is used in the nucleation rate prefactor as a means to estimate its size.[21] Variation of only D in the prefactor has a fairly limited effect on J_N.

In 1950, LaMer and Dinegar studied the decomposition of sodium thiosulfate into sulfur sols, thereby describing the processes of nucleation and growth.[22] The LaMer mechanism is based on the assumption that nucleation and growth occur in different time frames. It is divided into three stages, shown in Figure 1.3b. During the first stage, the monomer concentration builds up. When it reaches a certain level, particles are nucleated in the second stage. Consequently, the monomer concentration will drop below the critical concentration again, which ensures a brief nucleation stage. Subsequently, the nanocrystals grow in the third and last stage. The very short nucleation discussed by LaMer and Dinegar is reffered to as *burst nucleation.*[19] In the hot injection synthesis, burst nucleation is of vital importance for the size distribution. If the nucleation would continue throughout the complete synthesis, nanocrystals with a wide range of sizes would be produced. Keeping the nucleation short guarantees a similar growth course for all nanocrystals which leads to a monodisperse ensemble. In the hot injection synthesis, it is attempted to obtain a burst nucleation by injecting the precursor(s) only at elevated temperature. Monomers will form swiftly and due to the drop in temperature and the decrease of the monomer concentration, the nucleation is assumed to stop.

After the nucleation, nanocrystals will grow by adding monomers to the nanocrystal surface. The growth rate, $J_G = dr/dt$, depends on two different processes. First, the monomers have to diffuse towards (and away from) the nanocrystal surface. Only then they can be absorbed to the surface. This adsorption is of course countered by desorption as well. Under steady-state conditions, the number of monomer units diffusing to the particle and the number of monomers desorbed from the surface should be equal to those added to the surface since monomers cannot accumulate at the nanocrystal surface. In 2001, Talapin *et al.* proposed a general relationship between the growth rate J_G and the nanocrystal radius r[23]:

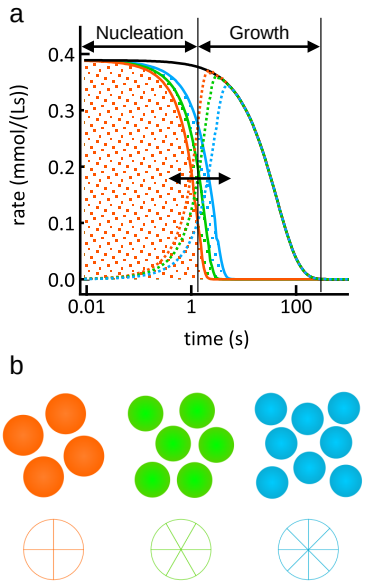

Figure 1.4: a) Schematic representation of the monomer generation rate (black), the nucleation rate (full colored lines) and the growth rate (dashed colored lines) in function of time. b) Nanocrystals generated with each pair of nucleation and growth rates.

$$J_G = \frac{dr}{dt} = DV_m \left[\mathrm{M}\right]_0 \left\{ \frac{S - exp\left(\frac{2\gamma V_m}{rRT}\right)}{r + \frac{D}{k_g^\infty} exp\left(\alpha \frac{2\gamma V_m}{rRT}\right)} \right\} \tag{1.9}$$

In this equation,

D	is the diffusion coefficient,
V_m	is the molar volume,
S	is the supersaturation,
γ	is the surface tension,
$[\mathrm{M}]_0$	is the monomer concentration,
k_g^∞	is the monomer adsorption rate constant for a flat surface
and α	is the transfer coefficient for the adsorption reaction.

A schematic representation of the monomer generation rate (black), the nucleation rate (orange) and the growth rate (blue) in function of time is depicted in Figure 1.4. These three parameters will determine the size

and the number of nanocrystals. First, all monomers are consumed by nucleation. Subsequently the nucleation rate decreases and the monomers start to be consumed by growth of existing nanocrystals as well. At a certain point, growth becomes the dominant monomer consumption. This point will be called the *takeover point* and is indicated by a black vertical line in figure 1.4.

The monomer generation rate will set both the nucleation and growth rate. If the monomer generation rate is faster, nucleation will benefit. This leads to the formation of more nanocrystals. At a constant monomer generation rate, the size and number of nanocrystals can still be altered. In that case, the monomer consumption by growth can only increase at the expense of the consumption by nucleation and vice versa.[24] The takeover point can thus be shifted to the left and less, larger nanocrystals will be formed. On the other hand, more, smaller nanocrystals will be formed when the takover point is shifted to the right. This can be compared to a pie. The monomer generation rate can be compared to the size of the pie. Even if two pies are equal in size, it can still be divided in different ways. More nucleation equals more pieces of pie, but those pieces will be smaller.

Depending on the ratio between the monomer diffusion coefficient D and the rate constant for monomer adsorption k_g^∞, growth can be limited by the diffusion of the monomer solute or by the surface reaction. Under diffusion control, $D << k_g^\infty r$, the growth rate boils down to:

$$J_G = \frac{DV_m \left[\mathrm{M}\right]_0}{r} \tag{1.10}$$

Figure 1.5 shows the growth rate as function of nanocrystal radius for a system in diffusion limitation. For small radii the growth rate has a positive slope, a negative slope is observed for bigger nanocrystals. In between, there is a radius where the nanocrystal is at equilibrium. Before that radius is reached, bigger nanocrystals will grow faster than the smaller ones leading to a defocusing of the size distribution.[20;25] In turn, when the slope is negative, smaller nanocrystals will grow faster than bigger ones. This is the focusing regime, where the size dispersion narrows. Importantly, the defocusing regime is larger when the supersaturation of the monomers decreases. This focusing regime is highly desired during any nanocrystal synthesis. It will ensure sharp size distributions, which is important for a whole range of applications.

The theories and concepts as described above, allow for a better comprehension of the hot injection synthesis. Several mechanistic studies have lead to improved results in terms of size control or size dispersion, or have lead to

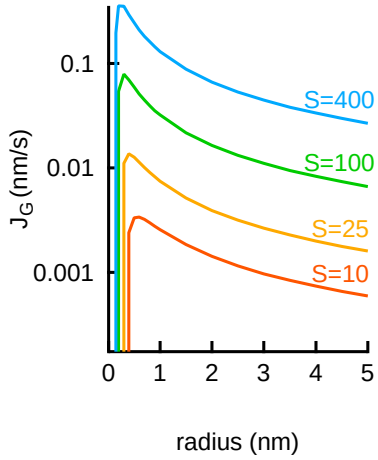

Figure 1.5: Growth rate as function of nanocrystal radius for supersaturation equal to 10 (orange), 25 (yellow), 100 (green) and 400 (blue).

the production of new nanomaterials. The following examples demonstrate that both elucidation of the chemical reaction equation and the study of the variation of nanocrystal properties with altered reaction chemistry can cause advances in field. In 2007, Liu *et al.* proposed a reaction mechanism for ME nanocrystals (M=Cd, Zn, E= S, Se, Te) formed out of tri-n-butylphosphine chalcogenides and an oleic acid or phosphonic acid complex of cadmium or zinc in a noncoordinating solvent.[26] The trialkylphosphine chalcogenides deoxygenate the oleic acid or phosphonic acid surfactant to generate trialkylphosphine oxide and oleic or phosphonic acid anhydride products. Hereby, the importance of ligands in the reaction mixture was demonstrated. Three years later, this team discovered that the precursor conversion limits the rate of nanocrystal nucleation and growth and they linked the initial precursor reaction rate to the number of NCs formed at the end of the reaction.[27] Hereby, they suggested a mechanism where the precursors react in an irreversible step that supplies the reaction medium with a solute form of the semiconductor.

Abe *et al.* showed that the diameter of colloidal nanocrystals at the end of the size distribution focusing depends on the reaction rate in a hot injection synthesis.[28] Simulations indicated that the postfocused diameter is reached at almost full yield and that it can be adjusted by the rate of monomer formation. After demonstrating that the reaction rate depends in first order

on the Cd and Se precursor concentration with simulations, this size-tuning strategy was implemented in actual experiments by varying the precursor concentration. This enabled the synthesis of colloidal nanocrystals with a predefined size at almost full yield and sharp size distributions.

Raising the concentration of free acid in the hot injection synthesis of colloidal nanocrystals increases the diameter of the resulting nanocrystals. Abe *et al.* showed that this has the same effect on a real synthesis as raising the solute solubility in simulations.[24] Since free acids are used to coordinate the cation precursors in the preformed syntheses, this led to a meaningful link between a parameter in reaction simulations and the composition of an experimental reaction mixture.

1.3 Surface chemistry

Quantum dots are obtained as a colloidal dispersion which is sterically stabilized by molecules that are called ligands in the jargon. They are often organic molecules, with a functional head group and a long aliphatic chain, that play a very important role in deciding the shape and size of the nanocrystals during the synthesis. Ligands can limit the growth rate of specific lattice planes during the synthesis leading to the growth of rods, tetrapods or wires.[13;29] Afterwards, it can be beneficial to obtain information about the inorganic/organic interface. After all, these ligands determine a great deal of the physicochemical properties of the quantum dots. They determine in which solvents the quantum dots can be suspended and the stability of that dispersion. If the quantum dots cannot be suspended in the preferred solvent, a ligand exchange is desirable. The opto-electronic properties of the quantum dot are influenced by the ligands as well.[30] Replacing the long organic ligands for shorter (in)organic ligands can improve the mobility in QD films.[31] Moreover, surface atoms have a weaker bond since they are undercoordinated which can create energy levels in the semiconductor band gap, so-called *trap states*. Ligands coordinate the surface atoms and can *passivate* the trap states. Hence, even the photoluminescence quantum yield can be dependent on the type of ligand and the ligand density.[32;33] Consequently, an in-depth knowledge of the surface chemistry is mandatory for fabricating high quality of QDs.

Ligands can be classified using the Covalent Bond Classification as depicted in Figure 1.6.[33–35] An X-type ligand is a one-electron donor (anionic or cationic) which will covalently bind to the quantum dot to form a neutral object. A carboxylic acid is a typical example. L-type ligands are two-electron donors (neutral lewis bases) undergoing a dative covalent bond with

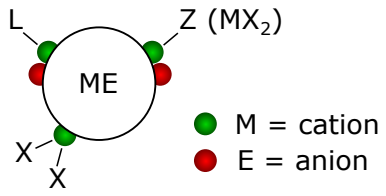

Figure 1.6: Ligands can be classified using the Covalent bond classification. There are L-type, Z-type and X-type ligands.

the nanocrystal surface. Amines are classic L-type ligands. Z-type ligands are two-electron acceptors (lewis acids). A cadmium carboxylate complex can be viewed as a Z-type ligand. It can reversibly bind to and dissociate from the nanocrystal surface.[33] The type of bond greatly depends on the stoichiometry of the nanocrystal. If the nanocrystal is stoichiometric, only a neutral ligand can bind to the quantum dot surface, whereas a nanocrystal with a metal-rich surface needs anionic X-type ligands to ensure neutrality of the overall particle.

Identification and knowledge of the ligand shell can be of great importance. A number of techniques like X-ray photoelectron spectroscopy (XPS), mass spectrometry (MS) or Fourier transform infrared (FTIR) can be useful although none of them actually can provide information about the ligand density or can distinguish between bound and free ligands. A technique that is capable of doing that is nuclear magnetic resonance spectroscopy (NMR). Nowadays, NMR is a widely used technique to study nanocrystal dispersions in a nondestructive way. One dimensional NMR measurements provide information about the type of ligands present in dispersion, the ligand density and the purity of the sample. Resonances of bound ligands will be broadened in the NMR spectrum, which makes them very recognizable. An *in-situ* ligand exchange can reveal the type of binding to the nanocrystal and the relative binding strength of these ligands. In addition, diffusion ordered spectroscopy (DOSY) provides a diffusion coefficient for every resonance in the spectrum. Hence, a distinction can be made between free, exchanging and tightly bound ligands. The hydrodynamic diameter of the nanocrystals can be determined as well. Nuclear Overhauser effect spectroscopy (NOESY) will indicate if a specific molecule spends time on the QD surface, even if it appears to be a sharp resonance in the one dimensional spectrum. Relaxation measurements and spectral hole burning experiments can provide information about ligand-nanocrystal interaction or the heterogeneity of the broadening of the resonances.

The NMR story started more than 20 years ago, when some initial studies used proton NMR to obtain information about the ligand binding.[36–38] For example, Majetich *et al.* studied CdSe quantum dots capped with thiolates.[37] Only later on NMR was utilized in more elaborate studies. In 2005, for example, Hens *et al.* published a paper about the study of the InP surface chemistry.[39] The ligands bound to the nanocrystal surface after purification were identified using a variety of NMR techniques. The amount of ligands per surface area, the ligand density, was determined as well. With DOSY, a distinction between bound and free resonances was made and the hydrodynamic diameter of the nanocrystals was determined. Afterward, an exchange of ligands to pyridine was performed and a dynamic adsorption/desorption process of the ligands was discovered for that system. Already in that paper a lot of the NMR techniques known today as *the NMR toolbox for nanocrystals* were used.

In 2007, proton and phosphorous NMR was utilized in the mechanistic study about metal chalcogenide quantum dots described in the previous section.[26] This demonstrates that NMR is not only useful to study the nanocrystal after synthesis, but it is also effective to elucidate reactions taking place during the synthesis.

Fritzinger *et al.* published a paper about the relevance of NOESY in 2009.[40] This technique allows for a confirmation of nanocrystal-ligand interactions, even if ligands undergo fast adsorption to and desorption from the nanocrystal surface. Using oleic acid with deuterated carboxyl group, the same authors demonstrated that oleic acid ligands on CdSe nanocrystals are bound as oleate ions and not as oleic acid molecules.[41] This explained why there is no adsorption/desorption process without the presence of excess free oleic acid molecules in this case. Later on, the NMR toolbox was able to differentiate between strongly bound ligands like phosphonic acids and weakly bound acids like amines[42–44] and it proved that the photoluminescence is quenched by the stripping of carboxylates off the nanocrystal surface as well.[45] Because of its versatility, NMR will be the main technique for characterisation used in this work. The next chapter will introduce all NMR techniques used in this work.

1.4 Outline

Following the widespread use of colloidal nanocrystals as a model system to explore and understand the properties of nanoscale materials and their implementation as active material in various applications, a good control over their production is necessary. To gain control over their production,

knowledge about the reaction mechanism is crucial. Therefore, mechanistic studies have become a hot topic in the field. In the first chapter the mechanism to form InP nanocrystals is studied. The InP nanocrystals are synthesized using an economical synthesis with aminophosphines and indiumhalides ($InCl_3$, InI_3, $InBr_3$). This is not a straightforward synthesis since aminophosphines are P^{III} compounds, such that intermediate reduction steps are needed to form InP in a reaction with an In^{III} precursor. The elucidation of this mechanism could lead to the improvement of the synthesis or the economical production of other III-V nanocrystals.

In the second chapter, we investigate the relation between the chain length of ligands used and the outcome of the CdSe nanocrystals hot injection synthesis. The size and size distribution and the yield development are studied for various carboxylic acids, amines and phosphine oxides. Thereafter, the observations are linked to the nucleation and growth rate. This study can provide insights in the precursor conversion chemistry and may lead to an efficient tuning strategy for the hot injection synthesis.

In the third chapter, we describe an NMR method for gaining insight in the ligand distribution on the nanocrystal surface. Spectral hole burning experiments are used to examine the surface chemistry of CdSe and PbSe quantum dots capped with oleate ligands. These oleates are very suitable for NMR studies thanks to their isolated alkene resonance at $\approx 5.6 - 5.7$ ppm. The spectral hole burning experiments can provide a great deal of information about the ligand shell of nanocrystals. On the one hand, the heterogeneity of the oleate alkene resonance is determined. The occurrence of a spectral hole is a sign of heterogeneity of a broad resonance.[39] For QDs, the heterogeneity could originate from a different configuration or orientation of the ligand or a different chemical environment. On the other hand, a spectral hole burning experiment can provide information about the ligand shell structure. When a series of spectral hole burning experiments is performed where the specific waiting time introduced between the saturation and the actual recording of the spectrum is increased, a spectral hole burning recovery can be measured. The recovery of a spectral hole reflects the loss of the irradiation induced transparency. This is caused either by spin-lattice relaxation or by a transfer of saturation to other parts of the resonance. The latter could involve an Nuclear Overhauser effect (nOe) type of transfer or it could be caused by each molecule slowly sampling a relatively broad configuration - and thus chemical shift - space either because they reorient or move to other locations on the nanocrystal.

The final chapter comprises a combined experimental and theoretical study on two-component ligand shells of colloidal quantum dots made by ligand

exchange. The model system of oleate-capped CdSe quantum dots is exposed to other fatty acids. Stepwise, the composition of the ligand shell is determined in function of the amount of acid added with 1D proton NMR measurements. Here the difference between linear and bulky carboxylic acids is highlighted. This study has important implications for ligand exchanges and the fabrication of particles with binary ligand shells.

1.5 Scientific output

1.5.1 Publications in international journals

1. Antti Hassinen, Iwan Moreels, Kim De Nolf, Philippe F. Smet, José C. Martins and Zeger Hens. *Short-Chain Alcohols Strip X-Type Ligands and Quench the Luminescence of PbSe and CdSe Quantum Dots, Acetonitrile Does Not.* Journal of the American Chemical Society, 134 (51): 20705-20712. 2012

2. Stijn Flamee, Marco Cirillo, Sofie Abe, Kim De Nolf, Raquel Gomes, Tangi Aubert and Zeger Hens. *Fast, High Yield, and High Solid Loading Synthesis of Metal Selenide Nanocrystals.* Chemistry of Materials, 25 (12): 2476-2483. 2013

3. Antti Hassinen, Raquel Gomez, Kim De Nolf, Qiang Zhao, André Vantomme, José C. Martins and Zeger Hens. *Surface Chemistry of CdTe Quantum Dots Synthesized in Mixtures of Phosphonic Acids and Amines: Formation of a Mixed Ligand Shell.* The Journal of Physical Chemistry C, 117 (27): 13936-13943. 2013

4. Ruben Dierick, Freya Van den Broeck, Kim De Nolf, Qiang Zhao, André Vantomme, José Martins and Zeger Hens. *Surface chemistry of $CuInS_2$ colloidal nanocrystals, tight binding of L-type ligands.* Chemistry of Materials, 26 (20): 5950-5957. 2014

5. Mickael D. Tessier, Dorian Dupont, Kim De Nolf, Jonathan De Roo, and Zeger Hens. *Economic and Size-Tunable Synthesis of InP/ZnE (E = S, Se) Colloidal Quantum Dots.* Chemistry of Materials, 27 (13): 4893-4898. 2015

6. Kim De Nolf, Richard K. Capek, Sofie Abe, Michael Sluydts, Youngjin Jang, José C. Martins, Stefaan Cottenier, Efrat Lifshitz and Zeger Hens. *Controlling the Size of Hot Injection Made Nanocrystals by Manipulating the Diffusion Coefficient of the Solute.* Journal of the American Chemical Society, 137 (7): 2495-2505. 2015

7. Mickael D. Tessier, Kim De Nolf, Dorian Dupont, Davy Sinnaeve, Jonathan De Roo, Zeger Hens. *Aminophosphines: a Double Role in the Synthesis of Colloidal Indium Phosphide Quantum Dots.* Journal of the American Chemical Society, 138 (18): 5923-5929. 2016

1.5.2 First author conference contributions

1. Kim De Nolf, Freya Van Den Broeck, Antti Hassinen, Sofie Abe, José C. Martins and Zeger Hens. *Water Soluble Quantum Dots for Bioimaging, an NMR Study.* 2012. Young Belgian Magnetic Resonance Scientist (YBMRS), 11th Symposium, Spa (Belgium). Poster

2. Kim De Nolf, Freya Van den Broeck, Antti Hassinen, Sofie Abé and Zeger Hens. *Water soluble quantum dots for bioimaging, an NMR study.* 2013. NWO Study Group Physics and Materials meeting, Veldhoven (The Netherlands). Poster

3. Kim De Nolf, Antti Hassinen, Iwan Moreels, Philippe F. Smet, Zeger Hens, José C. Martins. *Using NMR to Shine Light on the Origin of Luminescence Quenching of PbSe and CdSe Quantum Dots processed with Certain Protic Solvents.* 2013. Young Belgian Magnetic Resonance Scientist (YBMRS), 12th Symposium, Blankenberge (Belgium). Poster

4. Kim De Nolf, Richard K Capek, Sofie Abé, Youngjin Jang, Efrat Lifshitz and Zeger Hens. *Length matters: how the ligand chain length affects the nanocrystal size in the hot injection synthesis.* 2013. European Materials Research Society (E-MRS), Lille (France). Talk

5. Kim De Nolf, Mickaël Tessier, Dorian Dupont, Jonathan De Roo, Davy Sinnaeve, Pieter Surmont, José C. Martins and Zeger Hens. *Unravelling the synthesis mechanism of colloidal InP nanocrystals.* 2015. Young Belgian Magnetic Resonance Scientist (YBMRS), 14th Symposium, Blankenberge (Belgium). Talk

6. Kim De Nolf, Jacek J Jasieniak, José C. Martins and Zeger Hens. *Influence of ligand shape and steric hindrance on the composition of the nanocrystal ligand shell* 2015. Young Belgian Magnetic Resonance Scientist (YBMRS), 14th Symposium, Blankenberge (Belgium). Poster

7. Kim De Nolf, Jacek J Jasieniak, José C. Martins and Zeger Hens. *Influence of ligand shape and steric hindrance on the composition of the nanocrystal ligand shell* 2016. Materials Research Society (MRS) spring meeting, Phoenix (USA). Poster

References

[1] Dmitri V. Talapin, Jong-Soo Lee, Maksym V. Kovalenko, and Elena V. Shevchenko. *Prospects of Colloidal Nanocrystals for Electronic and Optoelectronic Applications.* Chemical Reviews, 110(1):389–458, 2010.

[2] Talha Erdem and Hilmi Volkan Demir. *Color Science of nanocrystal quantum dots for lighting and displays.* Nanophotonics, 2(1):57–81, 2013.

[3] Paul Alivisatos. *Nanocrystals: Building blocks for modern materials design.* Endavour, 21(2):56–60, 1997.

[4] L. E. Brus. *Electron-Electron and Electron-Hole Interactions in Small Semiconductor Crystallites - the Size Dependence of the Lowest Excited Electronic State.* Journal of chemical physics, 80(9):4403–4409, 1984.

[5] Catherine J. Murphy. *Optical Sensing with Quantum Dots.* Analytical Chemistry, 74(19):520 A–526 A, 2002.

[6] Paul Alivisatos. *Semiconductor clusters, nanocrystals, and quantum dots.* Science, 271(5251):933–937, 1996.

[7] P. Martyniuk and Antoni Rogalski. *Quantum-dot infrared photodetectors: Status and outlook.* Progress in Quantum Electronics, 32(3-4):89–120, 2008.

[8] Christopher B Murray, David J. Norris, and Moungi G. Bawendi. *Synthesis and Characterisation of Nearly Monodisperse CdE (E = S, Se, Te) Semiconductor Nanocrystallittes.* Journal of the American Chemical Society, 115(19):8706–8715, 1993.

[9] Celso de Mello Donega, Peter Liljeroth, and Daniel Vanmaekelbergh. *Physicochemical evaluation of the hot-injection method, a synthesis route for monodisperse nanocrystals.* Small, 1(12):1152–1162, 2005.

[10] Celso de Mello Donega, Stephen G. Hickey, Sander F. Wuister, Daniel Vanmaekelbergh, and Andries Meijerink. *Single-Step Synthesis to Control the Photoluminescence Quantum Yield and Size Dispersion of CdSe Nanocrystals.* The Journal of physical chemistry B, 107(2):489–496, 2003.

[11] Dmitri V. Talapin, Nikolai Gaponik, Holger Borchert, Andrey L. Rogach, Markus Haase, and Horst Weller. *Etching of Colloidal InP Nanocrystals with Fluorides: Photochemical Nature of the Process Resulting*

in High Photoluminescence Efficiency. The Journal of physical chemistry B, 106(49):12659–12663, 2002.

[12] Christopher B Murray, Shouheng Sun, Wolfgang Gaschler, H Doyle, TA Betley, and Cherry R Kagan. *Colloidal synthesis of nanocrystals and nanocrystal superlattices.* IBM Journal of Research and Development, 45(1):47–56, 2001.

[13] Liberato Manna, Erik C. Scher, and A. Paul Alivisatos. *Synthesis of Soluble and Processable Rod-, Arrow-, Teardrop-, and Tetrapod-Shaped CdSe Nanocrystals.* Journal of the American Chemical Society, 122(51):12700–12706, 2000.

[14] Xiaogang Peng. *Mechanisms for the shape-control and shape-evolution of colloidal semiconductor nanocrystals.* Advanced Materials, 15(5):459–463, 2003.

[15] Margaret A. Hines and Philippe Guyot-Sionnest. *Synthesis and Characterization of Strongly Luminescing ZnS-Capped CdSe Nanocrystals.* The Journal of physical chemistry, 100(2):468–471, 1996.

[16] J Jack Li, Y Andrew Wang, Wenzhuo Guo, Joel C Keay, Tetsuya D Mishima, Matthew B Johnson, and Xiaogang Peng. *Large-scale synthesis of nearly monodisperse CdSe/CdS core/shell nanocrystals using air-stable reagents via successive ion layer adsorption and reaction.* Journal of the American Chemical Society, 125(41):12567–75, 2003.

[17] Marco Cirillo, Tangi Aubert, Raquel Gomes, Rik Van Deun, Philippe Emplit, Amelie Biermann, Holger Lange, Christian Thomsen, Edouard Brainis, and Zeger Hens. *"Flash" Synthesis of CdSe/CdS Core - Shell Quantum Dots.* Chemistry of Materials, 26:1154–1160, 2014.

[18] Mark P. Hendricks, Michael P. Campos, Gregory T. Cleveland, Ilan Jen-La Plante, and Jonathan S. Owen. *A tunable library of substituted thiourea precursors to metal sulfide nanocrystals.* Science, 348(6240):1226–1230, 2015.

[19] Soon Gu Kwon and Taeghwan Hyeon. *Formation Mechanisms of Uniform Nanocrystals via Hot-Injection and Heat-Up Methods.* Small, 7(19):2685–2702, 2011.

[20] Sofie Abe, Richard K. Capek, Bram De Geyter, and Zeger Hens. *Tuning the postfocused size of colloidal nanocrystals by the reaction rate: from theory to application.* Acs Nano, 6(1):42–53, 2012.

[21] Kim De Nolf, Richard K. Capek, Sofie Abe, Michael Sluydts, Youngjin Jang, Jose C. Martins, Stefaan Cottenier, Efrat Lifshitz, and Zeger Hens. *Controlling the Size of Hot Injection Made Nanocrystals by Manipulating the Diffusion Coefficient of the Solute.* Journal of the American Chemical Society, 137(7):2495–2505, 2015.

[22] Victor K. LaMer and Robert H. Dinegar. *Theory, Production and Mechanism of Formation of Monodispersed Hydrosols.* Journal of the American Chemical Society, 72(11):4847–4854, 1950.

[23] Dmitri V. Talapin, Andrey L. Rogach, Markus Haase, and Horst Weller. *Evolution of an ensemble of nanoparticles in a colloidal solution: Theoretical study.* Journal of Physical Cemistry B, 105(49):12278–12285, 2001.

[24] Sofie Abe, Richard K. Capek, Bram De Geyter, and Zeger Hens. *Reaction Chemistry/Nanocrystal Property Relations in the Hot Injection Synthesis, the Role of the Solute Solubility.* ACS Nano, 7(2):943–949, 2013.

[25] Xiaogang Peng, Jacob Wickham, and Paul Alivisatos. *Kinetics of II-VI and III-V Colloidal Semiconductor Nanocrystal Growth: "Focusing" of Size Distributions.* Journal of the American Chemical Society, 120(21):5343–5344, 1998.

[26] Haitao Liu, Jonathan S. Owen, and A. Paul Alivisatos. *Mechanistic study of precursor evolution in colloidal group II-VI semiconductor nanocrystal synthesis.* Journal of the American Chemical Society, 129(2):305–312, 2007.

[27] Jonathan S. Owen, Emory M. Chan, Haitao Liu, and A. Paul Alivisatos. *Precursor Conversion Kinetics and the Nucleation of Cadmium Selenide Nanocrystals.* Journal of the American Chemical Society, 132(51):18206–18213, 2010.

[28] Sofie Abe, Richard Karel Capek, Bram De Geyter, and Zeger Hens. *Tuning the Postfocused Size of Colloidal Nanocrystals by the Reaction Rate: From Theory to Application.* ACS Nano, 6(1):42–53, 2012.

[29] Yadong Yin and Paul Alivisatos. *Colloidal nanocrystal synthesis and the organic-inorganic interface.* Nature, 437(7059):664–670, 2005.

[30] Jonathan Owen. *The coordination chemistry of nanocrystal surfaces.* Science, 347(6222):615–616, 2015.

[31] Jong-Soo Lee, Maksyn V. Kovalenko, Jing Huang, Dae Sung Chung, and Dmitri V. Talapin. *Band-like transport, high electron mobility and high photoconductivity in all-inorganic nanocrystal arrays.* Nature Nanotechnology, 6(6):348–352, 2011.

[32] Jacek Jasieniak and Paul Mulvaney. *From Cd-rich to Se-rich - The manipulation of CdSe nanocrystal surface stoichiometry.* Journal of the American Chemical Society, 129(10):2841–2848, 2007.

[33] Nicholas C. Anderson, Mark P. Hendricks, Joshua J. Choi, and Jonathan S. Owen. *Ligand Exchange and the Stoichiometry of Metal Chalcogenide Nanocrystals: Spectroscopic Observation of Facile Metal-Carboxylate Displacement and Binding.* Journal of the American Chemical Society, 135(49):18536–18548, 2013.

[34] Malcolm L.H. Green. *A New Approach to the Formal Classification of Covalent Compounds of the Elements.* Journal of Organometallics Chemistry, 500(1-2):127–148, 1995.

[35] Jonathan De Roo, Katrien De Keukeleere, Zeger Hens, and Isabel Van Driessche. *From ligands to binding motifs and beyond; the enhanced versatility of nanocrystal surfaces.* Dalton Transactions, 45:13277–13283, 2016.

[36] Joseph R. Sachleben, Vicki Colvin, Lyndon Emsley, E. Wrenn Wooten, and Paul Alivisatos. *Solution-state NMR studies of the surface structure and dynamics of semiconductor nanocrystals.* Journal of physical chemistry B, 102(50):10117–10128, 1998.

[37] Sara A. Majetich, Adriaan C. Carter, John Belot, and Richard D. McCullough. *^{1}H NMR Characterization of the CdSe Nanocrystallite Surface.* The Journal of physical chemistry, 98(51):13705–13710, 1994.

[38] Jose Aldana, Y. Andrew Wang, and Xiaogang Peng. *Photochemical Instability of CdSe Nanocrystals Coated by Hydrophilic Thiols.* Journal of the American Chemical Society, 123(36):8844–8850, 2001.

[39] Zeger Hens, Iwan Moreels, and José C. Martins. *In situ ^{1}H NMR study on the triOctylphosphine oxide capping of colloidal InP nanocrystals.* Chemphyschem, 6(12):2578–2584, 2005.

[40] Bernd Fritzinger, Iwan Moreels, Petra Lommens, Rolf Koole, Zeger Hens, and José C. Martins. *In Situ Observation of Rapid Ligand Exchange in Colloidal Nanocrystal Suspensions Using Transfer NOE Nuclear Magnetic Resonance Spectroscopy.* Journal of the American Chemical Society, 131(8):3024–3032, 2009.

[41] Bernd Fritzinger, Richard K. Capek, Karel Lambert, Jose C. Martins, and Zeger Hens. *Utilizing Self-Exchange To Address the Binding of Carboxylic Acid Ligands to CdSe Quantum Dots.* Journal of the American Chemical Society, 132(29):10195–10201, 2010.

[42] Raquel Gomes, Antti Hassinen, Agnieszka Szczygiel, Qiang Zhao, Andre Vantomme, Jose C. Martins, and Zeger Hens. *Binding of Phosphonic Acids to CdSe Quantum Dots: A Solution NMR Study.* Journal of physical chemistry Letters, 2(3):145–152, 2011.

[43] Antti Hassinen, Raquel Gomes, Kim De Nolf, Qiang Zhao, Andre Vantomme, Jose C. Martins, and Zeger Hens. *Surface Chemistry of CdTe Quantum Dots Synthesized in Mixtures of Phosphonic Acids and Amines: Formation of a Mixed Ligand Shell.* Journal of physical chemistry C, 117(27):13936–13943, 2013.

[44] Antti Hassinen, Iwan Moreels, Celso de Mello Donega, Jose C. Martins, and Zeger Hens. *Nuclear Magnetic Resonance Spectroscopy Demonstrating Dynamic Stabilization of CdSe Quantum Dots by Alkylamines.* Journal of physical chemistry Letters, 1(17):2577–2581, 2010.

[45] Antti Hassinen, Iwan Moreels, Kim De Nolf, Philippe F. Smet, Jose C. Martins, and Zeger Hens. *Short-Chain Alcohols Strip X-Type Ligands and Quench the Luminescence of PbSe and CdSe Quantum Dots, Acetonitrile Does Not.* Journal of the American Chemical Society, 134(51):20705–20712, 2012.

2

NMR Toolbox for Nanocrystals

NMR is a powerful technique to study quantum dots. Its most relevant feature is the ability to distinguish molecules bound to the nanoparticle surface from free species. In this chapter the essential techniques to study quantum dots are introduced. These techniques are often referred to as the NMR toolbox for nanocrystals.

2.1 Introduction

NMR is a technique which uses the magnetic properties of nuclides. Nuclei of all atoms are characterized by a nuclear spin quantum number I. Its value is a multiple of $1/2$ and is never lower than zero. The nuclei posses an angular momentum P, which gives rise to an associated magnetic moment μ, where $\mu = \gamma P$. The term γ is the gyromagnetic constant and will depend on the type of nuclide involved. When placed in an external magnetic field, the magnetic moments align themselves in a discrete number of orientations $2I + 1$ relative to the field since their energy states are quantized. Nuclei with spin quantum number $I = 1/2$ - such as ^{1}H, ^{13}C, ^{15}N, ^{31}P - will have access to two levels. Some of them will be parallel to the magnetic field (α state) and others will be anti-parallel (β state). The static magnetic field

imposes a torque on the spins causing a precession of the spin about the magnetic field. This is referred to as the Larmor precession and is defined by the Larmor frequency:

$$\nu = \frac{-\gamma B_0}{2\pi} \tag{2.1}$$

Here, γ is the gyromagnetic constant and B_0 is the applied static magnetic field. Electromagnetic radiation with a frequency equal to the Larmor precession can be absorbed by the nucleus causing it to change spin state. Indeed, the energy difference between the α and β state is given by:

$$\Delta E = h\nu = \frac{h\gamma B_0}{2\pi} \tag{2.2}$$

The energy splitting is small compared to thermal noise in the environment which makes NMR spectroscopy a very insensitive technique. The population difference is of importance here. If both states are equally populated, it is referred to as a saturated system without observable nuclear magnetic resonance. The ratio of the populations in the α and β states in the presence of B_0 static field is expressed by:

$$\frac{N_\alpha}{N_\beta} = \exp\left(\frac{-\Delta E}{k_B T}\right) \tag{2.3}$$

Here, k_B is the Boltzmann constant, T is temperature and ΔE is the energy difference between both states given by Equation 2.2. With respect to directions orthogonal to B_0, the individual magnetic moments are randomly distributed. Therefore, the small population excess can be represented by a bulk magnetic vector M_0 along the static magnetic field B_0 (Figure 2.1a). This orientation is referred to as the z-axis by convention.

NMR spectroscopy now uses electromagnetic radiation to induce transitions between the energy levels. A time-dependent magnetic field B_1, oscillating at Larmor frequency, in the transverse plane will affect the bulk magnetization M_0. To comprehend its influence on the bulk magnetization, the so-called rotating frame of reference is employed.[1] If the rf pulse is applied along the x-axis, the bulk magnetization will rotate in the direction of the y-axis (Figure 2.1b). The strength of the rf pulse will determine the rate of the rotation of the magnetization and the angle through which it turns is determined by the amplitude and duration of the rf pulse. If the pulse is stopped when the bulk magnetization reaches the xy-plane, we refer to this as a 90° pulse (Figure 2.1c). Since spin excitation only occurs when

[1] More information about the rotating frame of reference and other NMR concepts can be found in the book of Timothy D.W. Claridge: *High-Resolution NMR Techniques in Organic Chemistry, 2nd edition*, Elsevier, 2008

the magnetic component of the rf is oscillating at the Larmor frequency, a pulse can be applied to protons without exciting carbons for example.

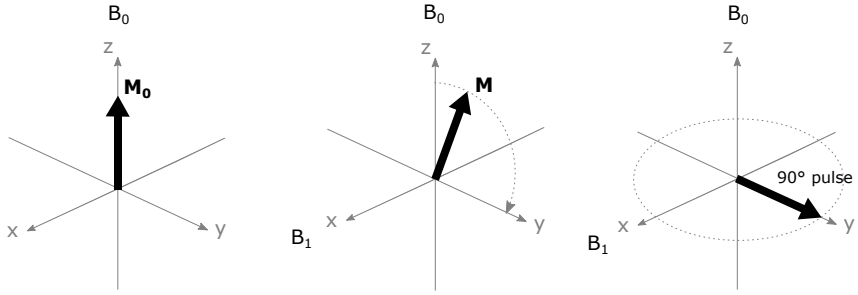

Figure 2.1: The bulk magnetization M_0 is first aligned with the static magnetic field B_0. When a time-dependent magnetic field B_1 is applied along the x-axis, the bulk magnetization will rotate in the direction of the y-axis. If the pulse is stopped when the bulk magnetization reaches the xy-plane, we refer to this as a 90° pulse.

After applying a pulse, the magnetization will return to its original orientation along the magnetic field. This is called relaxation. The relaxation process is a relatively slow process compared to for example optical spectroscopy. Hence, it is advantageous because it yields a narrow line width for the NMR resonances and the opportunity to manipulate spins after the initial perturbation. Relaxation occurs via two different processes. Longitudinal relaxation, often referred to as spin-lattice relaxation or T_1 relaxation, is related to the population difference. If the system is perturbed in such a way that the population of the α and β states are equal, no magnetization along the z-axis is observed. In time, the spins will go back from the excited state to the ground state to recover the original situation. The magnetization along the z-axis, M_Z, will gradually recover with an exponential recovery, expressed by

$$M_Z(t) = M_0\Big[1 - n\exp\Big(\frac{-t}{T_1}\Big)\Big] \tag{2.4}$$

In Equation 2.4, n is a factor dependent on the pulse angle, M_Z is the magnetization along the z-axis at time t, M_0 is the original magnetization along the z-axis and T_1 is the time constant. T_1 can vary anywhere between a few milliseconds and even a few minutes. The energy involved is transferred to the surroundings in the form of heat, giving rise to the name spin-lattice relaxation. For spins to relax fully after a 90° pulse, a waiting period of

$5T_1$ is desirable. Hence, knowledge of T_1 is important to conduct NMR experiments in practice.

Transverse or T_2 relaxation, is the second relaxation process. In an unperturbed situation there is no magnetization in the xy-plane because all spins are randomly oriented in that plane. When applying a pulse, the spins posses phase coherence. This phase coherence will disappear since all spins experience a slightly different magnetic field, causing them to precess slightly faster or slower than the others. Hence, after a while the magnetization in the xy-plane disappears again. This is referred to as translational relaxation, characterized by a time constant T_2. T_2 is more or less inversely proportional with size, meaning that small, fast tumbling molecules will have long T_2 relaxation time constants. The line width of the resonances at half maximum $\Delta\nu_{1/2}$ depends on the T_2 time constant:

$$\Delta\nu_{1/2} = \frac{1}{\pi T_2} \tag{2.5}$$

Hence, the line width of resonance corresponding to large molecules will be large.

Since the magnetization along the z-axis cannot be restored completely if there is still magnetization in the xy-plane, T_2 cannot be longer than T_1. Both T_1 and T_2 can be measured with specially designed experiments.[1] This relaxation cannot occur spontaneous. A magnetic field oscillating at a frequency corresponding to the transition can induce relaxation. There are four main pathways of relaxation: dipole-dipole, chemical shift anisotropy, spin rotation and quadrupolar mechanisms. Dipole-dipole relaxations occur when a spin influences the local magnetic field of its neighbor. Depending on the relative orientation of both nuclei, a nucleus can weaken or strengthen the local magnetic field experienced by its neighbor, which will be time-dependent due to the rotational motion of the molecules. To induce these transitions, the molecule has to tumble at a specific rate, to produce the right fluctuating field. More information about dipole-dipole relaxation and the other mechanisms, can be found in the book of Timothy D.W. Claridge.[1]

2.2 One dimensional Proton NMR

The one dimensional proton NMR spectrum of ligands bound to a nanocrystal exhibits remarkable differences compared to that of the free species in solution. Figure 2.2 shows the NMR spectrum of oleic acid (OAc) capped CdSe quantum dots and a reference of oleic acid without nanocrystals in toluene-d8. One can observe that the line width of the resonances in the

quantum dot spectrum is remarkably broader than that of the reference spectrum. In contrast to small molecules, ligands attached to a nanoparticle will exhibit a slower tumbling rate and a faster transverse relaxation rate, as described in the paragraph above.

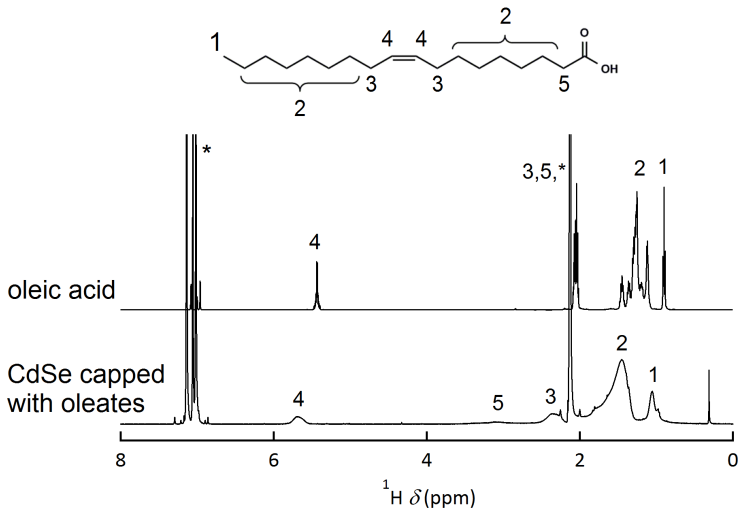

Figure 2.2: One dimensional ^{1}H spectrum of oleates bound to CdSe quantum dots and a reference spectrum of oleic acid in toluene-d8. The resonances are labeled with numbers $1-5$, indicating their position in the oleic acid molecule, or with a $*$, to indicate the solvent resonances.

Note that the resonances of oleate capped quantum dots have a slightly different chemical shift with respect to free oleic acid as well. The cause of this shift is the change in chemical environment in which the ligand is located when going from solution to ligand shell. In solution, it is completely surrounded by toluene molecules, an aromatic environment. When bound to the quantum dot, it is mostly surrounded by other ligands, an aliphatic environment. This difference in environment causes a change in chemical shift of the resonances. This shift will depend on the kind of solvent and the type of ligand used.

In quantitative 1D proton NMR measurements, the integration value of an NMR resonance is proportional to the number of nuclei corresponding to that resonance. In this way, the concentration of a certain species in solution can be determined. Formerly, the concentration determination was based on an internal standard in the sample. Nowadays, DIGITAL ERETIC (Electronic REference To access In Vivo Concentrations) is used.[1;2] ERETIC

generates a synthetic signal with a certain area in each spectrum. This area is calibrated once against a reference solution with a known concentration. Hence, the quantification of the unknown species is performed indirectly against the reference by means of the synthetic signal. Subsequently, the ligand density can be calculated if the volume of the sample and the size of the quantum dots are known.

2.3 Diffusion ordered spectroscopy[1;3;4]

DOSY is a technique which distributes the resonances of the 1D (^{1}H) spectrum according to their diffusion coefficient in the second dimension. In DOSY a pulsed field gradient is applied. The magnetic field of a pulsed field gradient with gradient strength g is deliberately inhomogeneous. A molecule at the bottom of the sample will not experience the same gradient field as a molecule in the middle of the sample and the precession frequency of the spins will depend on its position in the sample. Hence, the magnetization is completely dephased. When a second gradient with gradient strength -g is applied, all magnetization is rephased. However, molecules don't stay in the same position in the NMR sample while conducting a measurement. Therefore, not all magnetization will be rephased, leading to a decrease in signal intensity. The signal of a fast diffusing molecule will of course decrease more than that of a slow diffusion molecule. By repeating this experiment with different gradient strengths, a resonance decay is measured. A set of diffusion coefficients can extracted by analyzing the decays, which generates the second dimension of the DOSY spectrum. The signal intensity will decrease according to the Stejskal-Tanner equation[4]:

$$I = I_0 \exp(-D\gamma^2\delta^2 g^2(\Delta - \frac{\delta}{3})) \tag{2.6}$$

Here, I_0 is the original signal intensity, D is the diffusion coefficient, γ is the gyromagnetic constant, δ is the duration of the gradient, g is the gradient field strength and Δ is the time between the two gradients.

By means of the Stokes-Einstein relation, the diffusion coefficient can be linked to a hydrodynamic radius:

$$r_h = \frac{k_b T}{6\pi\eta D} \tag{2.7}$$

Here, k_b is the constant of Boltzmann, T is the temperature, η is the viscosity of the solvent, r_h is the hydrodynamic radius and D is the diffusion coefficient. Figure 2.3 gives an example of a DOSY spectrum. Three clearly different diffusion coefficients can be discriminated which represent three

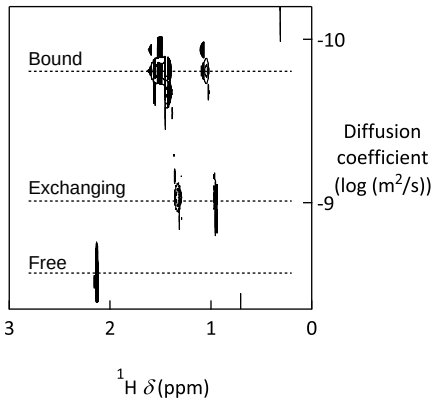

Figure 2.3: ^{1}H DOSY spectrum of oleates bound to PbS quantum dots in toluene-d8. Three diffusion coefficients can be distinguished: one for small molecules, one for molecules bound to nanocrystals and one weighted average between the bound and free state of fast exchanging ligands.

typical cases. Small molecules such as the solvent or ligands free in solution will diffuse more rapidly, generating a large diffusion coefficient. These molecules have small hydrodynamic radii. Larger molecules or bound ligands, will diffuse more slowly, generating a small diffusion coefficient. The hydrodynamic radius of ligands bound to the nanocrystal surface correspond to that of the nanocrystal itself including the ligand shell. Finally, dynamic ligands - species that spend some time on the nanocrystal surface and some time in solution - can give rise to two possible outcomes. If the exchange is fast compared to the diffusion time scale, dynamic ligands will exhibit a weighted average of both the free and bound state diffusion coefficients. For a slow exchange, on the other hand, the diffusion coefficient of both the bound and the free state will be visible.

2.4 Nuclear Overhauser effect spectroscopy[1;5]

nOe is a transfer of spin polarization from one spin to another via cross-relaxation. When observing two coupled spins, X and A, there are four states to be considered: $\alpha_X\alpha_A$, $\alpha_X\beta_A$, $\beta_X\alpha_A$ and $\beta_X\beta_A$ (Figure 2.4a). The $\alpha_X\alpha_A$ state will be more populated and the $\beta_X\beta_A$ state will be depleted. The transition between every state is characterized by one or more spin flips. The probability of transition between $\alpha_X\alpha_A$ and $\beta_X\beta_A$ is called the double quantum probability W_2 and the one between $\alpha_X\beta_A$ and $\beta_X\alpha_A$ the

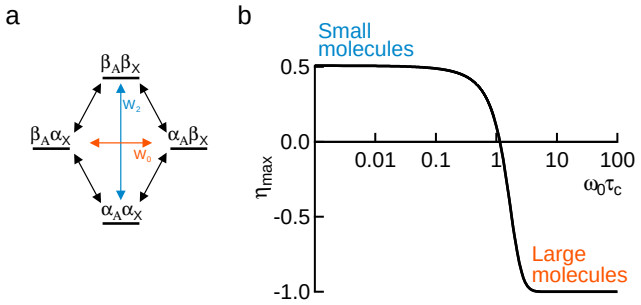

Figure 2.4: a) Energy diagram for two coupled spins A and X. b) The variation of the maximal theoretical nOe in a two-spin system as function of the molecular tumbling rate.

zero quantum probability W_0.

When spin X is saturated, its α and β populations are equalized. The nOe is an interplay between relaxation and this saturation. The saturation will equalize the $\alpha_X\alpha_A$ and the $\beta_X\alpha_A$ states as well as the $\alpha_X\beta_A$ and the $\beta_X\beta_A$ states, changing the population differences between the states for the X spin. Relaxation, on the other hand, will attempt to regain the equilibrium population differences for the X spin. As a result, the population difference across other transitions will also start to deviate from the original values. This is countered by the occurrence of zero and double quantum transitions with probability W_2 and W_0. These two processes are responsible for the nOe and are referred to as cross-relaxation pathways. W_2 will transfer population from the $\beta_X\beta_A$ to the $\alpha_X\alpha_A$ state. The recovery of the population differences between the X spin states will increase the population difference across the A spin states. This is a positive nuclear Overhauser effect. In contrast, W_0 will transfer population from the $\beta_X\alpha_A$ to the $\alpha_X\beta_A$ state. This will decrease the population difference across the A spin states, referred to as a negative nuclear Overhauser effect. These two cross-relaxation processes will compete with each other and the dominant process will determine the sign of the nOe.

NOESY will use this nuclear Overhauser effect to determine the proximity of protons since nOe can only occur when two protons are in each others vicinity. Cross peaks between two resonances will either show a negative nOe (same color as diagonal resonances) or a positive nOe (different color than diagonal resonances). As Figure 2.4 shows, the nOe will be positive for small, fast tumbling molecules and negative for large, slowly tumbling

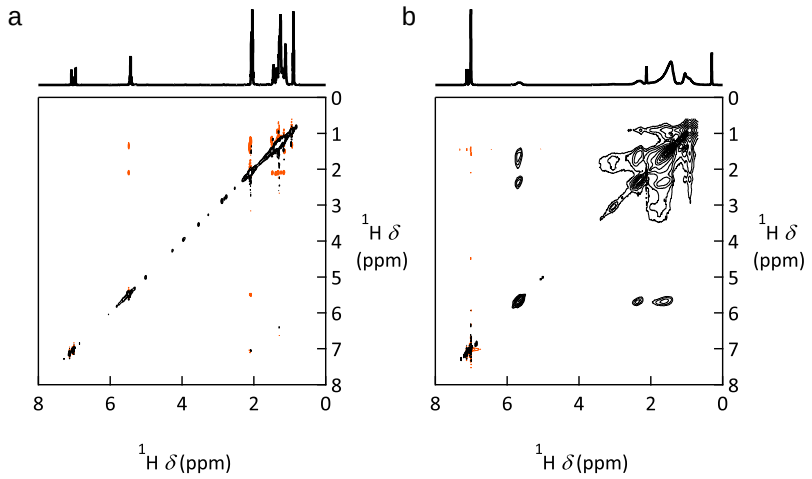

Figure 2.5: a) The NOESY spectrum exhibits small positive nOe's (orange) for non-interacting molecules (oleic acid in toluene-d8). b) Large negative nOe's (black) are visible in a NOESY spectrum of ligands interacting with quantum dots (oleate capped CdSe in toluene-d8).

molecules. Hence NOESY is the perfect technique to asses the interaction of the ligands with the quantum dots. If the ligands are not interacting with the quantum dots, small positive nOe's will be visible which are orange in this case (Figure 2.5a). A large negative nOe, on the other hand, will appear when there is interaction between the ligands and quantum dots, even if they are not tightly bound to the QD surface (Figure 2.5b). These cross peaks are black, the same color as the diagonal resonances.

2.5 Spectral hole burning[6]

In a spectral hole burning experiment a very narrow region of the NMR spectrum is saturated, which means the populations of the α and β states for spins inside this frequency range are equalized. Thereafter a 90° pulse is applied to record the actual spectrum as visualized in Figure 2.6. Hence, no signal is observed at the irradiated position. The outcome of the experiment is determined by the saturation position, the power level, the length of the saturation and the waiting time in between the saturation and the 90° pulse (the delay time). The width of the spectral hole burning region will be determined by both the length and the power level of the saturation.

A spectral hole burning experiment is used to determine if a broadened resonance is homogeneous or heterogeneous (Figure 2.7). On the one hand, the complete resonance can be attenuated indicating a homogeneous broadening of the resonance. On the other hand, a spectral hole can arise, suggesting a heterogeneous broadening of that resonance. A possible cause for heterogeneous broadening in ^{1}H NMR for nanocrystals can be the heterogeneity of the ligand environment which generates a distribution of chemical shifts.

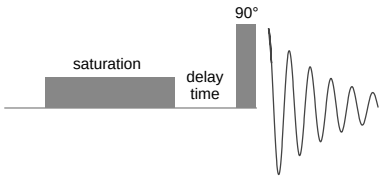

Figure 2.6: Pulse program of a hole burning experiment.

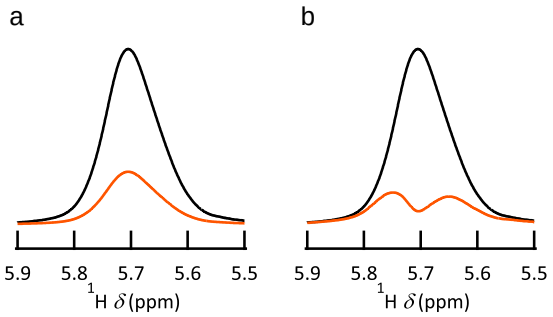

Figure 2.7: A hole burning experiment on a broadened resonance gives rise to two possible outcomes: a) attenuation of the complete resonance or b) a spectral hole.

If the spectral hole burning experiment leads to a spectral hole, it can be beneficial to study the recovery of the resonance to the original situation in the absence of saturation. In such an experiment, the resonance will be saturated, subsequently the resonance recovers during the delay time and finally the spectrum is recorded by applying a 90° pulse. This experiment is repeated with a different delay time used in every experiment (Figure 2.8). The spectral hole burning recovery series can provide information about the ligand heterogeneity and ligand shell structure since it reflects the recuperation of signal intensity. The loss is caused by spin lattice relaxation

or by a transfer of saturation to other parts of the resonance.

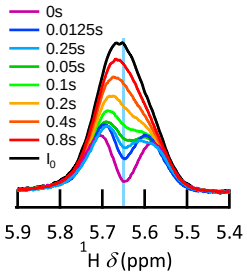

Figure 2.8: A recovery hole burning experiment performed on a broadened resonance.

2.6 Other frequently used NMR experiments

On top of all techniques mentioned in previous sections, homonuclear correlation experiments can be of particular use as well. Correlation spectroscopy (COSY) is a technique used to determine which proton spins are coupled to each other. This coupling always occurs through one or more bonds and cannot occur through space only, like in a NOESY experiment. Total correlation spectroscopy (TOCSY) visualizes couplings between all protons in a spin system. These techniques can be beneficial for structural analysis.

Of course NMR spectroscopy can monitor other nuclei apart from protons as well. One dimensional ^{31}P NMR can provide information about phosphorous-containing molecules used during the synthesis. Trioctylphosphine or trioctylphosphine oxide are commonly used in various syntheses for example. Heteronuclear single-quantum correlation (HSQC) can be used to determine the presence of couplings between two different types of nuclei which are separated by a single bond. A heteronuclear multiple-bond correlation (HMBC) on the other hand determines the couplings between two different types of nuclei separated by more bonds as well. All mentioned techniques can be used for structural analysis. Hence, ligands can be identified, the synthesis yield conversion can be monitored or reactions taking place at the nanocrystal surface can be discovered.

References

[1] Timothy D.W. Claridge. *High-Resolution NMR Techniques in Organic Chemistry, 2nd edition.* Elsevier, 2008.

[2] Serge Akoka, Laurent Barantin, and Michel Trierweiler. *Concentration measurement by proton NMR using the ERETIC method.* Analytical Chemistry, 71(13):2554–2557, 1999.

[3] Peter Stilbs. *Fourier Transform Pulsed-Gradient Spin-Echo Studies of Molecular Diffusion.* Progress in Nuclear Magnetic Resonance Spectroscopy, 19(1):1–45, 1987.

[4] EO Stejskal and JE Tanner. *Spin Diffusion Measurements: Spin Echo in the Prescence of a Time-Dependent Field Gradient.* Journal of Chemical Physics, 42(1):288, 1965.

[5] Zeger Hens, Iwan Moreels, and José C. Martins. *In situ ^{1}H NMR study on the triOctylphosphine oxide capping of colloidal InP nanocrystals.* Chemphyschem, 6(12):2578–2584, 2005.

[6] Moerner W.E. *Persistent Spectral Hole-Burning: Science and Applications.* Springer-Verlag, 1998.

3

Aminophosphines: a Double Role in the Synthesis of Colloidal Indium Phosphide Quantum Dots[1]

Aminophosphines have recently emerged as economical, easy-to-implement precursors for making InP nanocrystals, which stand out as alternative, Cd-free quantum dots for opto-electronic applications. In this chapter, a complete investigation of the chemical reactions leading to InP formation starting from $InCl_3$ and tris(dialkylamino)phosphines, is presented. NMR, MS and single crystal X-ray diffraction are used to demonstrate that the aminophosphine is both precursor and reducing agent.

[1] *Adapted from:* Mickael D. Tessier, Kim De Nolf, Dorian Dupont, Davy Sinnaeve, Jonathan De Roo, Zeger Hens. *Aminophosphines: a Double Role in the Synthesis of Colloidal Indium Phosphide Quantum Dots*, Journal of the American Chemical Society, 138 (18), 5923-5929, 2016

3.1 Introduction

Colloidal nanocrystals have many applications[1] ranging from energy[2–4] to opto-electronics[5–7] and catalysis.[8] In particular, quantum dots (QDs) fluorescing in the visible range are of significant interest for lighting and display applications.[9–12] In this respect, stringent restrictions on the use of cadmium in consumer products have initiated a shift from the well-characterized Cd-based QDs to Cd-free alternatives such as indium phosphide. The first synthesis of InP nanocrystals with a reasonable size dispersion was reported in 1995.[13] This synthesis employed tris(trimethylsilyl) phosphine (PTMS) which remains as yet the most widely used phosphorus precursor for the synthesis of InP QDs. However, this compound is in many respects problematic as it is highly expensive and autoignites in contact with air. Recently, efficient protocols based on aminophosphines have been established to synthesize InP QDs of different sizes.[14;15] As compared to PTMS, aminophosphines are inexpensive precursors that are safe-to-use under ambient conditions and proved to lead to InP QDs of comparable quality as the best samples obtained with PTMS.[16;17] In addition, aminophosphine-based syntheses can lead to InP/ZnE (E = S or Se) core/shell QDs that emit from 500 nm to 670 nm with an emission linewidth between 44 nm and 65 nm and a photoluminescence quantum yield of 20 to 80 %.[14]

Since the early days of Cd-based QD syntheses, insights in the reaction mechanism were used to improve the synthetic result in terms of size control and minimization of size dispersion.[18] By now, several QD synthesis methods have been shown to follow a two-step process where the injected precursors first react to form the solute or monomer whose increasing concentration subsequently gives rise to nucleation and growth of nanocrystals.[19–21] In this respect, mechanistic studies have addressed both the chemical reactions involved in monomer formation and the relation between the monomer formation rate and the size of the resulting nanocrystals.[22–25] Especially in the case of CdSe QDs synthesized using trioctylphosphine selenium (TOPSe), precursor conversion was investigated in great detail and found to consist of two essential steps, *i.e.*, a coordination of TOPSe to the Cd center, followed by the cleavage of the Se=P bond. Moreover, this precursor conversion was found to be limiting the overall rate of CdSe formation.[25] This finding not only resulted in several size tuning strategies,[22–24] it also indicates that a controlled synthesis of nanocrystals will only be possible if the precursor conversion is slow as compared to the nucleation and growth of the nanocrystals proper. Such a size tuning strategy is thoroughly discussed in Chapter 4 of this manuscript.

Importantly, such studies are shifting synthesis development from a semi--empirical trial-and-error approach to a more rational design of synthesis protocols that allows for optimal control of the QD size and size dispersion. A recent and most striking example involves the formation of lead sulfide QDs from thiourea precursors where insight in the relation between reaction rate and nanocrystal size was implemented to achieve size control at full reaction yield over a broad range of nanocrystal diameters.[26] In the case of PTMS-based synthesis protocols for InP QDs, different mechanistic studies showed that precursor conversion is complete upon injection,[27;28] resulting in ripening-driven nanocrystal growth. Although this was linked to the difficulty of synthesizing monodisperse InP QDs, the use of substituted silylphosphines with a lower reactivity did not overcome this problem.[29] In the case of aminophosphine precursors on the other hand, the InP formation rate proved to be much slower.[14] Whereas this lower rate was utilized to implement economical size-tuning-at-full-yield strategies, the chemistry of the conversion reaction is not yet understood. This, however, is crucial to further optimize the reaction and extend it to the synthesis of other metal phosphide and metal arsenide nanocrystals.

In this chapter, several key aspects that govern the formation of InP from aminophosphine precursors and indium chloride in the presence of primary amines are identified. First, it is shown that the reaction involves the substitution of the original amino groups by amines present in the reaction mixture, where only transamination with primary amines leads to InP formation. Furthermore, it was found that the substituted aminophosphine has a double role in the reaction, both serving as the phosphorous precursor and the reducing agent by the formation of P^{V} phosphonium salt. These findings are summarized in a chemical reaction mechanism that may help using this unique precursor chemistry for the formation of, *e.g.*, GaP, InAs or GaAs nancrystals. These have proven even more challenging than InP to synthesize as nanocrystals, with synthesis methods suffering from poor size dispersions[13] or requiring extremely hazardous precursors.[30;31]

3.2 Experimental

Chemicals Indium(III) chloride (99.999 %), zinc(II) chloride ($\geq$ 98%), dodecylamine (99 %), tris(diethylamino)phosphine (97 %), tris(dimethylamino)phosphine (97 %), selenium powder 100 mesh (99.99 %) and zinc stearate (technical grade, 65 %) were purchased from Sigma Aldrich. Trioctylphosphine ($>$ 97%) were purchased from Strem Chemicals. Oleylamine (80-90 %) was purchased from Acros Organics (NB: Oleylamine is stored

under inert atmosphere). Octadecene (technical 90 %) was purchased from Alfa Aesar.

Synthesis of core/shell InP/ZnSe QDs 100 mg (0.45 mmol) of indium(III)chloride and 300 mg (2.2 mmol) of zinc(II) chloride are mixed in 5.0 mL (15 mmol) of technical oleylamine which is a coordinating solvent. The reaction mixture is stirred and degassed at 120°C for an hour and subsequently heated to 180°C under inert atmosphere. Upon reaching 180°C, a volume of 0.45 mL (1.6 mmol) of tris(diethylamino)phosphine is quickly injected in the above mixture. After the phosphorus precursor injection, InP nanocrystals are formed. The InP core QDs reaction occurs during 30 minutes. Thereafter, the shell growth procedure is started by the slow injection of 1 mL of stoichiometric TOPSe (2.2 M). At 60 minutes, the temperature is increased from 180°C to 200°C. One hour later, at 120 minutes, 1 g of $Zn(stearate)_2$ in 4 mL of octadecene is slowly injected. Subsequently, the temperature is increased again from 200°C to 220°C. After 150 minutes of reaction, 0.7 mL of stoichiometric TOPSe (2.2 M) is injected. The temperature is increased from 220°C to 240°C. At 180 minutes, 1 g of $Zn(stearate)_2$ in 4 mL of octadecene is injected followed by a temperature increase from 240°C to 280°C. At 210 minutes, 0.7 mL of stoichiometric TOPSe (2.2 M) is injected slowly for the third time. Temperature is increased from 280°C to 320°C. After 240 minutes, the last slow injection of 1 g of $Zn(stearate)_2$ in 4 mL of octadecene is performed. Finally, the end of the reaction is reached after 300 minutes by cooling down. InP/ZnSe nanocrystals are then precipitated with ethanol and redispersed in chloroform.

Mass spectrometry InP core QDs are synthesized and precipitated with methanol. The supernatant is analyzed using a 6230 TOF-MS with ESI-source mass spectrometer of Agilent Technologies in a range from 55 to 1160 $g.mole^{-1}$.

NMR spectroscopy Aliquots of $40 - 100\mu L$ are taken from a synthesis and put into vials containing inert atmosphere (Argon). It is crucial to prevent contact between aliquots and air. Oxidation of the aminophosphine species into aminophosphine oxide species leads to the appearance of extra resonances in the NMR spectra that complicate the interpretation. A fixed volume of the aliquots is dissolved in $500\mu L$ toluene-d8 (99,50 % D, purchased at Euriso-top) and transferred to an NMR tube (5 mm). NMR measurements were recorded on a Bruker Avance III Spectrometer operating at a ^1H frequency of 500.13 MHz and equipped with a BBI-Z probe or on a Bruker Avance II Spectrometer operating at a ^1H frequency of

500.13 MHz and equipped with a TXI-Z probe (channels are ^{1}H, ^{13}C, ^{31}P). The sample temperature was set to 298.15 K. Quantitative ^{1}H spectra were recorded with a 20 s delay between scans to allow full relaxation of all NMR signals. The quantification was done by using the Digital ERETIC method. ^{31}P spectra were recorded with a 20 s delay between scans to allow full relaxation of all NMR signals as well. Diffusion measurements (2D ^{31}P DOSY) were performed using a double stimulated echo sequence for convection compensation and with monopolar gradient pulses.[32] Smoothed rectangle gradient pulse shapes were used throughout.

Single crystal X-ray diffraction X-ray intensity data were collected on a Agilent Supernova Dual Source (Cu at zero) diffractometer equipped with an Atlas CCD detector using CuKα radiation ($\lambda = 1.54184$ Å) and ω scans. The images were interpreted and integrated with the program CrysAlisPro (Agilent Technologies, Agilent (2013). CrysAlis PRO. Agilent Technologies UK Ltd, Yarnton, England.). Using Olex2[33], the structures were solved by direct methods using the ShelXS structure solution program and refined by full-matrix least-squares on F2 using the ShelXL program package[34]. Non-hydrogen atoms were anisotropically refined and the hydrogen atoms in the riding mode and isotropic temperature factors fixed at 1.2 times U(eq) of the parent atoms (1.5 times U(eq) for methyl groups).

Crystal data for $[C_2H_6NH_2Cl]$: M = 81.54, orthorhombic, space group Ibam (No. 72), a = 7.2377(5) Å, b = 14.3892(11) Å, c = 9.8897(9) Å, V = 1029.96(14) Å3, Z = 8, T = 100 K, ρ_{calc} = 1.052 g cm^{-3}, $\hat{I}\frac{1}{4}$(Cu-Kα) = 0.564 mm^{-1}, F(000) = 352.0, 2992 reflections measured, 558 unique (Rint = 0.0545) which were used in all calculations. The final R1 was 0.0320 (I > 2σ (I)) and wR2 was 0.0676 (all data). The structure of $[C_2H_6NH_2Cl]$, has been previously determined and deposited with the Cambridge Structural Database (CSD, Version 5.37, 2016)[35], with CCDC-numbers 204844, 661061 and 721889.[36;37]

3.3 Results and discussion

3.3.1 InP quantum dot synthesis

In a typical aminophosphine-based synthesis of InP QDs, indium halides and zinc halides are dissolved in a primary amine as solvent (*e.g.*, oleylamine ($OlNH_2$), where Ol = $C_{18}H_{35}$).[14;15] The reaction mixture is subsequently degassed and heated to 150 − 220°C, followed by the injection of tris(dimethylamino)phosphine, $P(NMe_2)_3$, or tris(diethylamino)phosphine,

$P(NEt_2)_3$. Figure 3.1a depicts the UV-Vis absorption spectra of different aliquots taken at various reaction times for the case of an InP QD synthesis at 180°C (see Experimental Section for details). Already after 1 min of reaction, the first excitonic feature is clearly visible and its redshift with time points towards an increase of the QD diameter during the reaction. When the QDs reach their optimal size, shell precursors are added to the reaction mixture to obtain core/shell InP/ZnE (E = S, Se) QDs. In Figure 3.1a, the absorbance and photoluminescence spectra of InP/ZnSe QDs are shown. They have been obtained using stoichiometric trioctylphosphine selenium and zinc stearate mixed in octadecene as shell precursors (see Experimental Section for details). This sample exhibits a photoluminescence full width at half maximum of 47 nm and a photoluminescence quantum yield of 50 % which are excellent values in comparison to the best core/shell InP/ZnE QDs obtained with PTMS precursor.[16;17] Different size-tuning strategies, such as stopping the reaction before its end[15] or using different indium halide or zinc halide precursors,[14] allow obtaining InP/ZnE QDs over the entire visible range as shown in Figure 3.1b.

Although aminophosphines prove most useful precursors for synthesizing InP QDs, they are not the most obvious. In PTMS, the phosphorus atom has an oxidation state of -III, rendering a reaction with an In^{III} precursor such as indium chloride or indium acetate most likely. Aminophosphines on the other hand are P^{III} compounds, such that intermediate reduction steps are needed to form InP in a reaction with an In^{III} precursor. Two-step methods in which at least the indium precursor is reduced before reacting with the phosphorus precursor have already been described in the literature. $InCl_3$ for example can be reduced by KBH_4 to form In^0 which then reacts with white phosphorus (P_4).[38] Another example is the reduction of $InCl_3$ by an organolithium reagent, followed by the reaction of the resulting In^0 with trioctylphosphine by a catalytic cleavage at high temperature.[39] Opposite from aminophosphine-based syntheses, however, such two-step strategies lead to rather polydisperse InP QDs. Alternatively, Song *et al.*. hypothesized that InP formation starting from aminophosphine could involve the *in-situ* formation of phosphine (PH_3) due to the presence of labile hydrogens in the primary amine solvent.[15] However, amines being poor Brønsted acids, such a mechanism seems unlikely.

3.3.2 Transamination reaction

To investigate possible intermediate reaction steps involved in the formation of InP out of aminophosphine and $InCl_3$, the exhaust of an InP QD synthesis was scrubbed using a chemical gas trap (Figure 3.2a). Most notably,

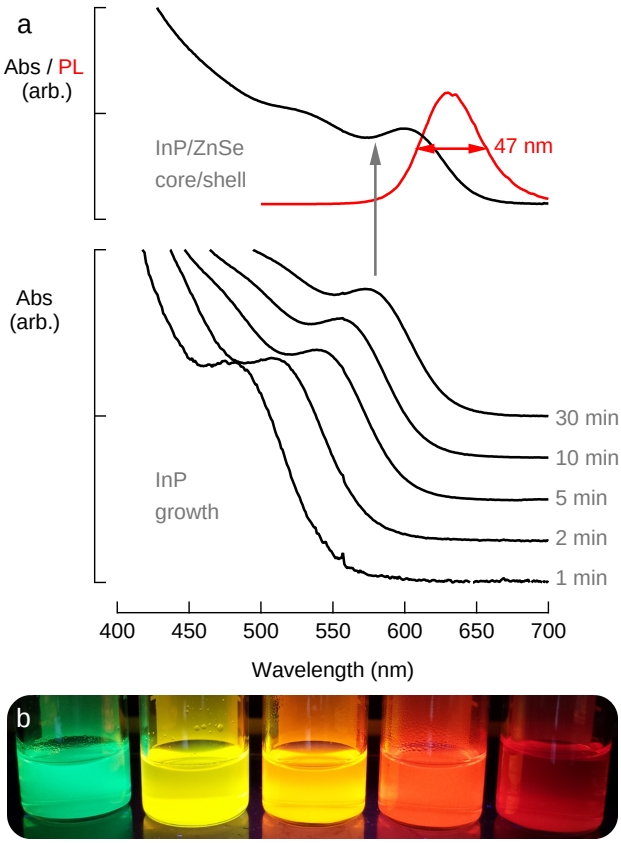

Figure 3.1: (a) (bottom) Development of the absorption spectrum of InP QDs during a typical aminophosphine-based synthesis of InP QDs and (top) absorption and photoluminescence spectra of resulting InP/ZnSe QDs. (b) Picture of a series of different InP/ZnE QDs emitting from 500 nm to 670 nm.

the formation of a copper hydroxide precipitate was observed upon scrubbing with a saturated aqueous $CuSO_4$ solution, a strong indication that the exhaust contains a basic gas (Figure 3.2b). Scrubbing with a methanolic solution of hydrogen chloride enabled us to trap the base as a salt. After rotary evaporation, a solid residue was obtained and after recrystallization in ethyl acetate, this salt was identified by single crystal X-ray diffraction as dimethylammonium chloride for a reaction where $P(NMe_2)_3$ was used as the phosphorus precursor (see Experimental Section for details). This points towards an exchange between the amines used as a solvent in the

synthesis and the amino groups coordinating to phosphorus in the original precursor. This exchange is also observed using $P(NEt_2)_3$ as the phosphorus precursor.

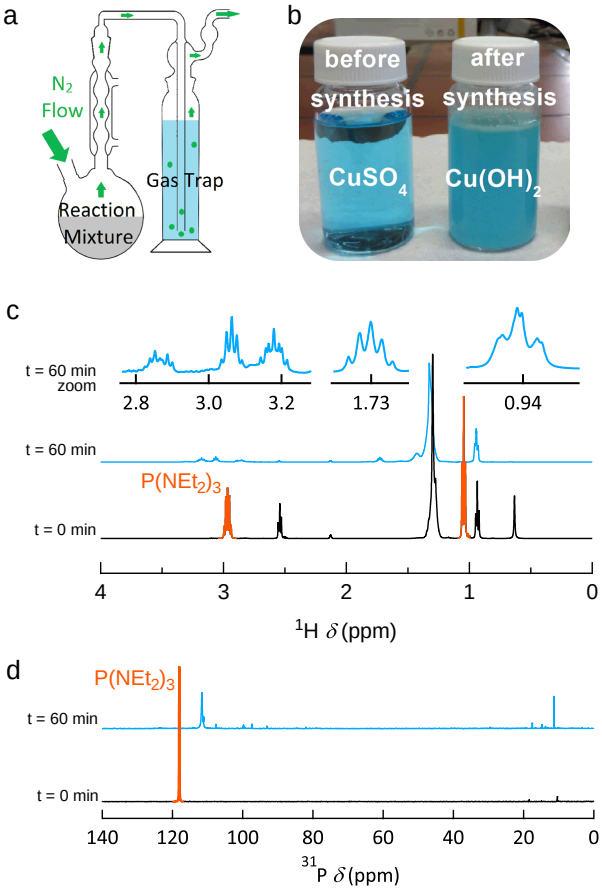

Figure 3.2: a) Scheme of the gas trap mounting. b) Picture of the $CuSO_4$ gas trap aqueous solution before and after an InP synthesis. c) ^{1}H NMR spectrum of $P(NEt_2)_3$ and dodecylamine, prior to and after reaction at 120°C for 60 minutes. d) ^{31}P NMR spectra of aliquots taken during the reaction of $P(NEt_2)_3$ and dodecylamine.

Simply mixing $P(NEt_2)_3$ and dodecylamine (ratio 1:3) in a vial under an inert atmosphere confirms this transamination. Indeed, when the temperature is raised above 100°C, gas bubbles evolve, which we attribute to Et_2NH rather than $P(NEt_2)_3$, as the latter has a boiling point of 245°C. This is

further corroborated by the two ^{31}P NMR spectra shown in Figure 3.2d, recorded on a mixture of $P(NEt_2)_3$ and dodecylamine prior to and 1 h after reaction. The initial solution features a single resonance of $P(NEt_2)_3$ at 118 ppm. This has almost completely vanished after 1 h of reaction due to transamination. Diethylamine is formed and has evaporated from the mixture (boiling point = 55°C). Moreover, a new, somewhat shifted dominant resonance appears at 111 ppm, most likely a transaminated aminophosphine, next to several less intense resonances especially at around 11 ppm.

Denoting the alkyl moiety of the solvent in general as R, this transamination can be written as a sequence of three successive reactions for the tris(diethylamino)phosphine precursor:

$$P(NEt_2)_3 + RNH_2 \rightleftharpoons P(NEt_2)_2(NHR) + Et_2NH \tag{3.1}$$

$$P(NEt_2)_2(NHR) + RNH_2 \rightleftharpoons P(NEt_2)(NHR)_2 + Et_2NH \tag{3.2}$$

$$P(NEt_2)(NHR)_2 + RNH_2 \rightleftharpoons P(NHR)_3 + Et_2NH \tag{3.3}$$

The ^{1}H NMR spectra prior to and after transamination presented in Figure 3.2c show again that the CH_3 and CH_2 resonances of $P(NEt_2)_3$ at 1.04 and 2.97 ppm disappear. In the region of the latter, three new resonances appear at 3.18, 3.07, and 2.86 ppm next to a fourth pentet resonance at around 1.73 ppm. These resonances come in an approximately 2:2:1:2 ratio. Such a ratio can be expected for the resonances of the two $\alpha-CH_2$, the N-H protons, and the $\beta-CH_2$ in the alkyl chain of a twice transaminated compound $P(NEt_2)(NHR)_2$. Note that the CH_3 of the remaining NEt_2 group is shifted and almost overlaps with the CH_3 of the alkyl chain at around 0.95 ppm.

A more detailed NMR analysis is performed on a different sample, where oleylamine is mixed with tris(diethylamino)phosphine in a 1:9 ratio. Next to one dimensional ^{1}H and ^{31}P spectra, a ^{1}H-^{31}P HMBC and a ^{1}H-^{13}C HSQC were recorded. Figure 3.3 shows that the transamination has lead to three dominant resonances in the ^{31}P NMR spectrum: the resonance at 111 ppm (P1), which was examined in Figure 3.2, a resonance at 98 ppm (P2) and a resonance at 10 ppm (P3). The ^{1}H-^{31}P HMBC spectrum (Figure 3.4) measures the proton-phosphorous couplings. P1 has a coupling with three proton signals at 3.18, 3.07, and 2.86 ppm, with again an intensity ratio of 2:2:1, respectively. The proton at 2.86 ppm has no signal in the HSQC spectrum (Figure 3.5), which means that this proton is most likely the N-H proton of an oleylamino group. The protons at 3.18 and 3.07 ppm have a clearly different multiplicity. These results can be expected

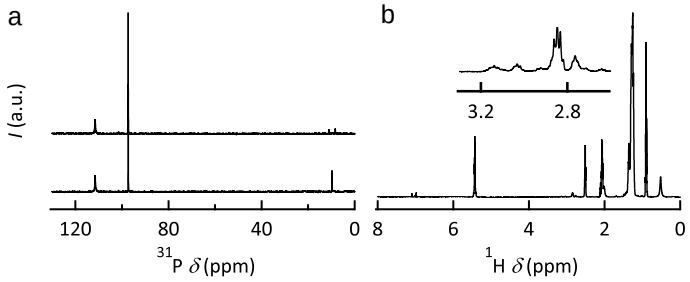

Figure 3.3: a) ^{31}P NMR spectra without (top) and with (bottom) ^{1}H-^{31}P decoupling of $P(NEt_2)_3$ and oleylamine after reaction at $120^{\circ}C$ for 60 minutes. b) ^{1}H NMR spectrum of the same mixture.

for the resonances of the two $\alpha-CH_2$ and the N-H protons of the twice transaminated compound $P(NEt_2)(NHR)_2$.

P2 couples with two protons at 2.85 and 1.47 ppm in the ^{1}H-^{31}P HMBC spectrum. The proton at 1.47 ppm is most likely an N-H proton since it has no signal in the HSQC spectrum. Therefore, we can assign P2 to a transaminated aminophosphine compound with at least one oleylamino group.

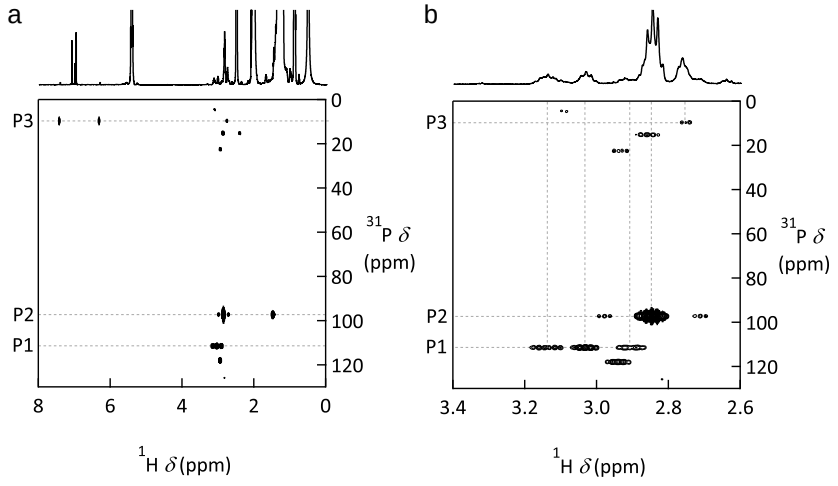

Figure 3.4: a) ^{1}H-^{31}P HMBC spectrum of $P(NEt_2)_3$ and oleylamine after reaction at $120^{\circ}C$ for 60 minutes. b) Detail of the ^{1}H-^{31}P HMBC spectrum shown in (a). P1, P2 and P3 are indicated in the figure.

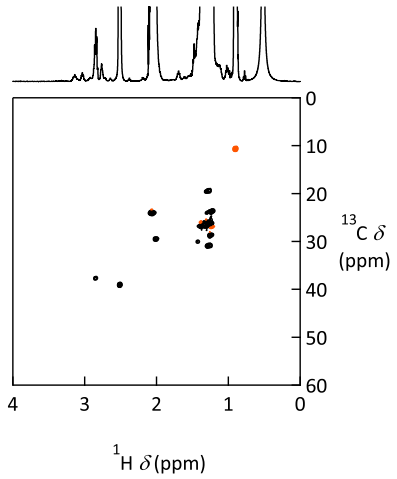

Figure 3.5: Isotope*1,H-^{31}P HSQC spectrum of $P(NEt_2)_3$ and oleylamine after reaction at 120°C for 60 minutes.

A ^{31}P NMR spectrum without ^{1}H-^{31}P decoupling shows that P3 exhibits a fairly large J_{PH} coupling of 556 Hz with the corresponding protons appearing at 7.42 and 6.31 ppm (See the ^{1}H-^{31}P HMBC in Figure 3.4). A J_{PH} coupling can only be this large if the proton is located directly onto the phosphorus atom. Such a P-H bond is typical for an iminophosphorane, which is a tautomeric form of aminophosphines that have a primary amino group (see Figure 3.6).[40] We therefore attribute P3 to a tautomer of one or more transaminated aminophosphines, yet the degree of transamination of this compound is not confirmed.

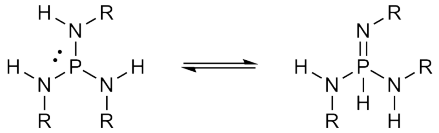

Figure 3.6: There is a tautomeric equilibrium between aminophosphines (left) and iminophosphoranes (right).

Transamination reactions for $P(NMe_2)_3$ and $P(NEt_2)_3$ have been described before.[41;42] Burgada for example argues that an exchange between the dimethylamino group of $P(NMe_2)_3$ and a heavier second amino group can occur if the hydrogen of this second amino group is sufficiently labile.[41] As the boiling point of dimethylamine is 7.4°C, this compound is eliminated

Table 3.1: Reaction results as a function of the solvent used

Kind of amine	Name	Outcome
Primary amines	Butylamine	InP QDs
	Octylamine	
	Dodecylamine	
	Oleylamine	
Secundary amines	Dioctylamine	No reaction
Tertiary amines	Trioctylamine	
Other solvent	tri-*n*-octylphosphine	

from the reaction mixture after its formation, shifting the equilibrium of the reaction to the formation of a fully transaminated aminophosphine where the amino group has a higher boiling point than dimethylamine. Even if the author mentioned exchange between secondary amines only, it underlines our observation that a similar exchange involving a primary amine, such as dodecylamine or oleylamine, and a more volatile amino group, such as dimethylamino or diethylamino, occurs in the aminophosphine-based synthesis of InP.

The occurrence of transamination provides an important perspective on the role of the amino group in a particular aminophosphine precursor. First of all, it implies that adjusting this group to tune the precursor reactivity and thus the outcome of an InP synthesis risks to be an inefficient strategy if - as seems necessary - high boiling point amines are used as the solvent for the reaction. Indeed, in that case it will be the solvent that dictates what amino groups make up the true aminophosphine precursor. This explains for one thing why we do not observe significant differences in reactivity between, *e.g.*, $P(NMe_2)_3$ and $P(NEt_2)_3$. On the other hand, the amino exchange highlights the role of the primary amine used as the solvent. By screening several amines, we find that InP is only formed when a primary amine is used. No reaction takes place in the case of secondary or tertiary amines (see Table 3.1). This clearly indicates that primary amines are not just the solvent or the ligand in an aminophosphine-based InP synthesis. Rather, they must play a central role in the whole precursor chemistry.

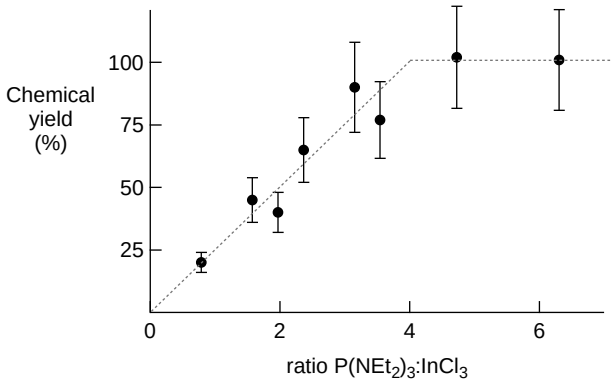

Figure 3.7: Yield conversion - amount of InP formed as fraction of the amount of $InCl_3$ used - of a tris(diethylamino)phosphine-based InP QDs synthesis plotted as a function of the $P(NEt_2)_3$:$InCl_3$ ratio used in the synthesis. The trend line is a straight line through the origin reaching full yield at a $P(NEt_2)_3$:$InCl_3$ ratio of 4, followed by a horizontal at 100% for higher $P(NEt_2)_3P$:$InCl_3$ ratios.

3.3.3 Reaction yield development

Focusing on syntheses using $P(NEt_2)_3$ and $InCl_3$ in oleylamine, a key point to get further insight in the precursor conversion is the observation we already made before that the conversion yield of the indium precursor into InP, *i.e.*, the chemical yield, depends on the aminophosphine *vs.* indium halide equivalence.[14] Here, the chemical yield is calculated by comparing the absorbance of quantitative aliquots with the intrinsic absorption coefficient of InP QDs at the same short wavelength.[14] As shown in Figure 3.7, we find that the chemical yield increases proportionally to the $P(NEt_2)_3$:InX_3 molar ratio to reach 100% for ratios of ≈ 4 or more. At this point, we hypothesize that a phosphorus precursor excess is needed to obtain full chemical yield because the aminophosphine plays more than one role in the synthesis. As discussed before, formation of an InP unit from $P(NEt_2)_3$ comes with a reduction of P^{III} to P^{-III}. One way to achieve this - and that accounts for the observed phosphorous excess needed to reach full conversion of the indium - is that one equivalent of phosphorous is reduced to P^{-III} by the oxidation of 3 equivalents of phosphorous to P^{V}. We have already demonstrated that injected $P(NEt_2)_3$ is modified during the synthesis by transamination. To continue this line of thought, we therefore propose an overall redox reaction in which 1 equivalent of InP is formed by the oxidation of 3 equivalents of

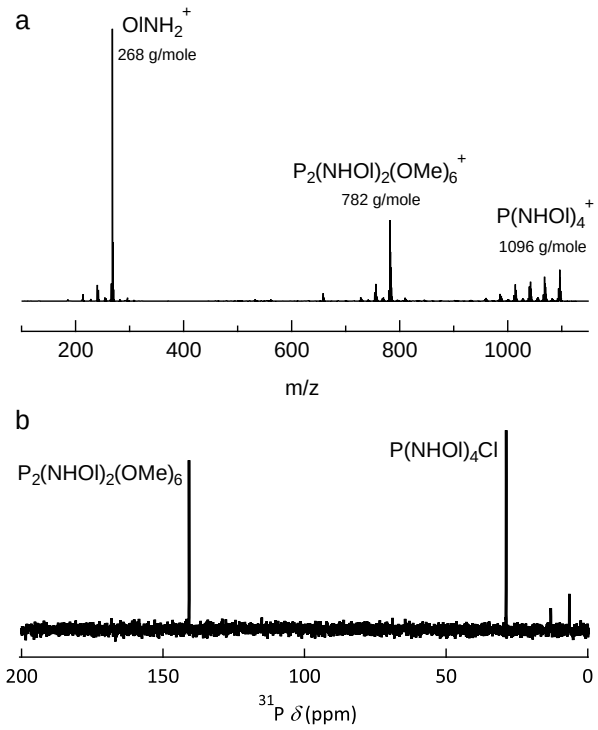

Figure 3.8: a) Mass-spectrum of the supernatant obtained after purification by methanol addition of a full yield diethylaminophosphine-based InP QDs synthesis b) ^{31}P NMR spectrum of the supernatant used for mass spectrometry diluted using toluene-d8.

the substituted aminophosphine to a phosphonium salt:

$$\mathrm{InX_3} + 4\,\mathrm{P(NHR)_3} \rightleftharpoons \mathrm{InP} + 3\,\mathrm{P(NHR)_4X} \tag{3.4}$$

In this chemical equation, R represents an alkyl moiety of a primary amine and X is either Cl, Br or I.

First evidence that Equation 3.4 indeed describes the overall reaction leading to InP comes from the mass spectrum of the reaction mixture after removal of the InP QDs by methanol addition. As shown in Figure 3.8 a, it contains three main compounds. A first has a molar mass of 268 g/mole, most likely corresponding to oleylamine, which is the solvent of the reaction and thus present in large amounts. The second compound has a molar mass of 782 g/mole, which corresponds to $\mathrm{P_2(NHOl)_2(OMe)_6}$. Prob-

ably, this has been produced during the purification in a reaction between aminophosphine compounds and methanol (see Experimental Section). The third compound has a measured molar mass of 1096 g/mol which is close to the 1097 g/mol expected for $P(NHOl)_4^+$, *i.e.*, the oleylamino phosphonium cation generated by the reaction according to Equation 3.4.

3.3.4 ^{31}P NMR spectroscopy analysis of the reaction development

To investigate in more detail this InP QD synthesis, we analyzed the reaction development using ^{31}P NMR spectroscopy. In Figure 3.9a, the ^{31}P NMR spectra of the precursor mixture and reaction aliquots are shown. Five resonances can be distinguished. Next to the initial precursor at 118 ppm (P0), two more resonances appear at comparable chemical shifts of 111 (P1) and 98 (P2) ppm. Like in the case of transamination with dodecylamine or oleylamine, we again attribute P1 to the twice transaminated compound $P(NEt_2)(NHOl)_2$. Also P2 was identified as a transamination product. As it always appears faster than P1 in a blank transamination reaction or during InP synthesis, we tentatively attribute this to the once transaminated compound $P(NEt_2)_2(NHOl)_1$. The resonance at 13 ppm (P3) was attributed earlier to a tautomer of one or more transaminated aminophosphines. Finally, we already identified the 29 ppm (P4) resonance as the phosphonium salt (see Figure 3.8b). Note that the assignment of P0, P1, P2, and P4 concurs with the variation of the diffusion coefficient of the corresponding compounds, which gets smaller for the more bulky species (see Figure 3.9a).

By identifying P1 and P2 as transaminated species and P4 as the main reaction byproduct, the development of these different phosphorus species can be monitored during a reaction by analyzing successive aliquots (see Figure 3.9b). Here, we derived the concentration of each species from the integrated intensity of its ^{31}P resonance. By taking a reaction carried out at 190°C as an example, Figure 3.9a and 3.9b show that 15 s after injection P0 has disappeared and the transaminated compounds are already the prevailing species. Next, Figure 3.9b shows that, during the reaction, the concentration of $P(NHOl)_4Cl$ gradually increases at a rate concurring with the formation of InP with an estimated equivalence somewhat exceeding 3:1. Clearly, this observation confirms the overall chemical reaction equation 3.4, where indeed one InP equivalent is formed together with 3 equivalents of $P(NHOl)_4Cl$ and it agrees with the MS analysis showing $P(NHOl)_4Cl$ to be the dominant reaction byproduct. The decrease in concentration of both transaminated aminophosphines follows the formation of InP, confirming

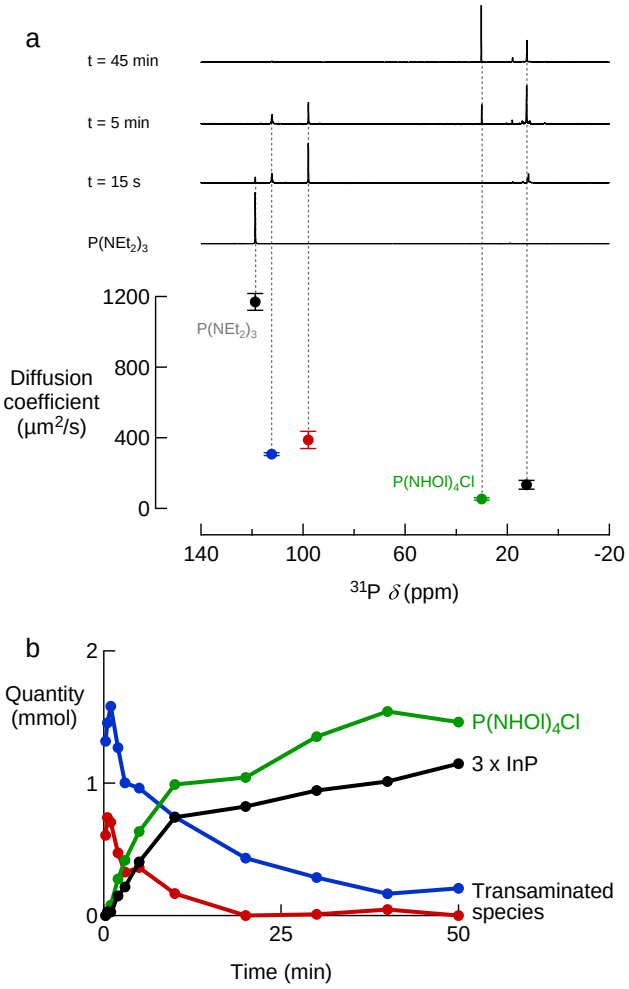

Figure 3.9: (a) (top) ^{31}P NMR spectra of $P(NEt_2)_3$ and different aliquots taken at the indicated time after initiating a diethylaminophosphine based InP synthesis run at $170^{\circ}C$, related to (bottom) the diffusion coefficient of the resonances as determined using ^{31}P DOSY. (B) (colored) Concentration development of the prevailing species during a diethylaminophosphine based InP synthesis run at $170^{\circ}C$ as estimated from ^{31}P NMR resonance intensities and (black) the concomitant amount of InP formed.

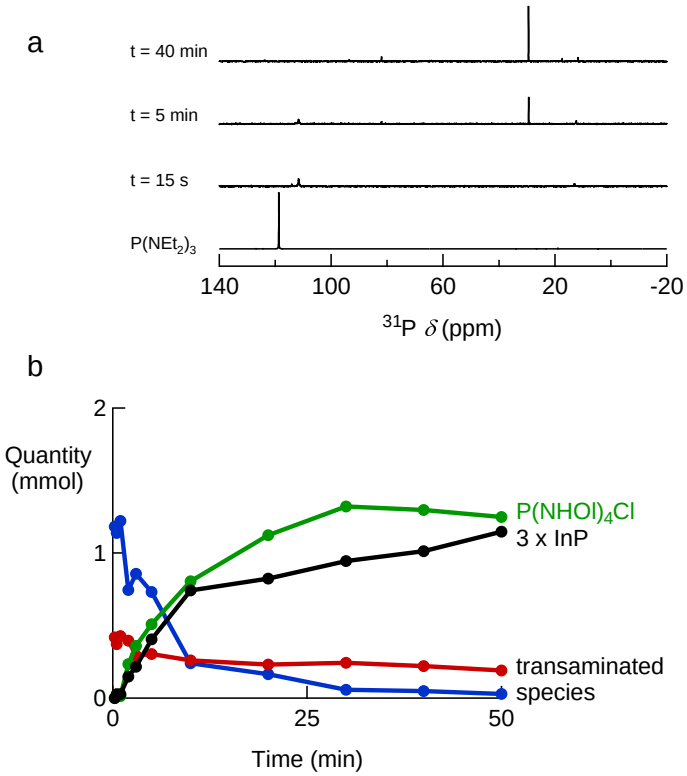

Figure 3.10: (a) ^{31}P NMR spectra of $P(NEt_2)_3$ and different aliquots taken at the indicated time after initiating a diethylaminophosphine based InP synthesis run at 170°C with $ZnCl_2$ present. (B) (colored) Concentration development of the prevailing species during a diethylaminophosphine based InP synthesis run at 170°C with $ZnCl_2$ present as estimated from ^{31}P NMR resonance intensities and (black) the concomitant amount of InP formed.

their role as the actual phosphorus precursor in this reaction. More specifically, the absence of partially substituted phosphonium salts suggests that the actual precursor is most likely $P(NHOl)_3$, the fully transaminated compound. Note that the concentration of the tautomeric form, on the other hand, stays largely constant during the reaction, suggesting that this P^V compound is unreactive and only formed in the initial stage of the reaction.

For the InP/ZnSe core/shell synthesis, 2.2 mmol $ZnCl_2$ is added from the start of the reaction. Figure 3.10 shows that the presence of $ZnCl_2$ con-

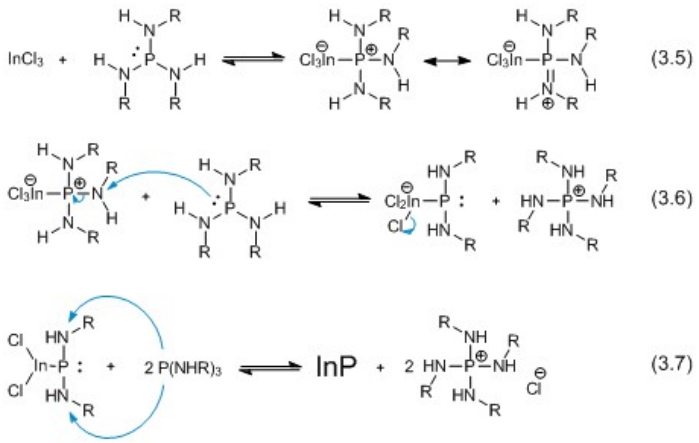

Figure 3.11: Proposed reaction mechanism, shown in three steps: reaction 3.5, 3.6 and 3.7

siderably speeds up the transamination. Indeed, $P(NEt_2)_2(NHOl)_1$ already has disappeared after 15 seconds, while this compound is still present after 5 minutes in the reaction without $ZnCl_2$ (Figure 3.9a). Nevertheless, the concentration of $P(NHOl)_4Cl$ still gradually increases at a rate concurring with the formation of InP with an approximately 3:1 equivalence and the decrease in concentration of the twofold substituted $P(NEt_2)_1(NHOl)_2$ still reflects the InP formation.

3.3.5 Reaction mechanism

Based on the overall InP formation reaction expressed by Equation 3.4, a chemical reaction mechanism can be proposed. In accordance with the double role of phosphorus, this mechanism assumes a nucleophilic attack by the phosphorus center of one aminophosphine on an amino group of another aminophosphine. Considering that the fully transaminated $P(NHR)_3$ is the actual reactant, reaction 3.5-3.7, Figure 3.11 represent the different steps this conversion involves. In a first step (reaction 3.5), an adduct of $InCl_3$ and $P(NHR)_3$ is formed. Importantly, such a complex exhibits different resonance structures (only two of which are shown), which lead to a delocalization of the positive charge over the phosphorus center and the surrounding nitrogen atoms. This renders the nitrogen atoms sensitive to a nucleophilic attack by a second $P(NHR)_3$ as represented in reaction 3.6. This results in the formation of an InP intermediate and a first equivalent of the $P(NHR)_4Cl$ phosphonium salt. Note that this reaction leads to a

first change in the phosphorus oxidation numbers, with that in the InP intermediate being reduced from +III to +I and that in the phosphonium salt being oxidized from +III to +V. Reaction 3.7 sketches subsequent reduction steps, where two more equivalents of $P(NHR)_3$ further reduce the phosphorus in the InP intermediates to an oxidation state of -I and -III, respectively, and result in the formation of 1 equivalent of InP. The proposed pathway provides an explanation as to why InP is only formed when using primary amines as the solvent. Indeed, steric hindrance may hamper both the formation of the adduct depicted in reaction 3.5 and the subsequent nucleophilic attack on nitrogen. Moreover, an alkyl chain is an electron-donating group that can further stabilize the positive charge in the adduct. This may render the nitrogen atoms less electrophilic, a necessary attribute for the subsequent reactions.

3.4 Conclusion

In summary, we have studied the precursor conversion in the aminophosphine-based synthesis of InP QDs. We have shown that upon injection, dimethyl- and diethylaminophosphine undergo rapid transamination with the amine used as the solvent. This leads to the release of dimethyl or diethylamine and an effective aminophosphine precursor that is most likely the fully transaminated compound. Only in the case that primary amines are used, this leads to the eventual formation of InP, where a quaternary aminophosphonium salt is formed as the major reaction byproduct. This finding enables the overall InP formation reaction to be written as a redox reaction where three equivalents of the transaminated aminophosphine reduce a fourth equivalent to form one equivalent of InP. Importantly, this double role of the aminophosphine explains why full conversion of the In precursor into InP is only attained with a 4-fold excess of the aminophosphine. This picture is confirmed by monitoring the reaction development using ^{31}P NMR spectroscopy. Based on these findings, we propose a chemical reaction mechanism that involves a nucleophilic attack of one aminophosphine on the nitrogen in a second aminophosphine that is activated by complexation with $InCl_3$. We believe that the new chemistry introduced here for the formation of InP QDs may be extended to the formation of other III-V quantum dots, such as GaP, InAs or GaAs, using similar aminophosphine or aminoarsine precursors.

References

[1] Maksym V. Kovalenko, Liberato Manna, Andreu Cabot, Zeger Hens, Dmitri V. Talapin, Cherie R. Kagan, Victor I. Klimov, Andrey L. Rogach, Peter Reiss, Delia J. Milliron, Philippe Guyot-Sionnnest, Gerasimos Konstantatos, Wolfgang J. Parak, Taeghwan Hyeon, Brian A. Korgel, Christopher B. Murray, and Wolfgang Heiss. *Prospects of NanoScience with Nanocrystals.* ACS Nano, 9(2):1012–1057, 2015.

[2] Doris Cadavid, Maria Ibanez, Stephane Gorsse, Antonio M. Lopez, Albert Cirera, Joan Ramon Morante, and Andreu Cabot. *Bottom-up processing of thermoelectric nanocomposites from colloidal nanocrystal building blocks: the case of Ag_2Te-PbTe.* Journal of Nanoparticle Research, 14(12), 2012.

[3] Maria Ibanez, Rachel Korkosz, Zhishan Luo, Pau Riba, Doris Cadavid, Silvia Ortega, Andreu Cabot, and Mercouri G. Kanatzidis. *Electron Doping in Bottom-Up Engineered Thermoelectric Nanomaterials through HCl-Mediated Ligand Displacement .* Journal of the American Chemical Society, 137(36):11854, 2015.

[4] Marek F. Oszajca, Maryna I. Bodnarchuk, and Maksym V. Kovalenko. *Precisely Engineered Colloidal Nanoparticles and Nanocrystals for Li-Ion and Na-Ion Batteries: Model Systems or Practical Solutions?* Chemistry of Materials, 26(19):5422–5432, 2014.

[5] Victor I. Klimov, Alexander A. Mikhailovsky, Shou-Jun Xu, Anton V. Malko, Jennifer A. Hollingsworth, Catherine A. Leatherdale, Hans-Juergen Eisler, and Moungi G. Bawendi. *Optical gain and stimulated emission in nanocrystal quantum dots.* Science, 290(5490):314–317, 2000.

[6] Octavi E. Semonin, Joseph M. Luther, Sukgeun Choi, Hsiang-Yu Chen, Jianbo Gao, Arthur J. Nozik, and Matthew C. Beard. *Peak External Photocurrent Quantum Efficiency Exceeding 100% via MEG in a Quantum Dot Solar Cell.* Science, 334(6062):1530–1533, 2011.

[7] Xihua Wang, Ghada I. Koleilat, Jiang Tang, Huan Liu, Illan J. Kramer, Ratan Debnath, Lukasz Brzozowski, D. Aaron R. Barkhouse, Larissa Levina, Sjoerd Hoogland, and Edward H. Sargent. *Tandem colloidal quantum dot solar cells employing a graded recombination layer.* Nature Photonics, 5(8):480–484, 2011.

[8] Sankaranarayanapillai Shylesh, Volker Schuenemann, and Werner R. Thiel. *Magnetically Separable Nanocatalysts: Bridges between Homogeneous and Heterogeneous Catalysis.* Angewandte Chemie - International Edition, 49(20):3428–3459, 2010.

[9] Katherine Bourzac. *Quantum dots go on display.* Nature, 493(7432):283, 2013.

[10] Ou Chen, Jing Zhao, Vikash P. Chauhan, Jian Cui, Cliff Wong, Daniel K. Harris, He Wei, Hee-Sun Han, Dai Fukumura, Rakesh K. Jain, and Moungi G. Bawendi. *Compact high-quality CdSe-CdS core-shell nanocrystals with narrow emission linewidths and suppressed blinking.* Nature Materials, 12(5):445–451, 2013.

[11] Aurora Rizzo, Yanqin Li, Stefan Kudera, Fabio Della Sala, Marco Zanella, Wolfgang J. Parak, Roberto Cingolani, Liberato Manna, and Giuseppe Gigli. *Blue light emitting diodes based on fluorescent CdSe/ZnS nanocrystals.* Applied Physics Letters, 90(5), 2007.

[12] Wan Ki Bae, Young-Shin Park, Jaehoon Lim, Donggu Lee, Lazaro A. Padilha, Hunter McDaniel, Istvan Robel, Changhee Lee, Jeffrey M. Pietryga, and Victor I. Klimov. *Controlling the influence of Auger recombination on the performance of quantum-dot light-emitting diodes.* Nature Communications, 4, 2013.

[13] Olga I. Micic, Julian R. Sprague, CJ Curtis, KM Jones, Janet L. Machol, Arthur J. Nozik, Harald Giessen, Brian Fluegel, Georg Mohs, and Nasser Peyghambarian. *Synthesis and Characteriszation of InP, GaP, GaInP2 Quantum Dots.* Journal of physical chemistry, 99(19):7754–7759, 1995.

[14] Mickael D. Tessier, Dorian Dupont, Kim De Nolf, Jonathan De Roo, and Zeger Hens. *Economic and Size-Tunable Synthesis of InP/ZnE (E = S, Se) Colloidal Quantum Dots.* Chemistry of Materials, 27(13):4893–4898, 2015.

[15] Woo-Seuk Song, Hye-Seung Lee, Ju Chul Lee, Dong Seon Jang, Yoonyoung Choi, Moongoo Choi, and Heesun Yang. *Amine-derived synthetic approach to color-tunable InP/ZnS quantum dots with high fluorescent qualities.* Journal of Nanoparticle Research, 15(6), 2013.

[16] Renguo Xie, David Battaglia, and Xiaogang Peng. *Colloidal InP nanocrystals as efficient emitters covering blue to near-infrared.* Journal of the American Chemical Society, 129(50):1543215433, 2007.

[17] Liang Li and Peter Reiss. *One-pot synthesis of highly luminescent InP/ZnS nanocrystals without precursor injection.* Journal of the American Chemical Society, 130(35):11588–11589, 2008.

[18] Christopher B Murray, David J. Norris, and Moungi G. Bawendi. *Synthesis and Characterisation of Nearly Monodisperse CdE (E = S, Se, Te) Semiconductor Nanocrystallittes.* Journal of the American Chemical Society, 115(19):8706–8715, 1993.

[19] Zhengtao Deng, Li Cao, Fangqiong Tang, and Bingsuo Zou. *A new route to zinc-blende CdSe nanocrystals: Mechanism and synthesis.* Journal of physical chemistry B, 109(35):16671–16675, 2005.

[20] Jonathan S. Steckel, Brian K. H. Yen, David C. Oertel, and Moungi G. Bawendi. *On the mechanism of lead chalcogenide nanocrystal formation.* Journal of the American Chemical Society, 128(40):13032–13033, 2006.

[21] Haitao Liu, Jonathan S. Owen, and A. Paul Alivisatos. *Mechanistic study of precursor evolution in colloidal group II-VI semiconductor nanocrystal synthesis.* Journal of the American Chemical Society, 129(2):305–312, 2007.

[22] Sofie Abe, Richard Karel Capek, Bram De Geyter, and Zeger Hens. *Tuning the Postfocused Size of Colloidal Nanocrystals by the Reaction Rate: From Theory to Application.* ACS Nano, 6(1):42–53, 2012.

[23] Sofie Abe, Richard K. Capek, Bram De Geyter, and Zeger Hens. *Reaction Chemistry/Nanocrystal Property Relations in the Hot Injection Synthesis, the Role of the Solute Solubility.* ACS Nano, 7(2):943–949, 2013.

[24] Kim De Nolf, Richard K. Capek, Sofie Abe, Michael Sluydts, Youngjin Jang, Jose C. Martins, Stefaan Cottenier, Efrat Lifshitz, and Zeger Hens. *Controlling the Size of Hot Injection Made Nanocrystals by Manipulating the Diffusion Coefficient of the Solute.* Journal of the American Chemical Society, 137(7):2495–2505, 2015.

[25] Jonathan S. Owen, Emory M. Chan, Haitao Liu, and A. Paul Alivisatos. *Precursor Conversion Kinetics and the Nucleation of Cadmium Selenide Nanocrystals.* Journal of the American Chemical Society, 132(51):18206–18213, 2010.

[26] Mark P. Hendricks, Michael P. Campos, Gregory T. Cleveland, Ilan Jen-La Plante, and Jonathan S. Owen. *A tunable library of substituted thiourea precursors to metal sulfide nanocrystals.* Science, 348(6240):1226–1230, 2015.

[27] Peter M. Allen, Brian J. Walker, and Moungi G. Bawendi. *Mechanistic Insights into the Formation of InP Quantum Dots.* Angewandte Chemie International Edition, 49(4):760–762, 2010.

[28] Dylan C. Gary and Brandi M. Cossairt. *Role of Acid in Precursor Conversion During InP Quantum Dot Synthesis.* Chemistry of Materials, 25(12):2463–2469, 2013.

[29] Dylan C. Gary, Benjamin A. Glassy, and Brandi M. Cossairt. *Investigation of Indium Phosphide Quantum Dot Nucleation and Growth Utilizing Triarylsilylphosphine Precursors.* Chemistry of Materials, 26(4):1734–1744, 2014.

[30] Andrew Guzelian, Uri Banin, Andreas Kadavanich, Xiaogang Peng, and Paul Alivisatos. *Colloidal chemical synthesis and characterization of InAs nanocrystal quantum dots.* Applied Physics Letters, 69(10):1432–1434, 1996.

[31] YunWei Cao and Uri Banin. *Growth and properties of semiconductor core/shell nanocrystals with InAs cores.* Journal of the American Chemical Society, 122(40):9692–9702, 2000.

[32] Mark A. Connell, Paul J. Bowyer, P. Adam Bone, Adrian L. Davis, Alistair G. Swanson, Mathias Nilsson, and Gareth A. Morris. *Improving the accuracy of pulsed field gradient NMR diffusion experiments: Correction for gradient non-uniformity.* Journal of Magnetic Resonance, 198(1):121–131, 2009.

[33] Oleg V. Dolomanov, Luc J. Bourhis, Richard J. Gildea, Judith A. K. Howard, and Horst Puschmann. *OLEX2: a complete structure solution, refinement and analysis program.* Journal of Applied Crystallography, 42:339–341, 2009.

[34] George M. Sheldrick. *A short history of SHELX.* Acta Crystallographica Section A, 64(1):112–122, 2008.

[35] Frank H. Allen. *The Cambridge Structural Database: a quarter of a million crystal structures and rising.* Acta Crystallographica Section B - structural science, 58(3, 1):380–388, 2002.

[36] Johan Lindgren and Ivar Olovsson. *hydrogen bond studies .17. crystal structure of dimethylammonium chloride.* Acta Crystallographica Section B - structural chrystallographic and crystal chemistry, B 24(4):549–553, 1968.

[37] VL Abramenko and VS Sergienko. *Synthesis and IR spectroscopical study of molecular complexes of WO_2Cl_2 with o-oxyazomethines. Crystal structure of the product of solvolysis of the WO_2Cl_2 center dot 2HL (HL = salicylidene-beta-naphthylimine) complex.* Russian Journal of Inorganic Chemistry, 47(8):1138–1144, 2002.

[38] P Yan, Y Xie, WZ Wang, FY Liu, and YT Qian. *A low-temperature route to InP nanocrystals.* Journal of Materials Chemistry, 9(8):1831–1833, 1999.

[39] Jannika Lauth, Tim Strupeit, Andreas Komowski, and Horst Weller. *A Transmetalation Route for Colloidal GaAs Nanocrystals and Additional III-V Semiconductor Materials.* Chemistry of Materials, 25(8):1377–1383, 2013.

[40] OI Kolodyazhnyi and N Prinada. *Diad phosphorus-nitrogen prototropism of tris(alkylamino)phosphines.* Russian Journal of General Chemistry, 71(4):646–647, Apr 2001.

[41] Ramon Burgada. *Les Composes Organique Du Phosphore Trivalent A Liaison P - N.* Bulletin de la societe chimique de France, (10):2335, 1963.

[42] Janarthanan Gopalakrishnan. *Aminophosphines: their chemistry and role as ligands and synthons.* Applied Organometallic Chemistry, 23(8):291–318, 2009.

4

Controlling the Size of Hot Injection Made Nanocrystals by Manipulating the Diffusion Coefficient of the Solute[1]

In the previous chapter an overall mechanistic problem was tackled. This chapter, on the other hand, will focus on the effect of the monomer properties on the outcome of the hot injection synthesis. More precisely, the chain length of the ligands used during the synthesis will be related to the size and size dispersion of the nanocrystals formed. CdSe was chosen as the model material, produced via two different syntheses.

4.1 Introduction

Following the widespread use of colloidal nanocrystals as a model system to explore and understand the properties of nanoscale materials and their im-

[1] *Adapted from:* Kim De Nolf, Richard K. Čapek, Sofie Abe, Michael Sluydts, Youngjin Jang, José C. Martins, Stefaan Cottenier, Efrat Lifshitz and Zeger Hens, *Controlling the size of hot injection made nanocrystals by manipulating the diffusion coefficient of the solute*, Journal of the American Chemical Society, *137*, 2495-2505, 2015

plementation as active material in various applications, the reaction mechanism of hot injection syntheses has become an active field of study. This involves both the question as to how precursors convert into a precipitant or solute (also called the growth species or monomer) and how the reaction chemistry is related to the development of the size and size dispersion of the nanocrystals throughout the reaction.[1–3] Importantly, such studies can provide a framework for rationalizing the reaction conditions, such as the choice and the concentration of the precursors and the functional headgroup, chain length, and concentration of the ligands. In some specific cases, including syntheses for PbSe, CdSe, and InP nanocrystals,[4–6] detailed chemical analysis has given insight in the precursor conversion chemistry. On the other hand, kinetic reaction simulations and extensive experimental studies on CdSe and CdS nanocrystal formation have already shown how the rate of precursor conversion is related to the size the nanocrystals attain at the end of the reaction.[7;8] Using the same combination of reaction simulations and an experimental study, it was demonstrated that the often reported increase of the nanocrystal diameter with increasing carboxylic acid concentration - an often used complexing agent - is due to an enhancement of the solute solubility.[9] Importantly, this implies that adjusting the carboxylic acid concentration, opposite from the precursor conversion rate, allows for size tuning at constant reaction rate.

Considering that the solubility of saturated carboxylic acids in apolar solvents decreases with increasing chain length,[10] one could expect a comparable dependence of the nanocrystal diameter on the ligand chain length. In fact, a number of studies have indicated that changing the chain length of the complexing agents, such as carboxylic acids, amines, phosphines or phosphine oxides, provides a versatile and straightforward method to change nanocrystal sizes. In the case of semiconductor nanocrystals, it has been demonstrated that for InP nanocrystals synthesized in the presence of a carboxylic acid, longer chain ligands yield smaller nanocrystals,[11;12] while similar observations have been made for other nanocrystal/ligand combinations such as PbSe,[13] CdS[14] and CdSe/carboxylic acid,[15] and CdSe/amine[16]. Moreover, the same principle has been applied for size tuning in the synthesis of metal and metal oxide nanocrystals, including Co/phosphine,[17] Ag/phosphine oxide[18] and SnO_2/amine[19]. Although the observation that longer chained ligands yield smaller nanocrystals seems quite general, no satisfactory interpretation exists. Most often, it is assumed that this effect reflects a slowing down of the nanocrystal growth rate with increasing chain length due to steric hindrance within the ligand shell.[11;14;19] However, since the growth rate, *i.e.*, the amount of material formed per unit of time, is eventually determined by the rate of solute formation, this interpre-

tation seems flawed and a more in-depth analysis is needed to understand the link between the ligand chain length and the diameter attained by the nanocrystals at the end of the reaction.

In this chapter, we use the quantitative analysis of two different syntheses of CdSe nanocrystals to address the influence of the ligand chain length on the nanocrystal diameter at the end of the reaction. A first based on the hot injection of trioctylphosphine selenide in a mixture composed of a cadmium carboxylate, excess carboxylic acid and primary amines[20;21] and a second involving the injection of selenium powder in a reaction mixture only composed of a cadmium carboxylate and excess carboxylic acid, all dissolved in octadecene.[15] In line with literature, we find that longer carboxylic acids lead to smaller nanocrystals with a better size dispersion. However, opposite from the idea that this results from a reduction of the reaction rate, we show that varying the carboxylic acid chain length leaves the reaction rate unchanged. By combining an experimental study involving carboxylic acid mixtures and previously developed kinetic reaction simulations,[8;9] we show that this size tuning at constant reaction rate is due to a change in solubility and diffusion coefficient of the growth species. The idea that the influence of the ligand chain length on the nanocrystal diameter is due to interaction between the ligand and the growth species is elaborated further by addressing the influence of the chain length of primary amines and phosphine oxides when added to the synthesis. Also in this case, we find that the reaction rate is unchanged when the chain length of any of the additives is varied. However, whereas increasing the chain length of the carboxylic acids or phosphine oxides again reduces the nanocrystal diameter, it follows that amines have little effect, if any, on the nanocrystal diameter. In particular the difference between carboxylic acids and amines is in line with the different complexation of CdSe nanocrystals by carboxylates (tightly bound) compared with amines (loosely bound, dynamic). We thus conclude that varying the ligand chain length in the hot injection synthesis is not only a straightforward method to tune the nanocrystal diameter and optimize size dispersions, yet it is also a sensitive probe to monitor the interaction between the ligand and the actual solute.

4.2 Experimental

CdSe/TOPSe Reference Synthesis. CdSe QDs were synthesized following a previously described procedure.[8] In brief, a mixture of cadmium oleate (0.2 mmol), hexadecylamine (1.6 mmol), OAc (variable amount, molar ratio Cd:oleic acid:hexadecylamine 1:x:8 as indicated) and 1-octadecene

(total volume = 10 mL) were stirred under a nitrogen flow for 30 min at room temperature and 60 min at 100°C. The nitrogen flow was stopped, and still under nitrogen, the temperature was raised to 245°C and 2 mL of a 1M TOPSe solution (2 mmol) was injected and the reaction was performed at 230°C. Aliquots were taken after specific reaction times, weighed, dissolved in a 1:5 mixture of oleic acid and toluene, and precipitated and redispersed using methanol and toluene as the non-solvent and the solvent, respectively. OAc can be replaced by decanoic acid (DAc), myristic acid (MAc) or behenic acid (BAc). For the synthesis work, toluene (> 99.8%), methanol (> 99.85%) and 2-propanol (> 99.7%) were purchased from Fiers; oleic acid (90%) and cadmium oxide (CdO; > 99.99% metals bases) were purchased from Sigma-Aldrich; selenium (99.999%) and 1-octadecene (tech.) were purchased from Alfa Aesar; hexadecylamine (90%) was purchased from Merck and trioctylphospine (TOP, 97%) was purchased from Strem.

CdSe/TOPSe Synthesis Using Different Amines and Phosphine Oxides. To investigate the effect of dative ligands, CdSe QDs were synthesized similarly to the synthesis mentioned above where cadmium oxide (0.2 mmol) and oleic acid (0.8 mmol) were mixed with 1-octadecene. The amount of 1-octadecene was adjusted in the way that the mass of all constituents inside the reaction mixture, after adding amines and phosphine oxides, was 8 g. This mixture was evacuated for 1 h at 110 °C, set under nitrogen and heated up until the mixture turned clear, cooled down to room temperature, opened and the particular amine (1.6 mmol) and phosphine oxide was added without further purification. The mixture was set again under vacuum and evacuated at 110 °C for 1 h, set under nitrogen and the temperature was raised to 245°C. Then 2 mL of a 1 M TOPSe solution (2 mmol) were injected and the reaction was performed at 230°C. Aliquots were taken after specific reaction times, weighed, dissolved in toluene, precipitated and redispersed twice using ethanol and isopropanol as non-solvents, and toluene as solvent. For the synthesis work, toluene, ethanol (> 96%) and 2-propanol were purchased from Gadot; 2-propanol (CP) was purchased from Bio-Lab; oleic acid (90%), 1-octadecene (tech.), cadmium oxide (CdO; > 99.99% metals bases), selenium (99.999%), hexadecylamine (tech.), tri-*n*-octylphosphine oxide (TOPO) (99%) and tri-*n*-butylphosphine oxide (TBPO) were purchased from Sigma-Aldrich; dodecylamine ($DDNH_2$, > 98%), tetradecylamine ($TDNH_2$, > 99%), and octadecylamine ($ODNH_2$, tech.) were purchased from Fluka; and trioctylphospine (TOP, 97%) was purchased from Strem.

CdSe/black Se Synthesis. CdSe QDs were synthesized following a previously described procedure.[15] CdO (0.4 mmol) was added to 10 mL of 1-octadecene together with 1.2 mmol of myristic acid in a three neck flask with cooler under air. The mixture was heated up to 270 °C to form a cadmium carboxylate complex. The heterogeneous 1-octadecene selenium (ODESe) precursor was prepared by adding 0.2 mmol of Se powder to 1 mL of 1-octadecene at room temperature. The resulting unstable dispersion was left stirring, yet no attempt was made to dissolve the Se powder by heating. To initiate the reaction, the heterogeneous ODESe precursor was swiftly injected in the colorless reaction mixture containing the Cd precursor. Injection and growth temperatures were set at 270 and 260 °C, respectively. The black color of the heterogeneous ODESe precursor disappeared upon injection, and the color of the mixture turned from yellow to orange to red depending on the size of the CdSe nanocrystals formed. For quantitative measurements, aliquots were taken after specific reaction times, weighed, dissolved in a 1:5 mixture of oleic acid and toluene, and precipitated and redispersed using methanol and toluene as the non-solvent and the solvent, respectively. The reaction was stopped by thermal quenching using a water bath. The reaction mixture was purified by the addition of toluene, isopropanol and methanol, both in a $1:1:1$ ratio relative to the volume of the reaction mixture. The resulting turbid solution was centrifuged to obtain a precipitate of NCs that was redispersed in toluene. Prior to a second purification step, oleic acid was added in a 10:1 ratio relative to the amount of acid originally used in the synthesis to replace the original carboxylic acid on the surface of the nanocrystals. Next, the purification was repeated twice using toluene and methanol as solvent and non-solvent, respectively to remove all residual reaction products. For the synthesis work, the same products were used as for the CdSe/TOPSe synthesis.

Analysis of Absorption Spectra. UV-vis spectra of purified, weighted aliquots were analyzed quantitatively with a Perkin-Elmer Lambda 2 spectrophotometer.[8] Using the zb-CdSe sizing curve,[22] the mean QD diameter, d_{NC}, is calculated from the peak wavelength of the first exciton transition. This sizing curve relates the position of the first exciton transition to the size of the quantum dot, measured by transmission electron microscopy (TEM). The amount of CdSe formed n_{CdSe} is obtained from the average absorbance of a diluted aliquot at 300, 320, and 340 nm, which is directly proportional to the volume fraction of CdSe.[22] The size distribution is estimated from the half-width at half-maximum of the absorption peak of the first exciton

transition:

$$\sigma_d = \frac{HWHM_\lambda}{d_{QD}\sqrt{2\ln 2}} \frac{\mathrm{d}(d_{QD})}{\mathrm{d}\lambda} \tag{4.1}$$

In the case of a double size distribution due to nanocrystal fusion, the size dispersion plotted is that of the primary set of (not fused) nanocrystals, where the half-widht at half-maximum is estimated by fitting a sum of two Gaussians to the first exciton peak.[9]

Nuclear Magnetic Resonance Spectroscopy. NMR samples of purified NC dispersions are prepared by evaporation of the toluene with a strong nitrogen flow in the glove box. The resulting dry NCs are dissolved in deuterated toluene-d8 (99, 50% D, purchased at Euriso-top) and transferred to an NMR tube (5 mm). Nuclear Magnetic Resonance (NMR) measurements were recorded on a Bruker Avance III Spectrometer operating at a ^{1}H frequency of 500.13 MHz and equipped with a BBI-Z probe or on a Bruker Avance II Spectrometer operating at a ^{1}H frequency of 500.13 MHz and equipped with a TXI-Z probe (channels are ^{1}H, ^{1}3C, ^{3}1P). The sample temperature was set to 298.15 K. Quantitative ^{1}H spectra were recorded with a 20 s delay between scans to allow full relaxation of all NMR signals. The quantification was done by using the Digital ERETIC method. Diffusion measurements (2D DOSY) were performed using a double stimulated echo sequence for convection compensation and with monopolar gradient pulses.[23] Smoothed rectangle gradient pulse shapes were used throughout. The gradient strength was varied linearly from 2-95% of the maximum value (calibrated at 50.2 G/cm) in 64 steps, with the gradient pulse duration and diffusion delay optimized to ensure a final attenuation of the signal in the final increment of less than 10% relative to the first increment. For 2D processing, before Fourier transformation, the 2D spectra were multiplied with a squared cosine bell function in both dimensions. The alkene and methyl proton resonances were corrected prior to integration by subtracting a linear background from the measured intensity.

Reaction simulations. Modeling of the QD synthesis was done by implementing the equations given in Chapter 1 into COMSOL Multiphysics, a commercially available finite-element partial differential equation solver. The parameters used for the reference simulation are given in Section 4.3.4.

4.3 Results and discussion

4.3.1 The effect of the acid chainlength

To investigate the effect of the ligand chain-length in the hot injection synthesis, we used two different syntheses for CdSe nanocrystals. Both make use of a cadmium carboxylate as the Cd precursor, whereas the Se precursor is either TOPSe[8;20;21] or a suspension of black selenium powder in 1-octadecene.[15] Here, we run both syntheses using saturated carboxylic acids with different chain length to analyze the reaction rate and the nanocrystal diameter reached at the end of the reaction, where both syntheses are denoted as CdSe/TOPSe and CdSe/black Se, respectively.

Figure 4.1 summarizes the key properties of the CdSe/TOPSe synthesis. In practice, it involves the injection of TOPSe in a mixture of a cadmium carboxylate ($Cd(CA)_2$), excess carboxylic acid (CA) and hexadecylamine in 1-octadecene (ODE) in a 10 : 1 : 4 : 8 ratio of TOPSe:$Cd(CA)_2$:total CA:HDA, where we use either behenic (BAc, C22), myristic (MAc, C14) or decanoic acid (DAc, C10) as the carboxylic acid. We analyze these reactions by means of the absorption spectra of aliquots taken at different times after the injection. Using the absorbance at short wavelength and the position λ_{1s-1s} of the first exciton peak, this provides us with the reaction yield and the mean nanocrystal diameter d_{NC}.[22]

Figure 4.1a shows that irrespective of the acid chain length, the reaction yield reaches $90 - 100\%$ after 8 minutes of reaction time, where also the overall time development is chain-length independent. Clearly, this indicates that a change of the acid chain length does not slow down nor accelerate the reaction. On the other hand, the absorption spectra recorded on aliquots taken at 8 min after the injection show that shortening the carboxylic acid chain-length results in a progressive increase of λ_{1s-1s} (Figure 4.1b). This corresponds to larger nanocrystals for shorter chain lengths, a trend that holds in fact for all reaction times (Figure 4.1c). In addition, as shown in Figure 4.1d, also the size dispersion – which we estimate from the width of the first exciton transition – tends to increase when the acid chain length is reduced, especially for the shortest chain length used.

As shown in Figure 4.2, similar results are obtained with the CdSe/black Se synthesis, where black selenium powder is injected in a hot mixture of 1-octadecene, a cadmium carboxylate and excess carboxylic acid. Once more, syntheses using behenic acid, myristic acid and decanoic acid are compared. Figure 4.2a confirms that the reaction yield, reaching a final value of $\approx 45 - 50\%$ within 4-8 min for these reactions carried out at re-

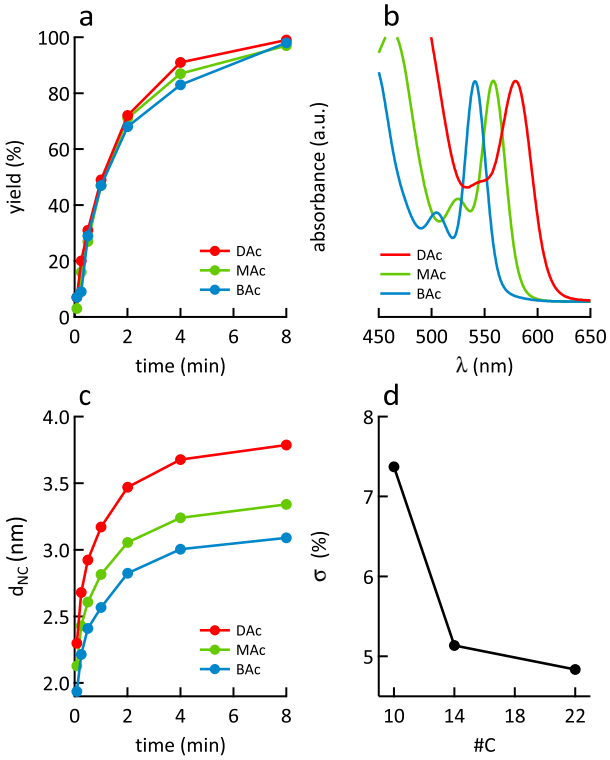

Figure 4.1: a) Yield development of the CdSe/TOPSe synthesis using (blue) behenic, (green) myristic and (red) decanoic acid as the carboxylic acid. b) Absorption spectra recorded on aliquots taken 8 min after injection for the three different acids used. c) Development of the diameter of CdSe nanocrystals during the same syntheses as shown in (a). d) Size dispersion of the CdSe nanocrystals obtained 8 min after injection, plotted as a function of the amount of carbon atoms in the carboxylic acid chain.

spective injection/growth temperatures of 250/240°C, is independent of the carboxylic acid used in this case as well. In addition, shorter chain lengths lead again to larger nanocrystals (see Figure 4.2b-c), whereas especially in the case of decanoic acid, a considerable deterioration of the width of the first exciton transition is observed (see Figure 4.2d).

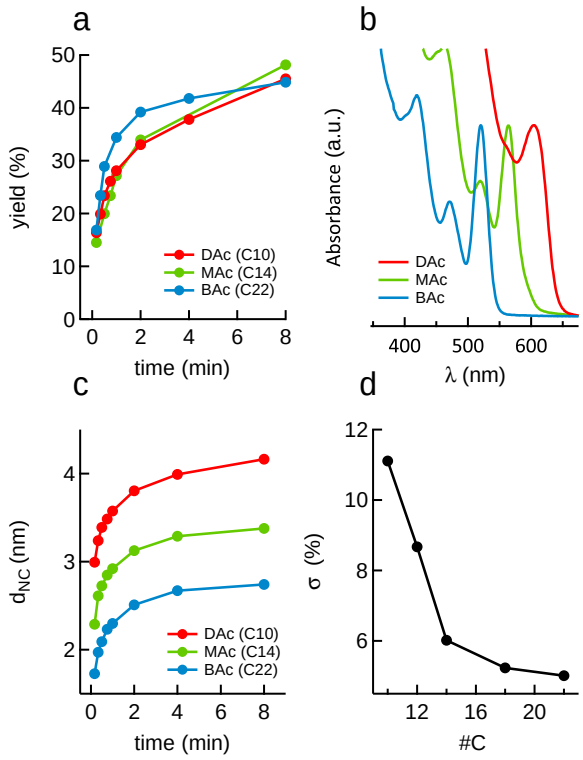

Figure 4.2: a) Yield development of the CdSe/black Se synthesis using (blue) behenic, (green) myristic and (red) decanoic acid as the carboxylic acid using injection/growth temperatures of $250/240°C$, respectively. b) Absorption spectra recorded on aliquots taken 8 min after injection for the three different acids used. c) Development of the diameter of CdSe nanocrystals during the same syntheses as shown in (a). d) Size dispersion of the CdSe nanocrystals obtained 8 min after injection, plotted as a function of the amount of carbon atoms in the carboxylic acid chain for decanoic acid, dodecanoic acid, myristic acid, oleic acid and behenic acid.

At more elevated injection/growth temperatures of $270/260°C$, a similar behavior is observed (Figure 4.3). However, the absorption spectrum of the synthesis conducted with the shortest ligand (decanoic acid) features a significant shoulder. A systematic deconvolution of the different spectra where decanoic acid has been used indicates that this additional feature corresponds to a secondary set of nanocrystals whose diameter exceeds that of the primary set by a factor 1.2 (see Figure 4.4 and Table 4.1). This ratio

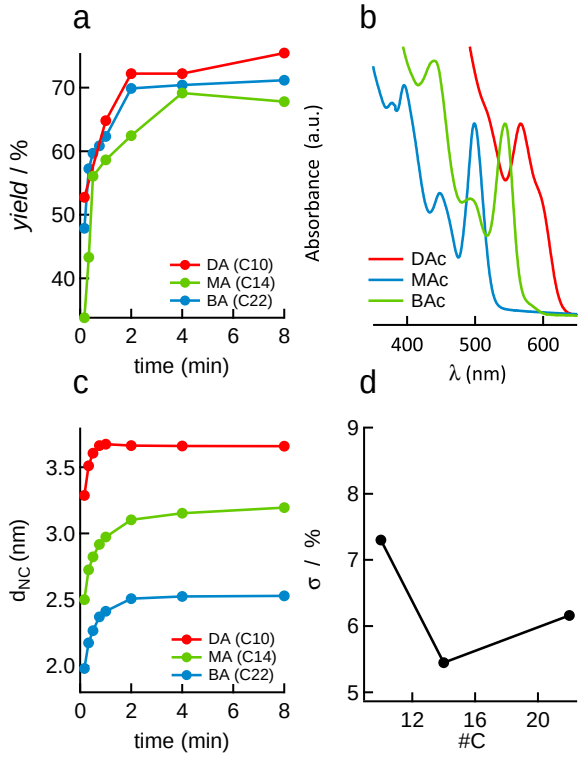

Figure 4.3: a) Yield development of the CdSe/black Se synthesis using (blue) behenic, (green) myristic and (red) decanoic acid as the carboxylic acid using injection/growth temperatures of $270/260°C$, respectively. b) Absorption spectra recorded on aliquots taken 8 min after injection for the three different acids used. c) Development of the diameter of CdSe nanocrystals during the same syntheses as shown in (a). d) Size dispersion of the CdSe nanocrystals obtained 8 min after injection, plotted as a function of the amount of carbon atoms in the carboxylic acid chain.

is close to the expected (1.26) for 2 sets of spherical nanocrystals where the volume of the larger nanocrystals is twice that of the smaller nanocrystals. As a result, we attribute the appearance of this absorption shoulder to nanocrystal fusion at the end of the reaction, leading to a secondary set of nanocrystals with the double volume of those in the primary set. Importantly, nanocrystal fusion only happens during the final stage of the reaction. Hence, it does not influence the balance between nucleation and growth, which is decisive for the size tuning phenomena discussed in this

Table 4.1: Analysis of the spectra displayed in Fig 4.4: center wavelengths and corresponding diameters of the two contributions to the first exciton peak, obtained by fitting the experimental spectrum to a sum of two Gaussians.

Spectrum occurs in	λ_1 (nm)	λ_2 (nm)	d_1 (nm)	d_2 (nm)	d_2/d_1
Fig 4.4a	565	598	3.39	4.02	1.19
Fig 4.4b	547	585	3.11	3.75	1.21
Fig 4.4c	554	589	3.22	3.83	1.19

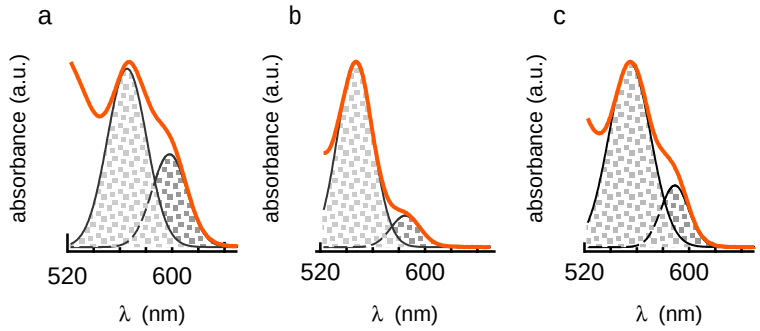

Figure 4.4: Zoom on the first exciton transition of the absorption spectra of CdSe nanocrystals synthesized using black selenium at 270/260°C injection and growth temperature. The figures represent the respective (full orange line) absorption spectra and two separate Gaussians (patterned gray) used for the fit.

manuscript. We thus conclude that longer-chained carboxylic acid ligands in colloidal hot-injection synthesis lead to ensembles of smaller particles with sharper size distributions.

4.3.2 The effect of ligand mixtures

To further investigate the dependence of the nanocrystal diameter and size dispersion on the acid chain length, we performed the CdSe/black Se synthesis using mixtures of carboxylic acids. This involved the combination of saturated carboxylic acids with oleic acid while keeping the overall acid concentration constant. Figure 4.5a indicates that these reactions feature the same yield development, reaching a constant yield of $\approx$ 70% within 2-4 min. The respective absorption spectra of aliquots taken after a reac-

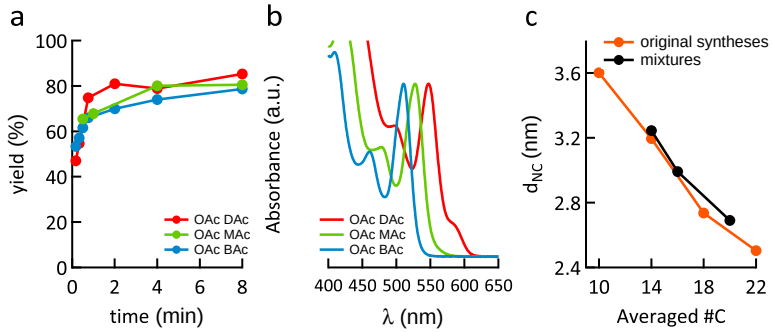

Figure 4.5: a) Yield development of the CdSe/black Se synthesis using 1:1 mixtures of (green) behenic, (black) myristic and (red) decanoic acid with oleic acid using injection/growth temperatures of $270/260^{\circ}\mathrm{C}$, respectively. b) Absorption spectra recorded on aliquots taken 8 min after injection for the three different acid mixtures used. The long wavelength shoulder in the oleic acid - decanoic acid spectra is due to nanocrystal fusion c) Diameter attained after 8 min of reaction time for (black markers) CdSe/black Se syntheses using a single saturated carboxylic acid and (orange markers) 1:1 mixtures of a saturated carboxylic acid and oleic acid as a function of the average number of carbon atoms of the carboxylic acids.

tion time of 8 min for syntheses performed using mixtures of decanoic acid, myristic acid and behenic acid with oleic acid in a 1:1 ratio are shown in Figure 4.5b. Again, we find that replacing behenic acid by myristic acid and decanoic acid in the mixture leads to a reduction of λ_{1s-1s} (and thus d_{NC}). Moreover, λ_{1s-1s} obtained for a carboxylic acid mixture of decanoic acid (C10) and oleic acid (C18, unsaturated) nearly coincides with λ_{1s-1s} obtained using only myristic acid (C14), whose number of carbon atoms is the average of that of decanoic acid and oleic acid (see Figure 4.5c). The same conclusion holds for λ_{1s-1s} attained with the other acid mixtures, which almost perfectly fit the trend line obtained by syntheses with a single, saturated carboxylic acid only. Finally, also in terms of size dispersion, the outcome of reactions using carboxylic acid mixtures strongly resembles the results obtained using a single saturated acid with an equivalent number of carbon atoms. Hence, we conclude that the final diameter of the NCs mainly depends on the average chain length of the carboxylic acid mixture used.

4.3.3 Takover of nucleation by growth

In the mechanistic picture put forward for nanocrystal syntheses such as the CdSe/TOPSe reaction, the precursors first react to form the solute or monomer species that is then used to nucleate and grow CdSe nanocrystals. Next to detailed molecular studies that have appeared in the literature,[4–6] a strong argument supporting this view is the finding that the same yield development is obtained under reaction conditions where the concentration and the size of the nanocrystals is different.[8] This behavior is confirmed in this study for both the CdSe/TOPSe and CdSe/black Se synthesis, which brings us to the conclusion that in both cases, the rate of nucleation and growth of nanocrystals is set by the rate of solute formation. Under these conditions, nanocrystals with different sizes can be obtained by shifting the point where the solute consumption by nanocrystal growth overtakes the solute consumption by nucleation (for a detailed explanation, see Section 1.2 at page 8).[9] Hence the question as to how the ligand chain length affects this takeover.

To analyze this question, we start from the expressions for the rate of nanocrystal nucleation J_N (*i.e.*, the number of nuclei formed per second) and nanocrystal growth J_G (*i.e.*, the change of the NC radius per second) that were introduced in Chapter 1. Both depend on parameters such as the diffusion coefficient D of the solute, the volume of a solute molecule v_0, the surface tension γ, the molar volume V_m of the material formed, the nanocrystal radius r, the rate constants k_g^∞ and k_d^∞ for solute adsorption and desorption, the transfer coefficient α for solute adsorption and the supersaturation S, which is defined as the ratio between the actual concentration and the solubility $[\mathrm{M}]_0$ of the solute:[24]

$$J_N = \frac{2D}{v_0^{5/3}} \exp\left(-\frac{16\pi\gamma^3 V_m^2 N_A}{3(RT)^3(\ln S)^2}\right) \tag{4.2}$$

$$J_G = DV_m [\mathrm{M}]_0 \left[\frac{S - \exp\left(-\frac{2\gamma V_m}{rRT}\right)}{r + \frac{D}{k_g^\infty}\exp\left(\alpha\frac{2\gamma V_m}{rRT}\right)}\right] \tag{4.3}$$

To understand how the different variables in these expressions influence d_{NC} at constant reaction rate, we consider a point in time right after the start of the reaction, where little or no nanocrystals have been formed. Under these conditions, all solute species generated are to be consumed by nucleation.

Table 4.2: Overview of the different adjustable parameters in the expression for the nucleation rate J_N (Equation 4.2) and the growth rate J_G (Equation 4.3). When increasing these parameters, arrows up or down indicate an ensuing increase or decrease of J_N, J_G, the nanocrystal diameter d_{NC} and the size dispersion σ_d.

Variable	Change analyzed	Effect on J_N	Effect on J_G	Effect on d_{NC}	Effect on σ_d
D - prefactor	↑	↑	-	↓	-
γ	↑	↓	-	↑	↓
k_g^∞	↑	-	↑	↑	↓
D - growth rate	↑	-	↑	↑	↑
$[\mathrm{M}]_0$	↑	-	↑	↑	↑

Writing the initial rate of solute formation as $G_{M,0}$, one can thus write:

$$G_{M,0} = \frac{4\pi r_c^3}{3} \frac{N_A}{V_m} J_N \tag{4.4}$$

Here, r_c is the critical radius, *i.e.*, the radius at which nuclei are stable for the prevailing supersaturation:

$$r_c = \frac{2\gamma V_m}{RT \ln S} \tag{4.5}$$

When the reaction rate is constant, $G_{M,0}$ will be constant as well and thus also the product of J_N and the volume of the critical nuclei. Given the relation between r_c and S, this means that the initial supersaturation will depend on both D – *i.e.,* more in general, the nucleation rate prefactor – and γ. According to Equation 4.2, increasing the prefactor will raise the nucleation rate while increasing γ will lower it. Since $G_{M,0}$ must remain fixed, these changes of parameters must be offset by a change of the supersaturation. In this respect, a variation of S has a much stronger influence on J_N – where S affects the exponent – than on r_c. As a result, an increase of the nucleation rate prefactor will lower S while increasing the surface tension will increase S. Using Equation 4.3, one sees that an increase of the supersaturation leads to a faster nanocrystal growth and thus a faster takeover of nucleation by growth. As summarized in Table 4.2, this makes that an increase of the nucleation prefactor results in smaller nanocrystals, while a larger surface tension will increase d_{NC}. Alternatively, parameters like D, $[\mathrm{M}]_0$ or k_g^∞ can directly influence the growth rate. Again, an increase

of the growth rate will expedite the takeover of nucleation by growth. As summarized in Table 4.2, this implies that an increase of D, $[\mathrm{M}]_0$ or k_g^∞ will lead to larger nanocrystals at the end of the reaction.

4.3.4 Reaction simulations

Importantly, the qualitative statements made in Table 4.2 can be confirmed by using Equations 4.2 and 4.3 to simulate the whole reaction development. The modeling approach used here is based on a kinetic scheme where injected precursors P react to form a solute or monomer M, which precipitates to form QDs:

$$\mathrm{P} \longrightarrow \mathrm{M} \rightleftharpoons \mathrm{QD} \tag{4.6}$$

Following this scheme, the central quantities in the modeling are (1) the concentration distribution $c(r,t)$ of QDs - where the product $c(r,t)dr$ yields the concentration of QDs with a radius between r and $r+dr$ at time t - (2) the supersaturation $S(t)$, which is defined as the ratio between the actual concentration of the solute or monomer and its equilibrium concentration $[\mathrm{M}]_0$ and (3) the precursor concentration [P]. For simplicity, the model assumes a single precursor. The concentration distribution $c(r,t)$ changes with time since new QDs nucleate (index N) and existing QDs grow (index G):[8]

$$\left.\frac{\partial c}{\partial t}\right|_N + \left.\frac{\partial c}{\partial t}\right|_G = J_N \delta(r - r_c) - \frac{\partial (J_G c)}{\partial r} \tag{4.7}$$

In the above expression, we describe nucleation as the formation of QDs with the critical radius r_c at a rate J_N , both given by classical nucleation theory (Equations 1.7 in Chapter 1 and 4.2 of the current chapter). For the growth rate, the expression as proposed by Talapin *et al.* was used (Equation 4.3). Regarding the supersaturation S, we assume that its time-dependence is governed by the generation of monomers from the precursors and by their consumption through the nucleation and the growth of nuclei. Writing the monomer generation rate as G_M, dS/dt thus reads:[8]

$$\frac{dS}{dt} = \frac{1}{[\mathrm{M}]_0}\left\{G_M - \frac{4\pi r_c^3}{3v_0} J_N + \int_0^\infty \frac{4\pi r^3}{3v_0}\frac{\partial (J_G c)}{\partial r} dr\right\} \tag{4.8}$$

Finally, the monomer generation rate G_M also determines the change of the precursor concentration [P] with time. For simplicity, we assume here a first order rate equation which agrees with the experimental CdSe synthesis under conditions of a large Se excess:

$$\frac{d\,[\mathrm{P}]}{dt} = -G_M = -k_1\,[\mathrm{P}] \tag{4.9}$$

The coupled differential equations (4.7), (4.8) and (4.9) were implemented in COMSOL Multiphysics. A one-dimensional simulation domain for the nanocrystal radius ranging from 0 to 4 nm was divided in 512 elements. From 0 to 0.2 nm an absorbing boundary condition was implemented to account for nanocrystal dissolution into monomers. The nucleation term was implemented as a Gaussian function with a width of 0.01 nm, centered 0.03 nm above the critical radius. The monomer diffusion coefficient D was chosen according to measured values for cadmium oleate in toluene at room temperature. The monomer volume was taken as the volume of a single spherical CdSe unit in the zincblende CdSe unit cell. The term $RT/2\gamma V_m$ and the monomer solubility $[\mathrm{M}]_0$ was adjusted to yield a realistic nucleation radius of ≈ 0.5 nm and a final QD concentration and radius comparable to what is obtained in the experiments. The monomer adsorption rate constant k_g^∞ was chosen to be in the diffusion-limited growth regime. The magnitude of the first order monomer generation rate constant was set equal to the experimental value for the product $k_2\,[\mathrm{P_{Se}}]$ obtained from the experimental yield development. Especially in terms of reaction speed, the values for k_1 ($0.03333\ \mathrm{s}^{-1}$) and $[\mathrm{M}]_0$ ($4\,10^{-11}$ mol/L) imply a fast reaction with a low monomer solubility.

Table 4.3: Overview of the different parameters in the reaction simulations and their respective value used for the reference simulation.

Symbol	Parameter Description	Value	Unit
D	Monomer diffusion coefficient	$0.25\,10^{-9}$	m^2/s
v_0	Monomer volume	$1.33\,10^{-29}$	m^3
$[\mathrm{M}]_0$	Monomer solubility	$4\,10^{-8}$	$\mathrm{mol}/\mathrm{m}^3$
T	Absolute temperature	503.15	K
γ	Surface tension	0.2	N/m
α	Transfer coefficient	0.5	–
V_m	Molar volume of CdSe	$3.367\,10^{-5}$	$\mathrm{m}^3/\mathrm{mol}$
k_g^∞	Monomer adsorption rate constant	$5\,10^{-7}/\,[\mathrm{M}]_0$	m/s
k_1	Monomer generation rate constant	0.03333	1/s
$[\mathrm{P}]_0$	Initial precursor concentration	0.01667	mol/L

The influence of D in the nucleation rate prefactor The monomer diffusion constant D is used in the nucleation rate prefactor as a means to

estimate its size. By varying D only in the prefactor, influence of the prefactor size can be isolated. Its effect is fairly limited, leading to a negligible decrease of nanocrystal size d_{NC} and increase of the size dispersion σ_d.

The influence of the surface tension Following Equation 4.2, a higher surface tension implies that a higher supersaturation is required to achieve the same nucleation rate. This enhances the growth rate and thus expedites the takeover of nucleation by growth. Due to the exponential dependence of the nucleation rate on the surface tension, nanocrystal concentration and size are very sensitive to the surface tension. Since the ratio D/k_g^∞ stays put in these simulations, the enhanced growth rate strongly promotes size distribution focusing, contrary to what would be expected experimentally.

The influence of k_g^∞ Starting from the reference values for the different parameters (see Table 4.3), the monomer adsorption rate constant k_g^∞ has been progressively increased. Following Equation 4.3, this implies that the growth rate goes up, while the reaction is pushed even further into the diffusion-limited regime. Again, the enhanced growth rate expedites the takeover of nucleation by growth, which leads to larger particles. In this case, the effect is limited since the reference simulation is already close to diffusion limitation. However, also in this case, larger sizes correspond to more narrow size distributions, opposite from the experimental observation.

The influence of D in the growth rate Raising D in the growth rate leads to an increased growth rate, resulting in a faster takeover of nucleation by growth. This in turn results in less, but larger, nanocrystals at the end of the reaction.

The influence of $[\mathrm{M}]_0$ Similar to the effect of raising D, an increase of $[\mathrm{M}]_0$ will enhance the growth rate, leading again to fewer yet larger nanocrystals.

Considering the different parameters introduced, one can expect γ, k_d^∞ and k_g^∞ to be directly influenced by the composition and the dynamical properties of the nanocrystal ligand, whereas $[\mathrm{M}]_0$ and D will be properties of the solute. This makes it possible to link the experimentally observed size and size-distribution tuning to one of these parameters by means of well-designed experiments.

4.3.5 Solute solubility

In the case of the CdSe/black Se synthesis, carboxylic acids are the only ligand used in the reaction. One can therefore assume that carboxylic acids or carboxylates will coordinate the solute and render it soluble. The same description has been put forward for the solute formed in reactions similar to the CdSe/TOPSe reaction used here.[6;9] The fact that the solubility of carboxylic acids in apolar solvents goes down with increasing chain length,[10] thus brings us to the assumption that also the solubility of the CdSe solute should decrease with increasing chain length. This provides a first possible interpretation of the observed size tuning at constant reaction rate since an increase of the solute solubility results in the formation of larger nanocrystals with a broader size distribution at the end of the reaction.[9]

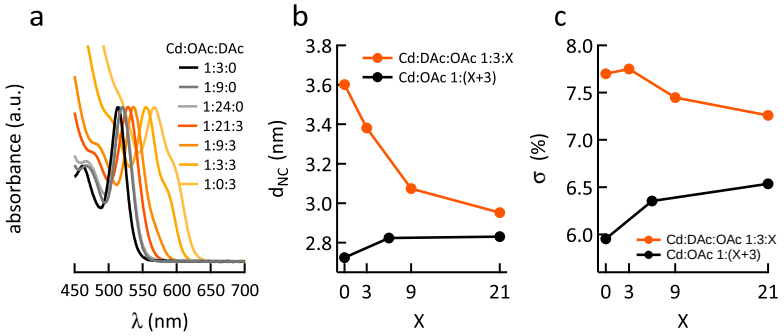

Figure 4.6: Overview of experiments where oleic acid is added to a CdSe/black Se synthesis run with (red) decanoic acid and (black) oleic acid. a) Absorption spectra of the final product of every synthesis. b) Final nanocrystal diameter in function of the amount of extra oleic acid in the synthesis. The long wavelength shoulders in the 1:0:3 and 1:3:3 spectra are due to nanocrystal fusion. c) Size dispersion of the nanocrystals formed as a function of the amount of extra oleic acid added. See methods section for details on the synthesis and the determination of the nanocrystal diameter and size dispersion.

To investigate this hypothesis, we progressively added oleic acid to a decanoic acid-based CdSe/black Se synthesis, while keeping the amount of decanoic acid constant. If the observed size-tuning effect would only be related to the CdSe solute solubility, we expect to observe an increasing particle size and size distribution when increasing the oleic acid ligand concentration in line with various previous literature studies.[7;9;25] Figure 4.6a represents the absorption spectra recorded on the final reaction product

for all syntheses, whereas Figure 4.6b-c show the final d_{NC} and σ_d of the CdSe nanocrystals obtained from these spectra as a function of the (relative) amount of oleic acid used. One sees that rather than increasing d_{NC} and σ_d, the addition of oleic acid to a decanoic acid-based synthesis systematically reduces both d_{NC} and σ_d. These trends strongly contrast with the increase of both parameters when the amount of oleic acid in an oleic acid-based synthesis is raised (black markers in Figure 4.6a-b), a behavior in line with previous literature findings.[9] We thus conclude that changing the ligand chain length in a hot injection synthesis affects other parameters, next to the solute solubility, that have an influence on the balance between the nucleation and growth rate.

4.3.6 The surface tension and the surface reaction

The surface tension corresponds to the free energy per surface area of the nanocrystals formed. As such, it can depend on the nature of the adsorbed ligands, where both the binding of the ligands to the nanocrystal and the mutual, interligand van der Waals interactions between the ligands may contribute. By changing the carboxylic acid chain length, the interligand interactions change, which may affect the nanocrystal surface tension. According to Table 4.2 and the simulations in Section 4.3.4, this could account for the observed link between larger nanocrystals and shorter ligands provided that a reduction of the ligands length increases the surface tension. However, in the case that shorter ligands indeed lead to a higher surface tension, free energy minimization dictates that syntheses in ligand mixtures should result in nanocrystal surfaces enriched in the longer ligand.

To verify this, we determined the ligand shell composition by solution NMR of two batches of CdSe nanocrystals synthesized using the CdSe/black Se reaction using either pure oleic acid or a 1:1 oleic acid:decanoic acid mixture. Figure 4.7 shows the ^{1}H NMR spectra recorded on both types of nanocrystals dispersed in toluene-d_8. In the case of the oleic acid only sample (Figure 4.7a), we obtain a ratio between the integrated intensities of the alkene and methyl protons at respectively 5.72 and 1.07 ppm of 2:3.5, which is close to the expected 2:3 for pure oleic acid. For the CdSe nanocrystals synthesized in the 1:1 oleic acid:decanoic acid mixture, this intensity ratio increases to 2:6.1. Including the errors related to the background correction, this corresponds to a oleic acid and decanoic acid fraction in the ligand shell of 0.53 ± 0.05 and 0.47 ± 0.05, respectively. This number closely corresponds to the composition of the reaction mixture. We therefore conclude that there is little enrichment of the ligand shell in either of the two ligands, meaning that the ligand chain length has no significant effect on the na-

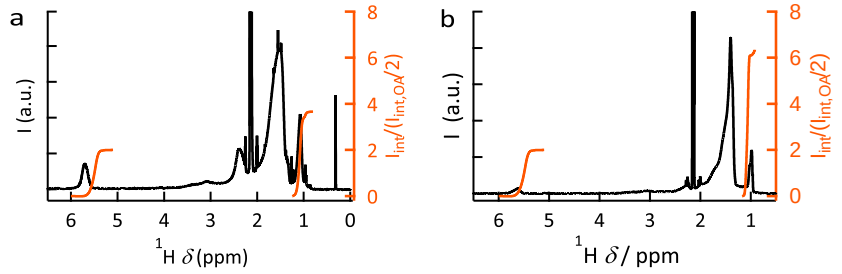

Figure 4.7: 1D ^{1}H NMR spectra of purified CdSe nanocrystal dispersions synthesized with the CdSe/black Se synthesis using a) oleic acid and b) a 1:1 oleic acid:decanoic acid ligand mixture. In orange the integrated intensity of the alkene (≈ 5.85 ppm) and methyl (≈ 1.1 ppm) protons is shown. Integrated intensities are normalized at half the integrated intensity of the alkene protons. The nanocrystal diameter amounts to 2.7 and 3.2 nm for the oleic acid and the oleic acid:decanoic acid synthesis, respectively and both NMR spectra were recorded in toluene-d_8 at 298.15 K.

nocrystal surface tension. This paradoxical outcome can be understood by acknowledging that the surface tension is actually the surface contribution of the free energy *difference* between a nanocrystal and its dissolved constituents, *i.e.*, solute and ligands. Although the interligand van der Waals interactions will be reduced for shorter ligands, so will be the van der Waals interactions between the ligands and the solvent. The absence of preferential adsorption indicates that both contributions largely cancel when their difference is considered.

Considering the rate constant for solute adsorption k_g^∞, an argument often found in the literature is that shorter ligands make the surface more accessible for the solute, thus resulting in larger rate constants for solute adsorption and desorption.[11;14;19] According to Table 4.2, this should indeed lead to larger nanocrystals since it favors growth over nucleation although k_g^∞ only has a pronounced influence on d_{NC} in a kinetic growth regime, where $D/k_g^\infty \gg r$. The simulations however only reproduce experimental diameters and size dispersions when run in or close to diffusion limitation, with the ratio D/k_g^∞ amounting to 1/50 nm for the standard simulation shown in 4.3.4. Moreover, increasing k_g^∞ will only push the synthesis further into diffusion limitation. This means that the more the chain length of the carboxylic acids is reduced, the smaller the additional increase of d_{NC} will be and the more narrow the size dispersion. Since this doesn't agree with the experimental results, we conclude that the acid chain length

has either no influence on k_g^{∞} or that this influence does not affect d_{NC} since nanocrystal growth in the syntheses studied is in or close to diffusion control.

4.3.7 The diffusion coefficient of the carboxylic acid ligand

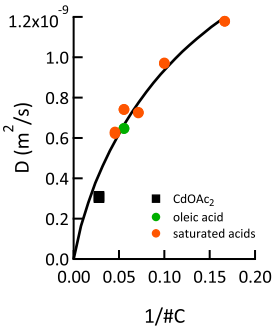

Figure 4.8: Diffusion coefficients of (orange circles) different saturated carboxylic acids, (green marker) oleic acid and (black marker) cadmium oleate determined at 298.15 K in toluene-d_8 using diffusion ordered ^{1}H NMR spectroscopy as a function of the reciprocal of the number of carbon atoms in the respective hydrocarbon chains. The black line is a fit to the expression for the diffusion coefficient of a freely rotating ellipsoid.

As argued before, it can be assumed that the carboxylic acids used in the CdSe/TOPSe or CdSe/black Se synthesis will coordinate the solute that is formed out of the precursors. As a result, changing the hydrocarbon chain length may also affect the diffusion coefficient of the solute, which is a parameter entering the expression for the nanocrystal growth rate. To assess the possible change in diffusion coefficient one could expect, we used diffusion ordered ^{1}H NMR spectroscopy to determine the diffusion coefficient of cadmium oleate ($Cd(OAc)_2$) and different carboxylic acids at room temperature in toluene-$d8$ (Figure 4.8). Carboxylic acids were used instead of cadmium carboxylates since cadmium carboxylates made using saturated carboxylic acids are insoluble in toluene-d_8 at room temperature. We refrained from using DOSY measurements at elevated temperature since convection artefacts makes the thus determined diffusion coefficients unreliable. Cadmium oleate was made in such a way that no excess of oleic acid was present, to avoid free oleic acid influencing the measurements. Figure 4.8 shows the thus obtained diffusion coefficients, plotted as a function of the

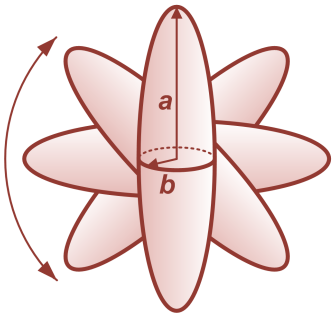

Figure 4.9: Representation of a freely rotating prolate ellipsoid of revolution with an indication of the the radii a and b of the principle axes.

reciprocal of the number of carbon atoms ($x = 1/\#$ C) in the respective hydrocarbon chains. To interpret the data, we start from the expression for the diffusion coefficient D of a randomly moving, prolate ellipsoid of revolution with principle axes of radius a and b (see Figure 4.9):[26]

$$D = \frac{kT}{6\pi\eta a} \ln\left(\frac{2a}{b}\right) \tag{4.10}$$

Here, k_B is the Boltzmann constant, T is the temperature and η is the viscosity of the solvent.
Looking at a carboxylic acid as a long ellipsoid where the long axis is proportional to the number of carbon atoms, we therefore fitted the measured diffusion coefficients to a function $f(x) = Ax\ln(B/x)$ where x represents the reciprocal of the number of carbon atoms ($x = 1/\#$ C). Considering A and B as adjustable parameters, a best fit is obtained for $A = 3.438\,10^{-9}$ m^2/s and $B = 1.322$. Using Equation 4.10, these numbers can be compared with the expected when starting from the known dimensions of carboxylic acids. Since the angle between the C-C bonds of sp^3 hybridized C atom is 109.5°, the total length of a carboxylic acid can be expressed in terms of the C-H, C-C, C-O and O-H bond length as:

$$\begin{aligned} a &= \sin\left(\frac{109.5}{2}\right)\left(l_{C-H} + (x^{-1}-1)l_{C-C} + l_{C-O} + l_{O-H}\right) \\ &= 0.817 \times \left(0.7 + (x^{-1}-1) + 0.92 + 0.623\right) l_{C-C} \\ &= \left(0.817x^{-1} + 1.015\right) l_{C-C} \end{aligned} \tag{4.11}$$

Similarly, the width of the rod can be expressed in terms of the C-H bond

length:

$$\begin{aligned} b &= \cos\left(\frac{109.5}{2}\right) \times (l_{C-H} + l_{C-C} + l_{C-H}) \\ &= 0.577 \times (0.7 + 1 + 0.7)\, l_{C-C} \\ &= 1.385 l_{C-C} \end{aligned} \tag{4.12}$$

Neglecting the constant contribution to the rod length, we thus obtain a theoretical relation between the fitting parameters and measurable quantities such as the solvent viscosity and the C-C bond length:

$$A_{th} = \frac{kT}{6\pi\eta} \times \frac{1}{0.817 l_{C-C}} = 2.94\,10^{-9}\ \mathrm{m}^2/\mathrm{s} \tag{4.13}$$

$$B_{th} = \frac{2 \times 0.817}{1.385} = 1.18 \tag{4.14}$$

The close agreement between these theoretical A and B coefficients and those obtained from a fit to the experimental diffusion coefficients confirms that carboxylic acids and cadmium oleate can be seen as freely diffusing rod like objects, whose diffusion coefficient scales with the inverse of the chain length.

We can conclude that the obtained diffusion coefficients follow a trend described by a function for freely rotating rod-like objects, where for long rods, the diffusion coefficient becomes proportional to the rod length. In this respect, we find that the diffusion coefficient of oleic acid is approximately twice as large as the one of $Cd(OAc)_2$, meaning that $Cd(OAc)_2$ can roughly be described as an object that is twice as long as one oleic acid molecule. Hence when indeed carboxylic acids coordinate the solute, this result indicates that we can directly link a change in the carboxylic acid chain length to a variation of the diffusion coefficient of the solute.

4.3.8 Linking the solute diffusion coefficient to the ligand chain length

As already mentioned in Section 4.3.4, the solute diffusion coefficient enters both in the prefactor of the nucleation rate and in the expression for the growth rate. Linking the solute diffusion coefficient to the ligand chain length, this provides two possible routes by which the ligand chain length can affect the balance between nucleation and growth. Increasing the nucleation prefactor to accommodate for shorter ligands - and thus a higher diffusion coefficient - results in smaller nanocrystals (see Table 4.2 and Section 4.3.4). However, since only a small change in supersaturation is needed

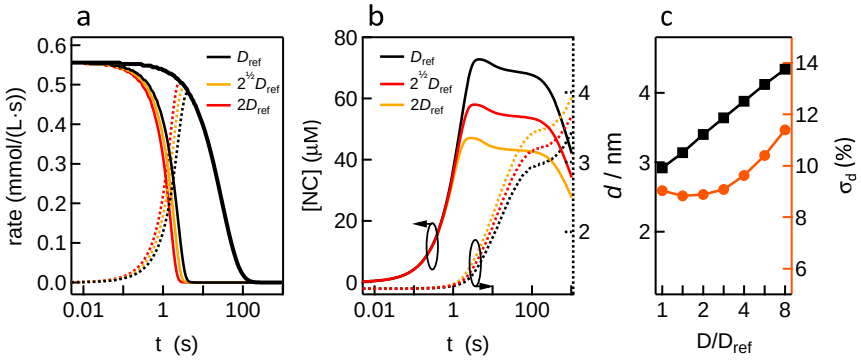

Figure 4.10: a) Rates of (bold lines) solute generation, (full lines) solute consumption by nucleation and (dashed line) solute consumption by growth for simulations of the hot injection synthesis based on a comprehensive model incorporating nucleation and growth of nanocrystals out of solute generated from the injected precursors. Three different diffusion coefficients for the solute are used, (black) $D_{ref} = 0.25\,10^{-9}\,\mathrm{m}^2/\mathrm{s}$, (red) $\sqrt{2}D_{ref}$ and (green) $2D_{ref}$. b) Time development of the concentration and the diameter of the nanocrystals for the three reaction simulations. The same color code is used to indicate simulations with different diffusion coefficients. c) Representation of (blue squares) diameter and (red circles) size dispersion after 90 s of reaction time as a function of the solute diffusion coefficient, represented as D/D_{ref} on a logarithmic axis.

to offset the increased prefactor and obtain the same nucleation rate, the effect is negligible. Moreover, inspecting the assumptions made in deriving Equation 4.2, it follows that the solute diffusion coefficient enters the prefactor only to assess the dissolution rate of critical nuclei.[27] Writing the nucleation prefactor in terms of the solute diffusion coefficient should therefore be seen as a way to estimate its order of magnitude and not as a true functional relation between both. Therefore we conclude that changing the ligand chain length may well affect the solute diffusion coefficient, but will not influence d_{NC} through the (apparent) dependence of the nucleation prefactor on D.

As can be seen in Equation 4.3, the solute diffusion coefficient also directly influences the nanocrystal growth rate, especially for reactions run close to or in diffusion control. Here, an increase of D raises the growth rate, and the concomitantly faster takeover of nucleation by growth makes that less nuclei form such that they can grow larger by the end of the reaction. Fig-

ure 4.10 shows the results of reaction simulations implementing Equation 4.2 and Equation 4.3 that clarify this point (see Section 4.3.4). The reference synthesis shown in black is based on a parameter set that makes that the simulated reference reaction has a comparable rate and yields a similar d_{NC} as the experimental syntheses studied here. First of all, Figure 4.10a shows the different rates involved in the formation and consumption of solute. In line with the argument made previously, one sees that all solute species formed (bold line) are initially consumed by nucleation (full line), which is later overtaken by consumption through growth (dashed line). After the suppression of the nucleation, the nanocrystal concentration [NC] is maintained at an approximately steady value and d_{NC} increases to level off when the reaction reaches full yield (see Figure 4.10b). After that, Ostwald ripening results in a drop of the nanocrystal concentration and a further growth of the remaining nanocrystals.

Next to the reference simulation the figure also shows simulation results where D has been multiplied by a factor of $\sqrt{2}$ and 2. Figure 4.10a indicates that a higher diffusion coefficient indeed speeds up the takeover of nucleation by growth. In line with the qualitative statements in Table 4.2, this results in a lower concentration of nanocrystals after nucleation is suppressed and the nanocrystals attain larger diameters when the reaction reaches full yield (Figure 4.10b). Quantitatively, we find that a doubling of the diffusion coefficient relative to the reference conditions raises d_{NC} by $\approx 0.5\,\text{nm}$ and Figure 4.10c indicates that this increase continues when raising D even further. Importantly, this predicted change is in line with the changes found experimentally when comparing syntheses run using decanoic acid (C10) or behenic acid (C22), where a difference in diffusion coefficient of ≈ 2 can indeed be expected. Figure 4.10c also lists σ_d at the point where the reaction reaches full yield. One sees that an initial increase of D relative to the D_{ref} has little effect on σ_d. On the other hand, raising D further leads to a progressive increase of σ_d, in line with what was reported before for a solubility increase.[9] This trend can be understood from Equation 4.3, which makes clear that increasing D will shift the growth from diffusion to kinetic control, thus reducing size distribution focusing. We thus conclude that at least part of the increase of d_{NC} observed when reducing the chain length of the carboxylic acids in the CdSe/TOPSe and CdSe/black Se synthesis can be due to an increase of the solute diffusion coefficient.

4.3.9 Size tuning is a result of solute diffusion coefficient and solubility

Various studies on the synthesis of metal, metal oxide or semiconductor nanocrystals have mentioned that a reduction of the ligand chain length - being either carboxylic acids, amines, phosphines or phosphine oxides - leads to larger nanocrystals.[11–19] When discussed, this effect has been attributed to an overall slowing down of nucleation and growth for longer chains, tentatively linked to an increase of steric hindrance.[11;14;19] Opposite from this interpretation, we find for the two different CdSe syntheses studied here that a change of the ligand chain length has no noticeable influence on the reaction rate. If the combined rate of solute consumption by nucleation and growth remains the same, the observed size tuning can only be due to a change of the moment where the increasing consumption of solute by nanocrystal growth suppresses the nucleation of new nanocrystals. Although the different composition of the ligand shell could play a role here - either through a variation of the solute adsorption rate k_g^∞ or the surface free energy γ - only a change of the solute diffusion coefficient D and the solute solubility $[\mathrm{M}]_0$ yield the experimentally observed combined increase of the nanocrystal diameter d_{NC} and size dispersion σ_d when simulating the reactions.

Including the experimental results shown in Figure 4.5 and 4.6, both relations explain why the use of pure acids or acid mixtures with the same average chain length yield the same nanocrystal diameter. When the carboxylic acids coordinate the solute, both its solubility and its diffusion coefficient will indeed be an average taken over the different carboxylic acids used. On the other hand, only the connection between the ligand chain length and the solute diffusion coefficient can explain why d_{NC} goes down when oleic acid is added to a synthesis run using decanoic acid only. In that case, the solubility is supposed to go up – leading to larger nanocrystals – hence the slight increase in d_{NC} observed when more oleic acid is added to a synthesis already run using oleic acid. On the other hand the replacement of decanoic acid by oleic acid as a coordinating species for the solute will reduce its diffusion coefficient by about a factor of 2, which explains the experimentally observed marked drop in d_{NC}. However, one sees that in particular for the CdSe/black Se synthesis the actually measured change in d_{NC} as a function of the acid chain length exceeds the variation expected from the simulations. When D is raised by about a factor of 2 (DAc *versus* BAc), d_{NC} increases by $\approx$ 1 nm whereas only $\approx$ 0.5 nm is predicted. Since D and $[\mathrm{M}]_0$ play a very similar role in the reaction simulations (see Supporting Information section S3 and S4), this indicates that the increase of d_{NC} most likely re-

sults from the joint increase of the diffusion coefficient and the solubility of the solute when reducing the chain length of the carboxylic acids.

4.3.10 Dative ligands: amines and phosphonic acids

The conclusion that the ligand chain length influences d_{NC} through its effect on the diffusion coefficient or the solubility of the solute suggests that a change in diameter will occur only if the ligands interact to some extent with the solute – either through direct (inner sphere) or a more loose (outer sphere) coordination. Formulated in this way, one sees that the chain length/d_{NC} relation could be used to probe possible interactions between a reaction additive and the solute. Considering the binding of ligands to nanocrystals such as CdSe, it has been well established that carboxylic acids adsorb as tightly bound, X-type carboxylate species.[28;29] Amines on the other hand are dative L-type ligands that are more loosely bound and exhibit a rapid adsorption/desorption behavior.[30] This different coordination behavior at the level of the nanocrystals raises the question as to how the diffusion coefficient of the solute and thereby the size and size-distribution development of nanocrystals during a synthesis will be affected by a change of the ligand chain of a dative, L-type ligand. To analyze this, we studied the yield, size and size distribution development of the CdSe/TOPSe syntheses using saturated, primary amines with different chain lengths. Here, the concentration of the amine was kept comparatively low so that it can be assumed that changes of the solubility will play a minor role.[9]

As shown in Figure 4.11a, we again find the same yield development for different CdSe/TOPSe syntheses run using n-dodecylamine ($DDNH_2$, C12), n-tetradecylamine ($TDNH_2$, C14), n-hexadecylamine ($HDNH_2$, C16) and n-octadecylamine ($ODNH_2$, C18). Hence, changing the amine chain length has no effect on the reaction rate. In this case however, also the absorption spectra recorded on aliquots taken after 8 min of reaction time show little variation, if any (see Figure 4.11b). We thus conclude that the outcome of the CdSe/TOPSe synthesis is almost independent of the chain length of the amine used. In line with this finding, Figure 4.11c shows the room temperature diffusion coefficient of $Cd(OAc)_2$ dissolved in toluene, again determined using DOSY, with and without the presence of octadecylamine ($ODNH_2$, C18). Ocatdecylamine has no significant influence on this diffusion coefficient within the precision of the measurement. This correspondence - albeit recorded on $Cd(OAc)_2$ and not on the actual solute - further supports the interpretation put forward that the strong effect of the ligand chain-length on the nanocrystal diameter observed for carboxylic acids is related to the acid coordinating the solute and thus changing its diffusion coefficient. With

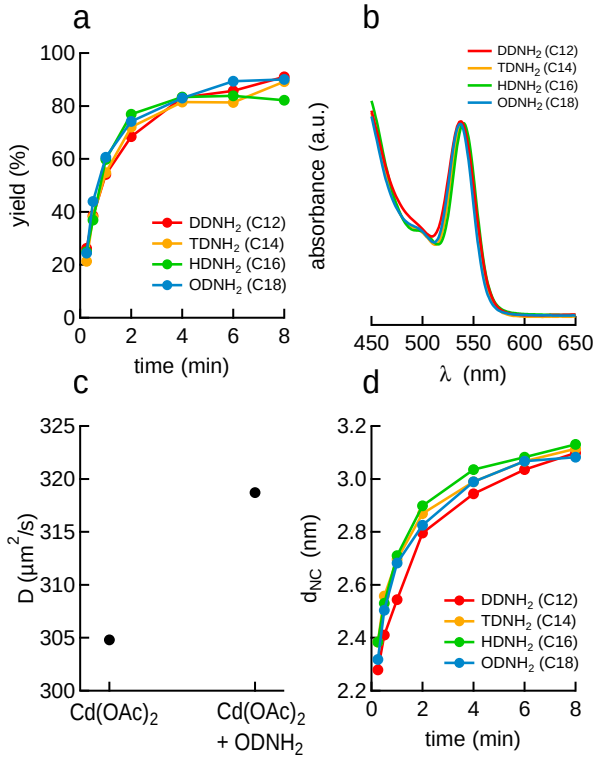

Figure 4.11: a) Time development of the reaction yield of CdSe/-TOPSe syntheses run using primary amines with different hydrocarbon chain length, including $DDNH_2$, $TDNH_2$, $HDNH_2$ and $ODNH_2$. b) Absorption spectra recorded on aliquots taken 8 min after injection for the different reactions shown in (a). c) Diffusion coefficient of $Cd(OAc)_2$ in toluene-d_8 at 298.15 K with and without octadecylamine present. d) Time development of the nanocrystal diameter for the different reactions shown in (a).

additives such as amines that show far less interaction with the solute, no influence of the chain length on the final nanocrystal size is observed (see Figure 4.11d).

Besides the diffusion coefficient effect, we have already mentioned that carboxylic acids with a shorter hydrocarbon chain are more soluble in apolar solvents.[10]. Although this was ruled out as the sole origin of the observed size tuning (see Figure 4.6), we already concluded that an increase of the solubility still contributes to the observed size tuning when changing the

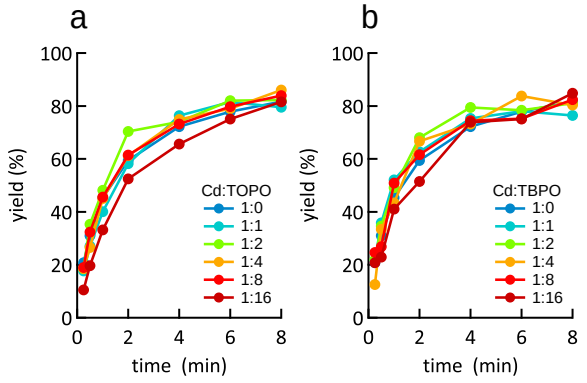

Figure 4.12: Yield development of all CdSe/TOPSe-based reactions with a) tri-n-octylphosphine oxide and b) tri-n-butylphosphine oxide. Reaction mixture: 0.2 mmol $Cd(OAc)_2$, 0.8 mmol Oleic acid, 1.6 mmol HDA, and the particular amount phosphine oxide and 1-octadecene (total mass 8 g). Injection mixture: 2 mL 1 M TOPSe. Injection and growth temperature: 245 and 230°C, respectively.

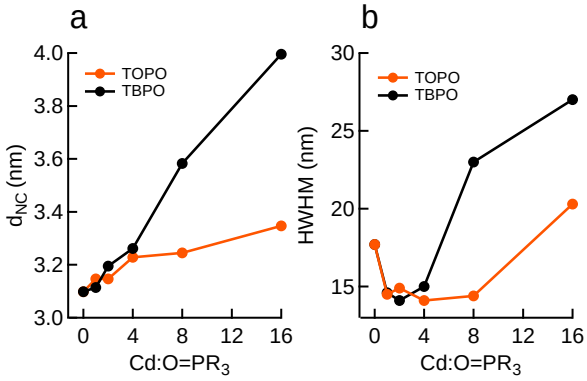

Figure 4.13: Overview of a) nanocrystal diameter and b) spectral width after 8 min reaction time in function of the cadmium to trialkylphosphine oxide ratio inside the reaction mixture for a CdSe/TOPSe-based reaction.

carboxylic acid chain length. It leads to the same observations, namely an increase of the particle size and size distribution when using ligands with shorter hydrocarbon chains[9] and the experimental increase of d_{NC} is larger than expected for the given change in diffusion coefficient. To address this aspect separately and, in doing so, extend the study to yet another ligand

system, trialkylphosphine oxides were added to the CdSe/TOPSe synthesis, where both tri-*n*-butylphosphine oxide (TBPO) and tri-*n*-octylphosphine oxide (TOPO) were used. For both additives, we always analyzed d_{NC} and σ_d attained at the end of the reaction. Similar to all other reactions studied, we find that the yield development is independent of both the concentration and the type of phosphine oxide added (see Figure 4.12). As shown in Figure 4.13 a and b, we find only a minor effect on d_{NC} and σ_d for low phosphine oxide concentrations that is independent of the phosphine oxide used. This lack of influence of the chain length resembles what is found with amines (see Figure 4.11b), suggesting that the main effect is rather due to a change of the solubility of the solute and not its diffusion coefficient. With increasing phosphine oxide concentration, the particles grow larger and the size distribution broadens, indicating a further increase of the solubility of the solute inside the reaction mixture.[9] Furthermore, this effect is stronger for tri-*n*-butylphosphine oxide than for tri-*n*-octylphosphine oxide, which indicates that indeed the solubility will increase more when the hydrocarbon chain-length of the alkylphosphine oxides is shorter. We thus conclude that the ligand chain length can also affect the nanocrystal size and size distribution in a hot injection synthesis by its effect on the solubility of the solute. Given the deterioration of the size dispersion with increasing solubility, this makes long chained ligands favorable in strongly coordinating reaction mixtures since they have a lower impact on the solubility of the solute.

4.4 Conclusion

We have analyzed the relation between the hydrocarbon chain length of ligands added to a hot injection synthesis and the diameter of the nanocrystals thus formed at the end of the reaction. In the case of carboxylic acids, we find for two different syntheses for CdSe nanocrystals that shorter chain lengths result in larger nanocrystals, where especially for the shortest ligands used the size dispersion also deteriorates. This finding is in line with various literature reports, yet opposite from the prevailing explanation that longer ligands slow down the reaction, we find that the ligand chain length has no effect on the reaction rate. Based on a combination of experimental evidence and reaction simulation, we therefore attribute the observed size tuning to a change of the moment where nanocrystal nucleation is overtaken by nanocrystal growth, due to the carboxylic acids affecting both the diffusion coefficient and the solubility of the solute species formed out of the injected precursors. This conclusion suggests that the chain length/d_{NC} relation could be used to probe the degree of interaction between a reaction

additive and the solute, a point we explored further by changing the chain length of amines and phosphine oxides. Especially in the case of amines, the ligand chain length has no noticeable effect on d_{NC}, suggesting little interaction with the solute in line with the weak, dynamic stabilization of CdSe nanocrystals by amines. Hence, this study shows that changing the ligand chain length provides a practical way to tune the nanocrystal diameter at full yield in a hot injection synthesis and enhance the size dispersion, which is key to the application of nanocrystals as light emitters, for example in display applications. Moreover, the ligand chain length can be used to probe the interaction between a reaction additive and the solute, which can lead to better insight in the hot injection synthesis itself.

References

[1] Raul Garcia-Rodriguez, Mark P. Hendricks, Brandi M. Cossairt, Haitao Liu, and Jonathan S. Owen. *Conversion Reactions of Cadmium Chalcogenide Nanocrystal Precursors.* Chemistry of Materials, 25(8):1233–1249, 2013.

[2] Kelly L. Sowers, Brett Swartz, and Todd D. Krauss. *Chemical Mechanisms of Semiconductor Nanocrystal Synthesis.* Chemistry of Materials, 25(8):1351–1362, 2013.

[3] Zeger Hens and Richard K. Capek. *Size tuning at full yield in the synthesis of colloidal semiconductor nanocrystals, reaction simulations and experimental verification.* Coordination Chemistry Reviews, 263-264(0):217–228, 2014.

[4] Jonathan S. Steckel, Brian K. H. Yen, David C. Oertel, and Moungi G. Bawendi. *On the mechanism of lead chalcogenide nanocrystal formation.* Journal of the American Chemical Society, 128(40):13032–13033, 2006.

[5] Peter M. Allen, Brian J. Walker, and Moungi G. Bawendi. *Mechanistic Insights into the Formation of InP Quantum Dots.* Angewandte Chemie International Edition, 49(4):760–762, 2010.

[6] Haitao Liu, Jonathan S. Owen, and A. Paul Alivisatos. *Mechanistic study of precursor evolution in colloidal group II-VI semiconductor nanocrystal synthesis.* Journal of the American Chemical Society, 129(2):305–312, 2007.

[7] Jonathan S. Owen, Emory M. Chan, Haitao Liu, and A. Paul Alivisatos. *Precursor Conversion Kinetics and the Nucleation of Cadmium Selenide Nanocrystals.* Journal of the American Chemical Society, 132(51):18206–18213, 2010.

[8] Sofie Abe, Richard Karel Capek, Bram De Geyter, and Zeger Hens. *Tuning the Postfocused Size of Colloidal Nanocrystals by the Reaction Rate: From Theory to Application.* ACS Nano, 6(1):42–53, 2012.

[9] Sofie Abe, Richard K. Capek, Bram De Geyter, and Zeger Hens. *Reaction Chemistry/Nanocrystal Property Relations in the Hot Injection Synthesis, the Role of the Solute Solubility.* ACS Nano, 7(2):943–949, 2013.

[10] C. W. Hoerr, R. S. Sedgwick, and A. W. Ralston. *The Solubilities of the Normal Saturated Fatty Acids. III.* Journal of Organic Chemistry, 11(5):603–609, 1946.

[11] David Battaglia and Xinguang Peng. *Formation of high quality InP and InAs nanocrystals in a noncoordinating solvent.* Nano Letters, 2(9):1027–1030, 2002.

[12] Derrick W. Lucey, David J. MacRae, Madalina Furis, Yudhisthira Sahoo, Alexander Cartwright, and Paras N. Prasad. *Monodispersed InP quantum dots prepared by colloidal chemistry in a noncoordinating solvent.* Chemistry of Materials, 17(14):3754–3762, 2005.

[13] In Chan Baek, Sang Il Seok, Nimai Chand Pramanik, Sunirmal Jana, Mi Ae Lim, Boek Yeop Ahn, Chang Jin Lee, and Yong Jae Jeong. *Ligand-dependent particle size control of PbSe quantum dots.* Journal of Colloid and Interface Science, 310(1):163–166, 2007.

[14] Jianying Ouyang, Jasmijn Kuijper, Simon Brot, David Kingston, Xiaohua Wu, Donald M. Leek, Michael Z. Hu, John A. Ripmeester, and Kui Yu. *Photoluminescent Colloidal CdS Nanocrystals with High Quality via Noninjection One-Pot Synthesis in 1-Octadecene.* Journal of Physical Chemistry C, 113(18):7579–7593, 2009.

[15] Stijn Flamee, Marco Cirillo, Sofie Abe, Kim De Nolf, Raquel Gomes, Tangi Aubert, and Zeger Hens. *Fast, High Yield, and High Solid Loading Synthesis of Metal Selenide Nanocrystals.* Chemistry of Materials, 25(12):2476–2483, 2013.

[16] Katsuhiro Nose, Hiroshi Fujita, Takahisa Omata, Shinya Otsuka-Yao-Matsuo, Hiroyuki Nakamura, and Hideaki Maeda. *Chemical role of amines in the colloidal synthesis of CdSe quantum dots and their luminescence properties.* Journal of Luminescence., 126(1):21–26, 2007.

[17] Shouheng Sun and Christopher B. Murray. *Synthesis of monodisperse cobalt nanocrystals and their assembly into magnetic superlattices (invited).* J. Appl. Phys., 85(8, 2A):4325–4330, 1999.

[18] Mark Green, Nicholas Allsop, Gareth Wakefield, Peter J. Dobson, and John L. Hutchison. *Trialkylphosphine oxide/amine stabilised silver nanocrystals - the importance of steric factors and Lewis basicity in capping agents.* Journal of Materials Chemistry, 12(9):2671–2674, 2002.

[19] Mauro Epifani, Jordi Arbiol, Raul Diaz, Mariano J. Peralvarez, Pietro Siciliano, and Joan R. Morante. *Synthesis of SnO_2 and ZnO colloidal*

nanocrystals from the decomposition of tin(II) 2-ethylhexanoate and zinc(II) 2-ethylhexanoate. Chemistry of Materials, 17(25):6468–6472, 2005.

[20] Emory M. Chan, Chenxu Xu, Alvin W. Mao, Gang Han, Jonathan S. Owen, Bruce E. Cohen, and Delia J. Milliron. *Reproducible, High-Throughput Synthesis of Colloidal Nanocrystals for Optimization in Multidimensional Parameter Space.* Nano Letters, 10(5):1874–1885, 2010.

[21] Richard K. Capek, Karel Lambert, Dirk Dorfs, Philippe Frederic Smet, Dirk Poelman, Alexander Eychmueller, and Zeger Hens. *Synthesis of Extremely Small CdSe and Bright Blue Luminescent CdSe/ZnS Nanoparticles by a Prefocused Hot-Injection Approach.* Chemistry of Materials, 21(8):1743–1749, 2009.

[22] Richard Karel Capek, Iwan Moreels, Karel Lambert, David De Muynck, Qiang Zhao, Andre/'e Van Tomme, Frank Vanhaecke, and Zeger Hens. *Optical Properties of Zincblende Cadmium Selenide Quantum Dots.* The Journal of physical chemistry C, 114(14):6371–6376, 2010.

[23] Mark A. Connell, Paul J. Bowyer, P. Adam Bone, Adrian L. Davis, Alistair G. Swanson, Mathias Nilsson, and Gareth A. Morris. *Improving the accuracy of pulsed field gradient NMR diffusion experiments: Correction for gradient non-uniformity.* Journal of Magnetic Resonance, 198(1):121–131, 2009.

[24] Dmitri V. Talapin, Andrey L. Rogach, Markus Haase, and Horst Weller. *Evolution of an ensemble of nanoparticles in a colloidal solution: Theoretical study.* Journal of Physical Cemistry B, 105(49):12278–12285, 2001.

[25] Craig Bullen and Paul Mulvaney. *Nucleation and growth kinetics of CdSe nanocrystals in Octadecene.* Nano Letters, 4(12):2303–2307, 2004.

[26] Ken A. Dill and Sarina Bromberg. *Molecular Driving Forces.* Garland Science, New York, 2003.

[27] Arne E. Nielsen. *Kinetics of Precipitation.* Pergamon Press, New York, 1964.

[28] Bernd Fritzinger, Richard K. Capek, Karel Lambert, José C. Martins, and Zeger Hens. *Utilizing Self-Exchange To Address the Binding of*

Carboxylic Acid Ligands to CdSe Quantum Dots. Journal of the American Chemical Society, 132(29):10195–10201, 2010.

[29] Nicholas C. Anderson and Jonathan S. Owen. *Soluble, Chloride-Terminated CdSe Nanocrystals: Ligand Exchange Monitored by ^{1}H and ^{31}P NMR Spectroscopy.* Chemistry of Materials, 25(1):69–76, 2013.

[30] Antti Hassinen, Iwan Moreels, Celso de Mello Donega, Jose C. Martins, and Zeger Hens. *Nuclear Magnetic Resonance Spectroscopy Demonstrating Dynamic Stabilization of CdSe Quantum Dots by Alkylamines.* Journal of physical chemistry Letters, 1(17):2577–2581, 2010.

5

Surface Chemistry of PbSe and CdSe Quantum Dots - a Spectral Hole Burning Study

In this chapter, we study the surface chemistry of CdSe and PbSe quantum dots by means of spectral hole burning experiments and simulations. We attempt to answer questions such as 'How are ligands distributed over the different facets' and 'Is the surface coverage the same for different materials?'.

5.1 Introduction

In the last 20 years, the research about the surface chemistry of colloidal quantum dots (QDs) has gained a lot of interest. Various techniques can be used to examine the surface chemistry. The elemental composition of the quantum dot can be determined by rutherford backscattering spectrometry (RBS).[1] The type of ligands can be identified by NMR, FTIR and many more techniques.[2–4] These techniques can be used to asses the type

of binding of these ligands to the QD surface as well.[5–7] In addition, it is nowadays fairly easy to asses the ligand density of any type of nanocrystal in combination with any type of organic ligand with NMR spectroscopy.

Unfortunately, we are not able to specify how these ligands are distributed over the quantum dot surface. Are these ligands distributed evenly over the complete surface? Or are they bound to specific facets only? Are they found close together in patches on one type of facet? Information about the distribution of ligands can provide insights on the stabilization of the nanocrystals or on ligand exchange.[8] On the one hand, this knowledge can lead to an improved surface passivation, which in turn can lead to a higher photoluminescence quantum yield (PLQY).[8] On the other hand, coverage of only one type of facet can be employed to obtain epitaxially connected quantum dots in two dimensional superlattices to increase charge carrier mobility. This is fundamental for highly performing QD devices based on charge transport.[9] It is not straightforward to asses the above questions by means of experimental research. To date the available methods are scarce.[10;11] In addition, the data obtained by experiments can be difficult to interpret.

In this chapter, we describe an NMR method for gaining insight in the ligand distribution on the nanocrystal surface. Spectral hole burning experiments are used to examine the surface chemistry of CdSe and PbSe quantum dots capped with oleate ligands. These oleates are very suitable for this NMR study thanks to their isolated alkene resonance at $\approx 5.6 - 5.7$ ppm. The spectral hole burning experiments can provide a great deal of information about the ligand shell of nanocrystals. On the one hand, the heterogeneity of the oleate alkene resonance is determined. The occurrence of a spectral hole is a sign of heterogeneity of a broad resonance.[2] For QDs, the heterogeneity could originate from a different configuration or orientation of the ligand or a different chemical environment. On the other hand, a spectral hole burning experiment can provide information about the ligand shell structure. When a series of spectral hole burning experiments is performed where the specific waiting time introduced between the saturation and the actual recording of the spectrum is increased, a spectral hole burning recovery can be measured. The recovery of a spectral hole reflects the loss of the irradiation induced transparency. This is caused either by spin-lattice relaxation or by a transfer of saturation to other parts of the resonance. The latter could involve an nOe type of transfer or it could be caused by each molecule slowly sampling a relatively broad configuration - and thus chemical shift - space either because they reorient or move to other locations on the nanocrystal. Importantly, the latter processes leave the overall

intensity of the resonance unchanged, whereas spin-lattice relaxation leads to a recovery of the original resonance intensity. More information on how to distinguish between these two cases is found in section 5.3 below. The NMR experiments are supported by Classical Molecular Dynamics simulations performed by the group of Ivan Infante at VU Amsterdam. The distribution of oleate ligands on the surface of CdSe quantum dots was simulated and subsequently the ligand density of each facet was calculated.

5.2 Experimental

PbSe synthesis. A stock solution of Pb oleate was prepared by loading 3.74 g of PbO (16.8 mmole) and 15.87 mL of oleic acid (50.3 mmole) in a three-neck flask. After flushing the flask with N_2 for 1 hour at 120°C, the temperature was increased to 150°C and the mixture was left to react until a clear, pale-yellow solution was obtained. The still hot solution was diluted with 67.96 mL of diphenyl ether and transferred to a nitrogen-filled glove box. TOPSe was prepared by heating 0.7106 g of Se powder (9 mmole), 9.366 mL of trioctylphosphine (21 mmole) and 87μL of diphenylphosphine (0.5 mmole) to 150°C until the Se powder was completely dissolved. PbSe QDs with an average diameter of 5.7 nm were synthesized by heating 12.3 mL of Pb oleate to 180°C and injecting 9 mL of TOPSe. The temperature was set at 150°C right before injecting the TOPSe. After 60 s, the reaction mixture was quenched with 15 mL of butanol and the synthesized QDs were precipitated by adding 15 mL of acetonitrile to the reaction flask. After centrifugation, the supernatant was discarded and the obtained QDs were washed 2 times by redispersion in toluene, precipitation with acetonitrile and centrifugation. After the final centrifugation, the purified QDs were redispersed in 4 mL of toluene. All procedures were carried out under inert atmosphere to prevent oxidation of the QDs. The size of the obtained QDs can be tuned from 3.5 nm to 8.5 nm by adjusting the injection temperature from 140°C to 210°C, always setting the growth temperature 30°C below the injection temperature. Samples for NIR-UV-VIS absorption measurements were prepared by redispersing 10μL of the purified QD dispersion in 4 mL of tetrachloroethylene.

CdSe/ODESe Synthesis. CdSe quantum dots were synthesized similar to Jasieniak *et al.*[12] In brief, a mixture of cadmium oleate (0.36 mmol), oleic acid (2.16 mmol) and 1-octadecene (total volume = 12mL) was stirred under a nitrogen flow for 30 min at 100°C. The nitrogen flow was stopped, and still under nitrogen, the temperature was raised to 260°C. 3.6mL of a 0.1M ODESe solution (0.36 mmol) was injected and the reaction was

performed at 235°C. To purify the CdSe nanocrystals, equal amounts of toluene, 2-propanol and methanol were added to the synthesis mixture in a 1:1 ratio with respect to the amount of 1-octadecene. The mixture was centrifuged and the palet was redispersed in toluene. In a second and third purification step, the nanocrystals were precipitated and resuspended using methanol and toluene as the non-solvent and the solvent, respectively. For the synthesis work, toluene ($> 99.8\%$), methanol ($> 99.85\%$) and 2-propanol ($> 99.7\%$) were purchased from Fiers; oleic acid (90%) and cadmium oxide (CdO; $> 99.99\%$ metals bases) were purchased from Sigma-Aldrich; selenium (99.999%) and 1-octadecene (tech.) were purchased from Alfa Aesar.

Nuclear Magnetic Resonance Spectroscopy. NMR samples of purified NC dispersions are prepared by evaporation of the toluene with a strong nitrogen flow in the glove box. The resulting dry NCs are dissolved in deuterated toluene-d8 ($99,50\%$ D, purchased at Euriso-top) and transferred to an NMR tube (5 mm). Nuclear Magnetic Resonance (NMR) measurements were recorded on a Bruker Avance III Spectrometer operating at a ^{1}H frequency of 500.13 MHz and equipped with a BBI-Z probe. The sample temperature was set to 298.15 K. Spectral hole burning experiments were recorded with a saturation power level of 60 dB for 5 seconds. The shape of the spectrum obtained after spectral hole burning strongly depends on the settings, where the waiting time between the irradiation and the NMR measurement is a crucial element. Therefore, a first set of measurements was performed to determine the power level. It was varied until a significant spectral hole appeared for all samples. The same saturation power level was used for all experiments. The number of scans was set to 8 for each experiment. To obtain quantitative spectral hole burning spectra, the delay was set to 10s between scans to allow full relaxation of all NMR signals. The spectral hole burning experiment is explained in Section 2.5 of Chapter 2.

Fitting of the exponential decay For each decay, a mono- or bi-exponential funtion (Equation 5.1 and 5.2, respectively) were used, unless specified differently.

$$f(t) = 1 + A\ exp(-k_1 t) \tag{5.1}$$

$$f(t) = 1 + A\ exp(-k_1 t) + B\ exp(-k_2 t) \tag{5.2}$$

Classical Molecular Dynamics Simulations. Classical Molecular Dynamics uses the numerical solution of the Newtonian equations of motion, where macroscopic equilibrium properties are directly retrieved using statistical mechanics. All simulations have been carried out on a non-stoichiometric $Cd_{1012}Se_{911}$ nanocrystal of about 4.0 nm in diameter cleaved

from a bulk zinc-blende structure that exposes the (100), the Cd-rich (111), the Se-rich (111) and the (101) staircase facets. 202 X-type formiate ligands were generated to charge balance the excess of cationic charge of the native $Cd_{1012}Se_{911}$ nanocrystals. The center of mass (COM) of the carboxylate groups of these ligands were randomly placed on the surface of an imaginary sphere of 6 nm of diameter centered in the COM of the nanocrystal. This places the X-type ligands at $\sim$ 1 nm from the surface and loosely pointing at it. All formiates were then substituted by oleates, with the carboxylate groups in the same positions. A relatively long energy minimization of 15000 steps was then performed to eliminate possible overlaps between the organic tails by using the very robust conjugate gradient and line search algorithm implemented in namd. During this energy minimization, the positions of the atoms in the nanocrystal and of the carboxylate groups in the imaginary sphere were constrained, *i.e.* fixed in their initial position. The X-type ligands were then relaxed onto the nanocrystal surface by performing microcanonical or NVE simulations of 15 ns. Relaxations were performed first in vacuum to accelerate ligand approach to the surface. Atomic velocities were initialized to reach a temperature of 500 K, a bit lower than the temperature at which colloidal CdSe nanocrystals are synthesized. In this relaxation step, the integrity of the non-passivated nanocrystal was maintained by restraining Cd and Se atom positions with very stiff harmonic potential using (k=15000 kJ/mol). The fully-passivated QDs were thereafter simulated in dichloromethane. Solvated boxes were 11nm x 11nm x 11nm. Solvent and ligand tails were initially relaxed in the new environment by performing a complete steep descent minimization toward the closest minimum followed by a Molecular Dynamics simulation (Isothermal-isobaric ensemble or NpT) of 1.5 ns at 500 K and 1 atm (Berendsen thermostat and barostat were used). In both passages, the nanocrystal and the carboxylate ligand atoms were restrained in the positions obtained from the previous ligand relaxation step. In the subsequent step, finally all atoms were allowed to completely relax by annealing the temperature from 500 K to 298 K in 20 ns (velocity rescaling thermostat) and maintaining pressure at 1 atm (Parinello-rahman barostat). After the annealing, each system was simulated for additional 20 ns at the final temperature (298 K). The last 17 ns were used for the analyses.

5.3 Background

In the spectral hole burning experiments performed for this work, the irradiation time was standardly set to 5s, which is considerably longer than the relaxation constants of the nanocrystal systems. In addition, saturation can also be transferred from one part of the resonance to another. Hence, irradiation in a spectral hole burning experiment effectively creates a steady state determined by (1) the saturation of the resonance at the irradiated frequency, (2) the transfer of saturation to other frequencies and (3) the loss of saturation by relaxation (Figure 5.1). The balance of these rates determines the obtained resonance intensities.

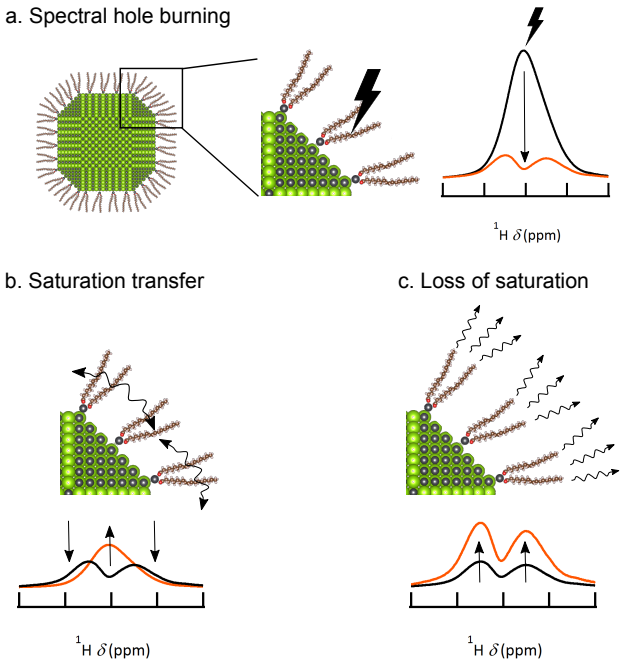

Figure 5.1: A steady state is reached during irradiation where the signal intensity is determined by 3 factors. a) The saturation of the resonance at the irradiated frequency. The original resonance is shown in black, the effect of the spectral hole burning is depicted in orange. b) The transfer of saturation to other frequencies. The original resonance is shown in black, the effect of the saturation transfer is depicted in orange. c) The loss of saturation by spin-lattice relaxation. (Same color code)

There are two main situations to be distinguished when spectral hole burning leads to a spectral hole:

In situation (a), depicted in Figure 5.2 a, there is no saturation transfer. Here a narrow, deep spectral hole is formed and the intensity of the rest of the resonance equals the intensity before irradiation. The shape of the obtained spectra depends on the irradiation power and time (unless it is markedly larger than T1) and the T1 relaxation rate. The size of the hole will depend on the strength of the saturation and the relaxation constants. The recovery of the spectral hole in this case is simple: the intensity at the hole will recover to its intensity before saturation with a single rate constant, equal to 1/T1.

In situation (b), the steady state is determined by the three above-mentioned processes (Figure 5.2 b). Since the saturation is transferred to parts of the resonance that are not irradiated, the intensity will attenuate at those chemical shifts as well. This gives rise to the resonance depicted in Figure 5.2 b, 0s delay: a significant hole is present and the intensity of the complete resonance is much lower than the original resonance intensity. The relaxation of such a system is more complex. When irradiation is stopped, the saturation transfer and the relaxation will both continue until the original situation is reached again. Therefore, the spectral hole disappears more quickly than in situation (a), with a resulting decrease of the intensity at the sides of the resonance. Thereafter, the loss of saturation by spin-lattice relaxation will lead to a recovery of the complete resonance intensity. Hence, the complete resonance will recover with a single rate constant yet the intensity around the spectral hole will recover with a bi-exponential decay.

The presence or absence of the saturation transfer will depend of the degree of solvatation. Close-packed ligands will be able to transfer the saturation more efficiently than ligands on a less dense surface. Note that the two above-mentioned situations can occur at the same time if a resonance is composed of two submanifolds for example. To demonstrate the presence of saturation transfer within the submanifolds within one resonance, the spectral hole burning can be performed at different chemical shifts.

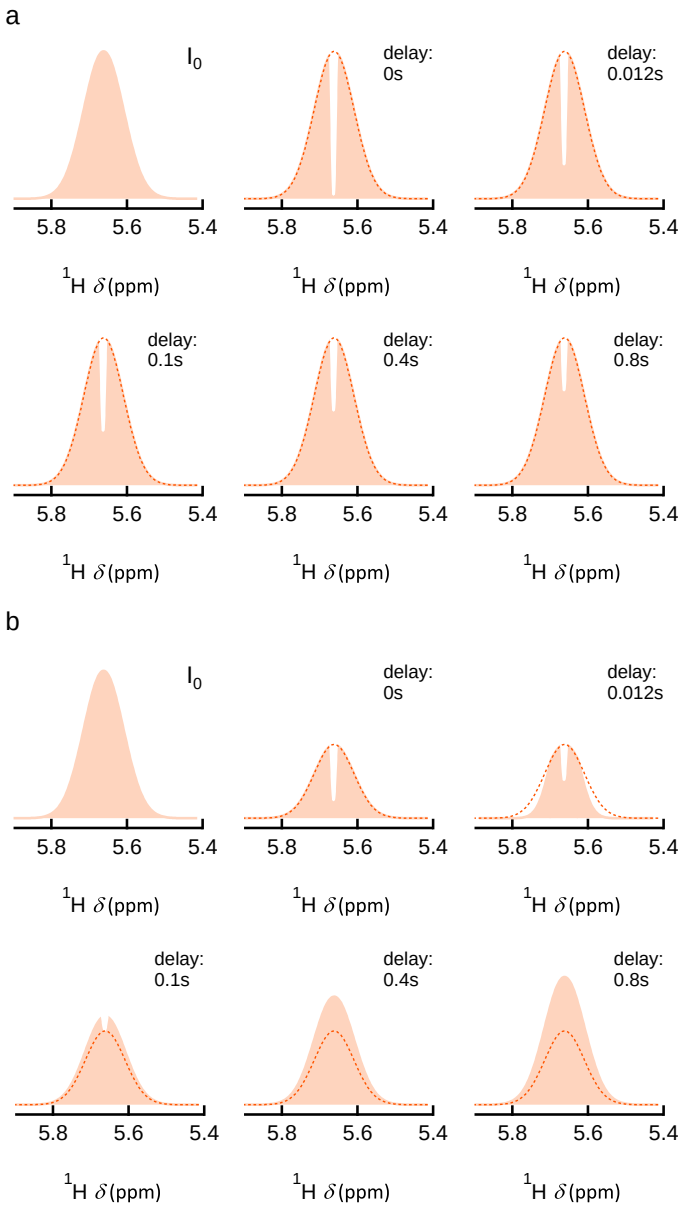

Figure 5.2: Two main situations when spectral hole burning leads to a spectral hole. a) Representation of a situation without saturation transfer. The original resonance, the resonance immediately after spectral hole burning and the recovery are shown. Here a narrow spectral hole is formed. b) Representation of a situation with saturation transfer. Here the spectral hole burning leads to the attenuation of the complete resonance and the presence of a spectral hole.

5.4 Results

5.4.1 Spectral hole burning on oleate ligands

For this study, 3.8 nm CdSe and 3.7 nm PbSe quantum dots were synthesized. Both nanocrystals are capped with oleate ligands, with ligand densities amounting to 3.0 ± 0.2 and 4.2 ± 0.2 ligands/nm^2, respectively. As attested by the 1D ^{1}H NMR spectra, both samples are well purified without free acid and only isopropanol (0.936 and 3.6 ppm) and grease (1.31 and 0.72 ppm) present as impurities, see Figure 5.3.[13] Figure 5.4 represents a series of spectral hole burning experiments where the alkene resonance of oleates bound to (a) PbSe and (b) CdSe was irradiated at different frequencies, as indicated. In all cases, the intensity of the resonance drops inhomogeneously and, especially in the case of CdSe QDs, a spectral hole is formed centered at around the irradiation frequency. We thus conclude that for both PbSe and CdSe QDs, the broadened alkene resonance is, in fact, a heterogeneous manifold composed of different, more narrow resonances.

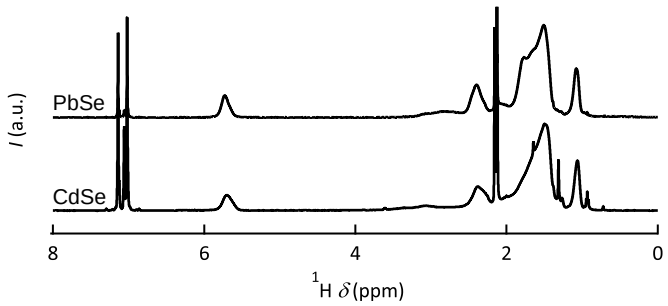

Figure 5.3: The 1D ^{1}H spectrum of PbSe (top) and CdSe (bottom) quantum dots of 3.66 nm and 3.85 nm, respectively. The spectra show clear broad features of the oleates, indicating that no free ligands are present. The bottom spectrum contains some impurities: isopropanol (0.936 and 3.6 ppm) and grease (1.31 and 0.72 ppm)

5.4.2 PbSe QDs: spectral hole burning recovery

To analyze ligand heterogeneity in more detail, we monitored the relaxation of spectral holes burned at different positions in the alkene resonance. This can be done by recording a series of hole burning spectra with a progressively increased delay time between the irradiation and the actual recording of the NMR spectrum, see Section 2.5 of Chapter 2 for more information. Focusing

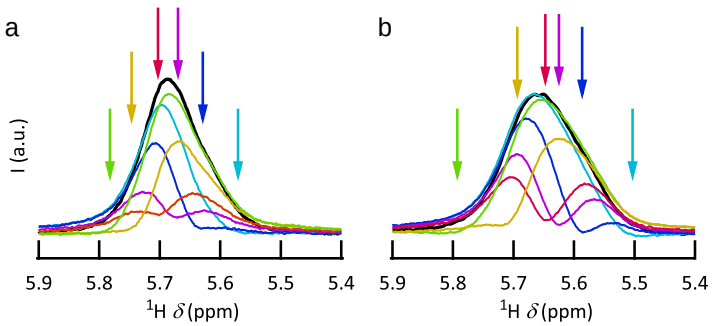

Figure 5.4: A series of spectral hole burning spectra of a) PbSe and b) CdSe quantum dots ($3,66$ nm and $3,85$ nm, respectively). In each measurement a different part of the resonance was irradiated, indicated with an arrow in the same color as the spectrum. The black spectrum represents measurement without spectral hole burning

first on the case of PbSe QDs, Figure 5.5a shows such a recovery series taken after irradiating the central part of the alkene resonance. Initially, one sees that this results in a spectral hole at the irradiated frequency and a marked reduction of the signal intensity across the entire resonance. During the recovery, the spectral hole rapidly disappears – which concurs with a decrease in intensity at the downfield and upfield side of the resonance – and the entire resonance regains its original intensity. Note that the latter process is rather fast as compared to the 5 s of irradiation used in these experiments; after 0.4 s, the resonance has regained already 77% of its original intensity.

Figure 5.5b represents total resonance intensity and the resonance intensity integrated over a narrow frequency range around the minimum of the spectral hole (see blue band in Figure 5.5a), both normalized to the fully relaxed intensities. The total intensity recovery can be described by a single exponential with a rate constant of $k_1 = 2.95 \pm 0.1$ s^{-1}. The function used for the fitting is $f(t) = 1 + A\ exp(-k_1 t)$. In this case, the value of A is -0.69. The resonance intensity at the center of the spectral hole, on the other hand, exhibits a more involved recovery where an initially rapid recovery tends asymptotically the the overall intensity relaxation. A fit to a double exponential ($f(t) = 1 + A\ exp(-k_1 t) + B\ exp(-k_2 t)$) yields accordingly a first rate constant comparable to the overall relaxation rate and a second, considerably faster component $k_2 = 56 \pm 6$ s^{-1}. Here A and B are -0.76 and -0.14, respectively. Looking at Figure 5.5a, the latter clearly characterizes the disappearance of the spectral hole.

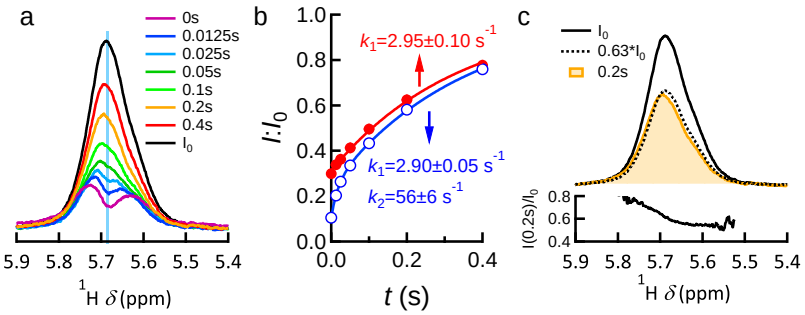

Figure 5.5: a) A series of spectral hole burning spectra of PbSe quantum dots. In each measurement the waiting time introduced between the saturation and the actual recording of the spectrum is increased. b) Recovery of (red) the total resonance intensity and (blue) the resonance intensity around the bottom of the burned spectral hole as a function of the waiting time. The latter region is highlighted in (a) of this figure. c) Top: original spectrum (black) and spectrum with waiting time 0.2s (filled yellow) of (a), together with an overlay with the recovered resonance rescaled with an average rescaling factor (dashed black) as indicated. Bottom: the ratio between the intensity of the spectrum after 0.2s and the original spectrum I_0 as function of the chemical shift.

In addition, it can be seen that after the initial rapid disappearance of the spectral hole, the relaxing resonances do not attain a shape idential to the fully relaxed resonance. This is shown more clearly in Figure 5.5c, where the resonance recorded using an 0.2 s delay is compared to the best fitting rescaled resonance. The impression that the rescaled resonance underestimates the downfield side and overestimates the upfield side of the recovering resonance is compared by the inset in Figure 5.5c, which represents the ratio $I(0.2)/I_0$. Whereas this ratio tends towards 0.8 at the downfield side of the resonance, it only reaches about 0.5 at the upfield side. This suggests a more complicated picture of the resonance heterogeneity, where on the one hand the original spectral hole is erased quite rapidly while on the other hand, both sides of the resonance do not equilibrate during the recovery.

We further addressed this point by irradiating the alkene resonance both at the downfield and the upfield side and recording the ensuing resonance recovery. As shown in Figure 5.6a, irradiating the alkene resonance at the upfield side (5.62 ppm) whipes out the entire downfield side of the resonance. Again, the overall resonance intensity exhibits a single exponential recovery with a rate constant estimated at $k_1 = 2.34 \pm 0.13\ \mathrm{s}^{-1}$, whereas the recovery

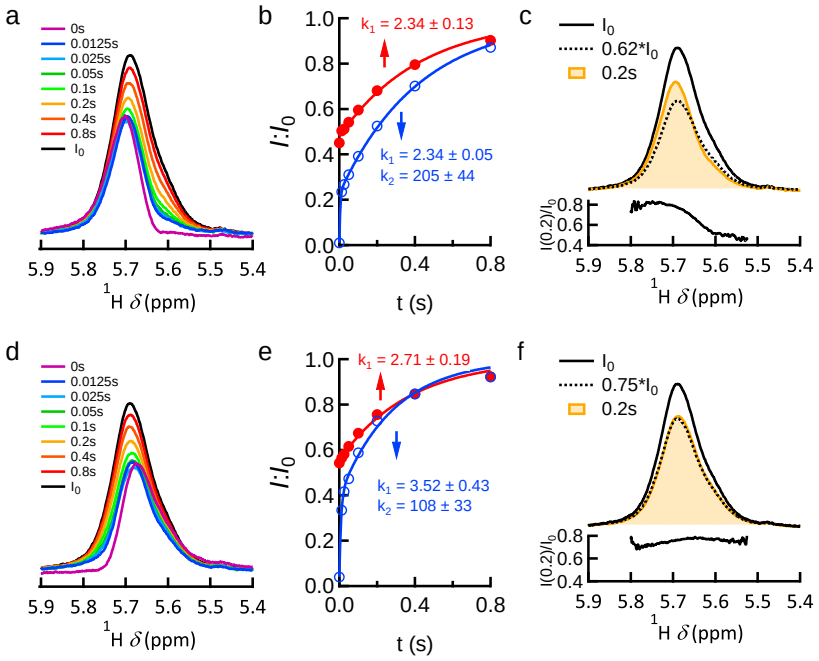

Figure 5.6: a) A series of spectral hole burning spectra of PbSe quantum dots at the upfield side of the resonance (5.62 ppm). In each measurement the waiting time introduced between the saturation and the actual recording of the spectrum is increased. b) Recovery of the total resonance intensity (red) and the resonance intensity around the bottom of the burned spectral hole (blue) as a function of the waiting time. c) Top: original spectrum (black) and spectrum with waiting time 0.2s (filled yellow) of (a), together with an overlay with the recovered resonance rescaled with an average rescaling factor (dashed black) as indicated. Bottom: the ratio between the intensity of the spectrum after 0.2s and the original spectrum I_0 as function of the chemical shift. d-f) same as (a-c), for spectral hole burning at the downfield side of the resonance. (5.76 ppm)

in a narrow spectral window around 5.62 ppm features an additional fast component with an ill-defined rate of $k_2 = 205 \pm 44$ s^{-1}. Coefficients A and B were -0.77 and -0.21, respectively. Note that rapid recovery at the upfield side concurs with an initial intensity drop at the downfield side of the resonance, a transfer required to have an overall single-exponential intensity buildup. Again, the shape of the recovering resonance does not match a rescaled version of the relaxed resonance, where a plot of the $I(0.2)/I_0$ ratio

shows that deviations are now even more pronounced, see Figure 5.6c.

A similar picture emerges from spectral hole burning at the downfield side (5.76 ppm) of the resonance, see Figure 5.6d-f. Again, the downfield side of the resonance is all but completely wiped out immediately after irradation. The overall intensity recovery follows a single exponential, yet focusing on the frequency range around 5.76 ppm shows that this also contains a rapid transfer of saturation from that region to almost the entire resonance. Moreover, also the recovering resonance does not coincide with a rescaled version of the relaxed resonance. The difference is, however, less pronounced in this case and reversed with respect to the previous examples with a lower intensity at the upfield and a higher at the downfield side.

5.4.3 CdSe QDs: spectral hole burning recovery

Figure 5.7a represents a spectral hole burning recovery series measured after irradiating the center of the alkene resonance of CdSe QDs. Similar to the case of PbSe, irradiation leads to a spectral hole in the resonance – though it seems more pronounced – and the upfield and downfield sides of the resonance have a reduced intensity even if these regions were not targeted. In addition, the overall resonance intensity can be fitted to $f(t) = 1 + A\ exp(-k_1 t)$ and recovers with a single rate constant of $2.24 \pm 0.16\ s^{-1}$, with a coefficient A of -0.54 (see Figure 5.7b). The intensity around the irradiated frequency, on the other hand, exhibits the characteristic double exponential recovery ($f(t) = 1 + A\ exp(-k_1 t) + B\ exp(-k_2 t)$) with an additional rapid relaxation rate of $\approx 70\ s^{-1}$. Again, this rapid relaxation concurs with a transfer of saturation from the irradiated region to the downfield and upfield side of the resonance.

Opposite from the hole burning recovery with PbSe QDs, however, the spectral hole does not disappear after the fast, initial saturation transfer. It rather changes shape and vanishes with the overall intensity recovery. We therefore followed an alternative approach to monitor the recovery of the spectral hole, where we subtract from a relaxed spectrum rescaled so as to match the intensity at the upfield and downfield side of the hole burning spectrum, each hole burning spectrum, see Figure 5.7c. For this fitting, we used the following fit function:

$$f(t) = A\ exp(-k_1 t) + B\ exp(-k_2 t) \tag{5.3}$$

This confirms the picture of an initially fast recovery, followed by a slow recovery whose rate coincides with that of the overall intensity ($k_1 = 3.41, k_2 = 263.34, A = 0.17 and B = 0.38$). Note that the slowly recovering part of the

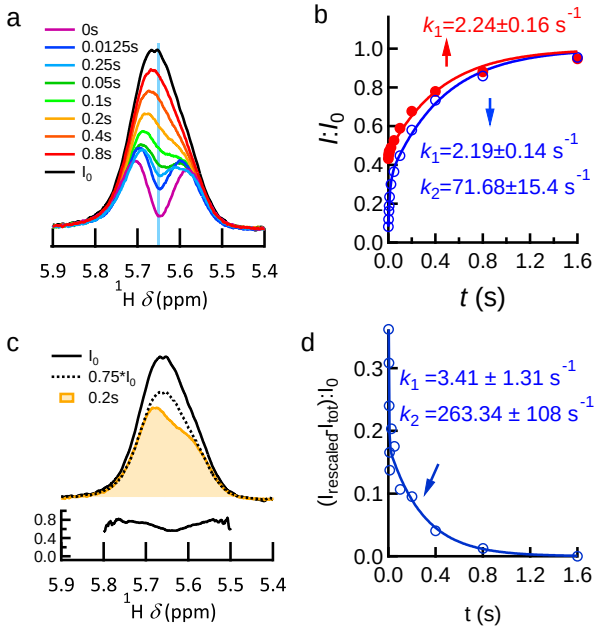

Figure 5.7: a) A series of spectral hole burning spectra of CdSe quantum dots. In each measurement the waiting time introduced between the saturation and the actual recording of the spectrum is increased. b) Recovery of (red) the total resonance intensity and (blue) the resonance intensity around the bottom of the burned spectral hole as a function of the waiting time. The latter region is highlighted in (a) of this figure. c) Original spectrum (black) and spectrum with waiting time 0.2s (filled yellow) of (a), together with (dashed black) an overlay with the recovered resonance rescaled as indicated to overlap with the both sides of the alkene resonance at 0.2 s waiting time. d) For each spectral hole burning spectrum, the original spectrum was rescaled to overlap with both sides of the spectral hole burning spectrum as demonstrated in (c). The difference between the intensity of each matched spectrum and each spectral hole burning spectrum, normalized to the intensity of the original spectrum, is plotted as function of waiting time.

spectral hole has an initial intensity amount to $\approx 20\%$ of the original resonance intensity.

Irradiating the alkene resonance of CdSe QDs at its downfield side (5.72 ppm) yields a picture similar to what was obtained with PbSe QDs. As shown in Figures 5.8a-c, the entire downfield side becomes largely trans-

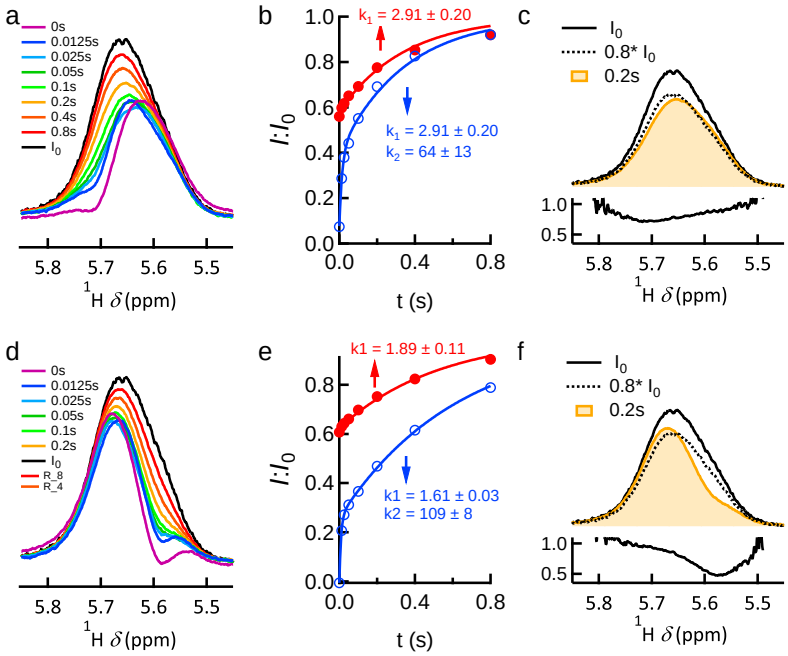

Figure 5.8: a) A series of spectral hole burning spectra of CdSe quantum dots at the downfield side of the resonance (5.72 ppm). In each measurement the waiting time introduced between the saturation and the actual recording of the spectrum is increased. b) Recovery of the total resonance intensity (red) and the resonance intensity around the bottom of the burned spectral hole (blue) as a function of the waiting time. c) Original spectrum (blank) and spectrum with waiting time 0.2s (filled yellow) of (a), together with (dashed black) an overlay with the recovered resonance rescaled with an average rescaling factor as indicated. d-f) same as (a-c), for spectral hole burning at the upfield side of the resonance (5.58 ppm).

parent and the overall single-exponential recovery hides a more complex bi-exponential dynamics with rate constants similar to what was found with PbSe. In addition, the recovering resonance does not match a rescaled version of the relaxed resonance, with a markedly lower (higher) intensity at the downfield (upfield) side, respectively.

A totally different picture, on the other hand, ensues after irradiating the upfield side of the resonance (5.58 ppm), see Figures 5.8d-f. As shown in Figure 5.8d, rather than effacing the intensity over the entire upfield side, a marked spectral hole is now burned in the spectrum. Again, this hole ex-

hibits a double exponential decay ($f(t) = 1 + A\ exp(-k_1 t) + B\ exp(-k_2 t)$) involving a rapid redistribution of saturation and a slower intensity recovery ($k_1 = 1.61, k_2 = 109, A = -0.74 and B = -0.26$). However, the initial redistribution does not erase the spectral hole as can be seen from a comparison between the recovering spectrum after an 0.2 s delay and a rescaled fully relaxed spectrum (Figure 5.8f). This is further confirmed by considering the ratio $I(0.2)/I_0$, which now shows a dip rather than an asymptote at the upfield side. Hence, notwithstanding the similarities with the hole burning recovery of oleate ligands bound to PbSe QDs, it appears that oleate ligands bound to CdSe feature a more complex heterogeneity where two pools of ligands coexist with markedly different hole burning recovery characteristics.

5.5 Discussion

5.5.1 PbSe QDs

The set of spectral hole burning experiments on the alkene resonance of oleate ligands bound to PbSe QDs leads to three main conclusions:

1. The alkene resonance is heterogeneously broadened. Irradiating different parts of the spectrum leads to differently shaped resonances, often featuring a spectral hole and never simply proportional to the relaxed resonance.

2. The intensity of the complete intensity is much lower than the initial resonance intensity, indicating a saturation transfer within the resonance.

3. Hole burning recovery involves two time constants, a first reflecting the transfer of saturation from the irradiated region to the entire resonance and a second involving the overall loss of irradiation-induced saturation.

4. The rapid initial saturation transfer does not yield a recovering resonance that is a merely rescaled version of the relaxed resonance and its shape depends on what part of the original resonance was irradiated.

The finding that the broad alkene resonance is heterogeneous is hardly a surprise. Similar observations were made in the case of trioctylphosphine oxide bound to InP [2] and underlying variation in resonance frequencies can easily result from the diversity of chemical environments experienced by the oleate ligands. The orientation of the ligand, for example, might change the

chemical shift of the resonance as could the local ligand density and the extent of solvent penetration in the ligand shell.

The transfer of saturation from the irradiated region to the entire resonance is more intriguing. It shows that the entire heterogeneous resonance is not composed of separate ligands each exhibiting a particular, well-defined chemical shift. Saturation transfer could result from, for example, nOe contacts that lead to spin diffusion between neighboring ligands or it could be caused by each molecule sampling a relatively broad configuration space, thus changing its chemical shift with time. In view of the measurements shown here, the latter explanation is the more likely as nOe contacts should also transfer saturation to different resonances, a process not preserving the resonance intensity. Note that both the saturation transfer and the overall recovery are considerably shorter than the 5s irradiation time. Hence, irradiation in a spectral hole burning experiment effectively creates a steady state determined by (1) the saturation of the resonance at the irradiated frequency, (2) the transfer of saturation to other frequencies and (3) the loss of saturation (Figure 5.1). The balance of these rates determines the obtained resonance intensities.

Since an exchange of saturation takes place within the manifold of resonance frequencies, the relaxed resonance should represent a situation of thermal (dynamic) equilibrium. The rapid saturation transfer out of the irradiated region to the downfield and upfield sides of the resonance should therefore result in a resonance that takes, once the spectral hole has disappeared, the same shape as the recovered resonance. This, however, is not the case. We typically find that the downfield and the upfield side of the resonance have a shape that indeed fits the recovered resonance, yet with a different proportionality constant. Hence, whereas saturation can be transferred from the irradiated region to either side of the resonance - and leads to a thermal equilibrium at both sides - this implies that no saturation is transferred and no equilibration takes place between the downfield and the upfield part of the resonance. The recovery of the alkene resonance after spectral hole burning thus leaves us with the apparently contradictory outcome that saturation is rapidly transferred from the spectral hole to either the downfield or the upfield side of the resonance, whereas both sides do not thermalize.

Such behavior does not fit an interpretation of the alkene resonance as reflecting a single heterogeneous ligand manifold. It can, however, occur when the manifold of alkene resonances consists of (at least) two separate parts that (1) are both heterogeneously broadened, (2) overlap both with the irradiated frequency and (3) exhibit rapid thermalization (saturation transfer) within each manifold yet slow or no thermalization between them

(see Figure 5.9).

Considering the morphology of a colloidal nanocrystal, a most straightforward interpretation of such non-interacting submanifolds within a single alkene resonance are clearly ligands adsorbed to different crystal facets (Figure 5.9). Here, slightly different ligand densities - and thus different solvent penetration - could shift the average resonance frequency. Their spatial separation will inhibit saturation transfer from one facet to another. In this respect, the fact that the PbSe/oleate spectral hole disappears with a single rate constant only indicates that saturation transfer within both manifolds is highly similar and could be seen as characteristic of a collection of ligands on densely packed facets.

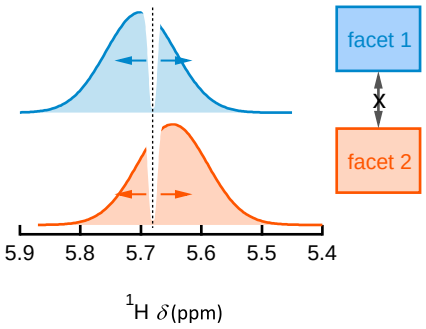

Figure 5.9: Representation of two heterogeneously broadened subresonances making up a single heterogeneously broadened resonance. One is slightly more shifted than the other one. If no saturation transfer is possible between both subsets, redistribution can occur within each subset but not between the subsets.

To invigorate this picture, we used it as a basis to simulate the shape of the alkene resonance during hole burning recovery at a moment where thermalization is complete but relaxation is not. We assumed that the entire alkene resonance is composed of two, slightly shifted Gaussian resonances, each representing one of the ligand submanifolds. Finally, we estimated the intensity loss of either Gaussian after irradiation and recovery as proportional to its intensity at the irradiation frequency. To decide the width and relative intensity of each Gaussian, we focused on the experimental ratio $I(0.2)/I_0$ obtained after irradiating different parts of the resonance. First, when the alkene resonance is irradiated at its maximum intensity, we observed that the upfield side is bleached more than the downfield side. This indicates that this intensity maximum is closer to the maximum of the up-

field submanifold then to the downfield submanifold. This enhanced bleaching of the upfield side is, obviously, more pronounced when irradiating the upfield side, yet it is only just reversed upon irradiating the downfield side. This suggests that the upfield submanifold is more intense and considerably broader than the downfield manifold.

We accordingly used a combination of resonances shown in Figure 5.10a, where (black, dotted pattern) two heterogeneously broadened subresonances make up a (black line) single heterogeneously broadened resonance. Following upfield, center and downfield irradiation, we calculated the (red line) recovering resonance and compared it with the fully relaxed resonance. As anticipated, we find that irradiating the upfield side leads to a more pronounced bleach at the upfield side, see Figure 5.10b. By the choice of the two resonances, this enhanced bleach of the upfield side persists - although less pronounced - upon irradiating the resonance at its maximum and is only reversed when irradiating the downfield side. Admittedly, the actual alkene resonance of PbSe-bound oleate ligands has a shape different from a mere sum of two Gaussians. Nevertheless, this set of simulated hole burning spectra indicates that the experimental observations can indeed be understood by conceiving the resonance as the sum of two ligand submanifolds that show rapid intermanifold yet no or slow intramanifold thermalization. Moreover, it appears that one of them is more intense and broader than the other. Possibly, this reflects differences in surface area of the crystal facets terminating PbSe QDs that we tentatively linked to the separate ligand submanifolds.

5.5.2 CdSe QDs

Similar to oleate ligands bound to PbSe QDs, we find that the alkene resonance of CdSe-bound oleate ligands is heterogeneously broadened. Moreover, the intensity of the complete resonance is lower than the original resonance, indicating saturation transfer. The recovery of this resonance after spectral hole burning features a similar combination of a rapid saturation transfer followed by a slower relaxation as for the PbSe case. On the other hand, spectral holes resulting from irradiating the center or the upfield side of the resonance are more pronounced and persist after the initial redistribution of saturation across the resonance. This indicates that the shell of oleate ligands around CdSe QDs is (1) composed of non-interacting submanifolds that (2) may be structurally different from that around PbSe QDs.

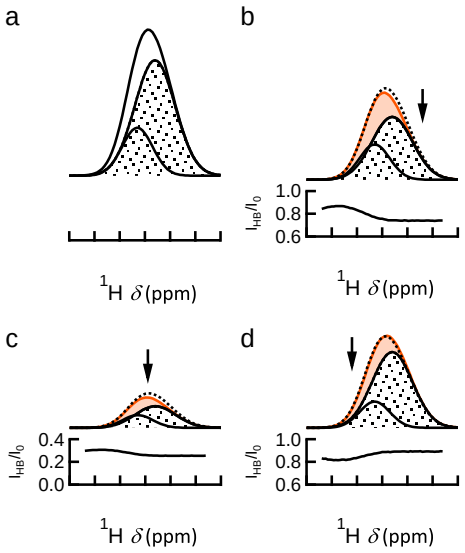

Figure 5.10: a) Representation of two heterogeneously broadened subresonances (black, dotted pattern) making up a single heterogeneously broadened resonance (black). One is slightly more shifted than the other one. b-d) Top: Simulation of irradiation at the upfield side (b), center (c) and downfield side of the resonance (d). The subresonances after simulation (black, dotted pattern), their sum (red, filled) and the rescaled original resonance (black, dotted line) are shown. Bottom: ratio between the total resonance after spectral hole burning I_{HB} and the original resonance for spectral hole burning I_0

For CdSe- and PbSe-bound oleate ligands, the spectral shape and recovery of the alkene resonance after irradiating its downfield side is highly similar. Initially, almost the entire downfield side of the resonance is wiped out, whereas it matches a rescaled version of the relaxed resonance after the rapid saturation transfer. Spectral hole burning at the center and upfield side of the resonance, however, displays a different behavior. Here, a spectral hole persists during the recovery of the resonance intensity and its spectral position moves together with the irradiation frequency. This suggests that here, oleate resonances are addressed that (1) have a relatively narrow spectral footprint and (2) are not involved in a rapid saturation transfer or thermalization, neither with the resonance manifold dominating the downfield side, nor among each other.

We summarize these conclusions in the description of the alkene resonance as shown in Figure 5.11. It combines a broad, rapidly thermalizing yet heterogeneous resonance depicted in red with a set of more narrow, homogeneous resonances at the upfield side in blue. The first accounts for the rapid saturation transfer observed during all hole burning recovery series and the relatively featureless spectral hole burned at the downfield side. The second set is responsible for the persistent, slowly recovering spectral hole burned in the center or upfield side of the resonance. In line with our conclusions in the case of PbSe QDs, the broad resonance might again be attributed to ligands bound to a densely packed crystal facet. Attributing this second is more speculative. Given the lower overall ligand density and the more narrow resonance lines, this may reflect oleate ligands on sparsely packed facets where heterogeneity and saturation transfer is reduced by better solvation by solvent molecules.

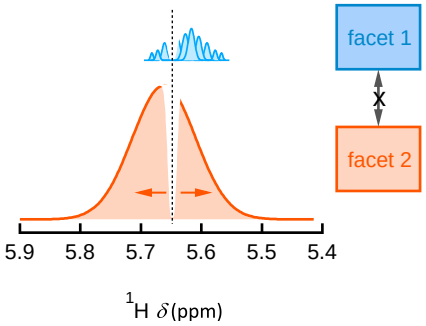

Figure 5.11: Representation of two heterogeneously broadened subresonances making up a single heterogeneously broadened resonance. One subset is significantly smaller and located more upfield than the other one. If no saturation transfer is possible between both subsets, redistribution can occur within each subset but not between the subsets.

5.6 Confirmation by Classical Molecular Dynamics simulations

To support the tentative interpretation of the hole burning and hole burning recovery experiments on CdSe-bound oleate ligands, we analyzed the oleate capping of CdSe QDs using classical molecular dynamics simulations in collaboration with dr. Ivan Infante (VU Amsterdam). All simulations have been carried out on a non-stoichiometric $Cd_{1012}Se_{911}$ nanocrystal of

about 4.0 nm in diameter cleaved from a bulk zinc-blende structure that exposes the (100), the Cd-rich (111), the Se-rich (111) and the (101) staircase facets. Dichloromethane was used as a solvent and 202 oleate ligands were introduced which leads to an overall ligand density of 3.43 ligands/nm^2, in close agreement with experimental ligand densities. All simulation details can be found in the experimental section.

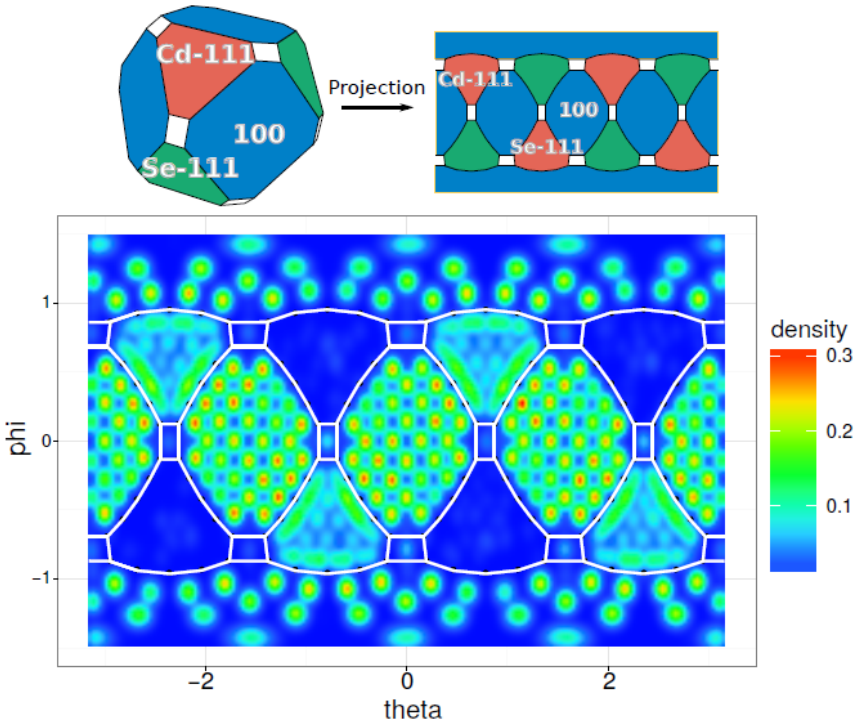

Figure 5.12: Projection of the surface of the simulated CdSe QD. The ligand density is plotted in function of the position on the QD surface.

As shown in Figure 5.12, these simulations show that oleate ligands have the highest affinity towards the (100) facets, where they all orient in the same direction. The Cd-rich (111) facets bind ligands mostly at their edges, yet they also support more mobile ligands on their center. Little ligands, if any, on the other hand bind to the Se-rich (111) facets. Overall, this leads to facet-dependent ligand densities as summarized in Table 5.1. It follows that the overall ligand density of $3.0 - 3.5\,\mathrm{nm}^{-2}$ reflects an area-weighted average involving facets with hugely divergent ligand densities.

Given the ligand density of $4.0\,\mathrm{nm}^{-2}$ or more in the case of PbSe QDs, one can argue that the densely packed oleate ligands on CdSe(100) account for the similarities between CdSe and PbSe in spectral hole burning and hole burning recovery. Hence, these ligands could account for the broad, rapidly equilibrating part of the alkene resonance represented in red in Figure 5.11. The interpretation of the homogeneous resonances at the upfield side of the resonance is less straightforward. They could either correspond to oleate ligands bound to the edges or the center of the Cd-rich(111) facets or both. In either case, surface curvature or lower ligand densities can indeed enhance the solvation of ligands, thus creating the range of more homogeneous chemical environments that is needed to explain the experimental observations.

Table 5.1: Ligand densities for different facets, obtained during the simulations of CdSe with oleate ligands

Facet	ligand density (ligands/nm^2)	standard deviation
(100)	4.99	0.06
Cd-rich (111)	3.11	0.16
Se-rich (111)	0.1	0.09
Total	3.43	

5.7 Conclusion

Spectral hole burning experiments were performed on 3.8 nm CdSe and 3.7 nm PbSe QDs capped with oleate ligands. Both samples exhibit a significant spectral hole after spectral hole burning targeting the alkene resonance, indicating that oleate ligands have heterogeneously broadened resonances when bound to the QD surface. This could be a consequence of a variation in chemical environment experienced by the oleate ligands. A spectral hole burning recovery study shows the recovery of the region around the spectral hole and the complete resonance. For PbSe QDs, the total intensity recovers with a mono-exponential decay. The intensity at the spectral hole on the other hand, shows a bi-exponential decay. The fast component corresponds to the disappearance of the spectral hole, the slower one is similar to the decay of the complete resonance. In addition,

the upfield and downfield side of the resonance both have the shape of the fully recovered spectrum, however with different proportionality constants. This means that saturation can be transferred from the center to either sides of the resonance but no saturation is transferred between the sides. Hence, the resonance consists of two highly similar submanifolds. These two submanifolds could reflect ligands bound to different nanocrystal facets that have comparable ligand densities. The high ligand density of PbSe could explain the efficient saturation transfer on each facet.

For CdSe QDs, the spectral hole burning results in a more distinct initial spectral hole. The recovery exhibits a mono-exponential decay as well. It is similar but somewhat slower than for PbSe. During the recovery the spectral hole seems to change shape. Moreover, after the initial rapid recovery, the spectral hole has not completely disappeared. This indicates that, opposite from PbSe/oleate, CdSe/oleate features two frequency submanifolds with a markedly different saturation relaxation behavior. Spectral hole burning at the upfield and downfield side of the resonance show that one submanifold spreads across the complete chemical shift region of the resonance and the other is located at the upfield side. In line with our conclusions in the case of PbSe QDs and the simulations, the broad resonance could be attributed to ligands bound to a densely packed crystal facet ((100) facet). Attributing the second is more speculative. It could either correspond to oleate ligands bound to the edges or the center of the Cd-rich(111) facets or both. In either case, surface curvature or lower ligand densities can indeed enhance the solvation of ligands, thus creating the range of more homogeneous chemical environments that is needed to explain the experimental observations.

We have shown an alternative way to asses the distribution of ligands on the QD surface by combining spectral hole burning experiments with classical Molecular Dynamics simulations.

References

[1] Iwan Moreels, Karel Lambert, Dries Smeets, David De Muynck, Tom Nollet, José C. Martins, Frank Vanhaecke, Andre Vantomme, Christophe Delerue, Guy Allan, and Zeger Hens. *Size-Dependent Optical Properties of Colloidal PbS Quantum Dots.* ACS Nano, 3(10):3023–3030, 2009.

[2] Zeger Hens, Iwan Moreels, and José C. Martins. *In situ ^{1}H NMR study on the triOctylphosphine oxide capping of colloidal InP nanocrystals.* Chemphyschem, 6(12):2578–2584, 2005.

[3] Haitao Liu, Jonathan S. Owen, and A. Paul Alivisatos. *Mechanistic study of precursor evolution in colloidal group II-VI semiconductor nanocrystal synthesis.* Journal of the American Chemical Society, 129(2):305–312, 2007.

[4] Bernd Fritzinger, Iwan Moreels, Petra Lommens, Rolf Koole, Zeger Hens, and José C. Martins. *In Situ Observation of Rapid Ligand Exchange in Colloidal Nanocrystal Suspensions Using Transfer NOE Nuclear Magnetic Resonance Spectroscopy.* Journal of the American Chemical Society, 131(8):3024–3032, 2009.

[5] Raquel Gomes, Antti Hassinen, Agnieszka Szczygiel, Qiang Zhao, Andre Vantomme, Jose C. Martins, and Zeger Hens. *Binding of Phosphonic Acids to CdSe Quantum Dots: A Solution NMR Study.* Journal of physical chemistry Letters, 2(3):145–152, 2011.

[6] Antti Hassinen, Raquel Gomes, Kim De Nolf, Qiang Zhao, Andre Vantomme, Jose C. Martins, and Zeger Hens. *Surface Chemistry of CdTe Quantum Dots Synthesized in Mixtures of Phosphonic Acids and Amines: Formation of a Mixed Ligand Shell.* Journal of physical chemistry C, 117(27):13936–13943, 2013.

[7] Antti Hassinen, Iwan Moreels, Celso de Mello Donega, Jose C. Martins, and Zeger Hens. *Nuclear Magnetic Resonance Spectroscopy Demonstrating Dynamic Stabilization of CdSe Quantum Dots by Alkylamines.* Journal of physical chemistry Letters, 1(17):2577–2581, 2010.

[8] Antti Hassinen, Iwan Moreels, Kim De Nolf, Philippe F. Smet, Jose C. Martins, and Zeger Hens. *Short-Chain Alcohols Strip X-Type Ligands and Quench the Luminescence of PbSe and CdSe Quantum Dots, Acetonitrile Does Not.* Journal of the American Chemical Society, 134(51):20705–20712, 2012.

[9] Willem Walravens, Jonathan De Roo, Emile Drijvers, Stephanie ten Brinck, Eduardo Solano, Jolien Dendooven, Christophe Detavernier, Ivan Infante, and Zeger Hens. *Chemically Triggered Formation of Two-Dimensional Epitaxial Quantum Dot Superlattices.* ACS Nano, 10(7):6861–6870, 2016.

[10] Alicia M Jackson, Ying Hu, Paulo J. Silva, , and Francesco Stellacci. *From Homoligand- to Mixed-Ligand- Monolayer-Protected Metal Nanoparticles: A Scanning Tunneling Microscopy Investigation.* Journal of the American Chemical Society, 128(34):11135–11149, 2006.

[11] Xiang Liu, Miao Yu, Hyewon Kim, Marta Mameli, and Francesco Stellacci. *Determination of monolayer-protected gold nanoparticle ligand-shell morphology using NMR.* Nature Communications, 3, 2012.

[12] Jacek Jasieniak, Craig Bullen, Joel van Embden, and Paul Mulvaney. *Phosphine-Free Synthesis of CdSe Nanocrystals.* Journal of Physical Cemistry B, 109(44):20665–20668, 2005.

[13] Gregory R. Fulmer, Alexander J. M. Miller, Nathaniel H. Sherden, Hugo E. Gottlieb, Abraham Nudelman, Brian M. Stoltz, John E. Bercaw, and Karen I. Goldberg. *NMR Chemical Shifts of Trace Impurities: Common Laboratory Solvents, Organics, and Gases in Deuterated Solvents Relevant to the Organometallic Chemist.* Organometallics, 29(9):2176–2179, 2010.

6

Two-Component Colloidal Quantum Dot Ligand Shells

This last chapter addresses the surface chemistry of CdSe/oleate nanocrystals when a carboxylic acid is added to the dispersion. Is there a preferential binding of one or the other carboxylic acid? Does the chain length or shape of the acid influence the ligand shell composition?

6.1 Introduction

Colloidal nanocrystals (NCs) are terminated by an organic capping or ligand shell.[1;2] Typical ligands such as carboxylic acids, thiols, amines or phosphonic acids feature a functional headgroup and a hydrocarbon chain and they are used in nanocrystal synthesis as coordinating agents to dissolve metal precursors. Adhering by their headgroup to the surface of growing nanocrystals and exposing their tail to the surroundings, they act as steric stabilizers that provide colloidal stability to the reaction mixture. Ligand concentration and chain length proved, moreover, most useful reaction variables to tune the nanocrystal size during synthesis[3;4] and it was found that they can promote anisotropic growth,[5;6] most likely by preferentially adhering

to specific crystal facets. Furthermore, tightly bound ligands make dried nanocrystals a tractable powder that can be readily redispersed in appropriate solvents, a practical advantage that facilitated the ongoing proliferation of colloidal nanocrystals in applications that cover fields as diverse as lighting and displays,[7] photovoltaics,[8] photodetection,[9] sensing[10] and catalysis.[11]

For most nanocrystal applications, a proper surface termination has proven essential and breakthroughs in surface functionalization have often led to significant improvements in nanocrystal processing and nanocrystal-based device performance or made possible new nanocrystal applications. Using *entropic ligands* such as 2-hexyldecanoic acid (HDA) to maximize the intramolecular entropic effects, leads to outstanding processability.[12] Replacing the original organic ligands of semiconductor nanocrystals or quantum dots by small organic or inorganic moieties, for example, makes for high mobility QD films[13] and enables the QD workfunction to be tuned,[14] two aspects that are now widely explored in QD photodetectors[9] or solar cells.[15] Again for colloidal QDs, various studies have addressed the relation between the ligand surface coverage and the photoluminescence quantum yield, which underlies their use in lighting, displays and solar concentrators. Gold nanocrystals, on the other hand, were turned into colorimetric sensors when functionalized with ligands exposing chelating or complexing groups to the surroundings that can coordinate specific analytes and thus cause an aggregation-induced color change.[10]

Nanocrystal ligand shells have been compared to self-assembled monolayers (SAM) on flat surfaces, where alkanethiols on gold stand out as one of the most-studied SAM model systems and a widely used colloidal nanocrystal/ligand combination.[16–18] The way SAMs organize themselves on solid surfaces is generally described in terms of the combined effect of headgroup-substrate and chain-chain interaction. In this respect, the above examples make clear that either in view of ligand exchange or to assess the interplay between ligand binding and nanocrystal properties, nanocrystal surface chemistry tends to focus more on headgroup-substrate interactions than on chain-chain interactions. However, already in the case of two-component SAMs containing molecules with identical headgroups yet slightly dissimilar chains, ligand-ligand interactions can cause phase separation into nanometer scale molecular domains,[19] a size commensurate with that of a nanocrystal surface facet.

Gold nanocrystals capped by synthesis with a binary ligand shell of octanethiol and mercaptopropionic indeed show phase segragation,[20] where different molecules can group in ripples or Janus-like domains.[21] Interestingly, such patchy or Janus-like ligand shells can help directing nanocrystal

self-assembly or tuning nanocrystal properties.[22] Extending such results to colloidal quantum dots is, however, not straightforward since several elements may further affect ligand packing in a two-component ligand shell. First, especially quantum dots made of binary metal sulfides or selenides such as CdSe, PbS and PbSe, are terminated by facets with distinctly different composition and concomitantly different headgroup-substrate interactions. Second, a delicate interplay exists in such nanocrystals between the surface composition and the ligand density, where excess surface metal cations are charge balanced by a fixed equivalence of so-called X-type ligands such as carboxylates or phosphonates.[23;24] For one thing, this restricts newly added X-type ligands to replacing existing ligands in a fixed equivalence rather than adding to the ligand shell, processes which are both possible in the case of gold nanocrystals exposed to thiols.[25]

Here, we propose a combined experimental and theoretical study on two-component ligand shells of colloidal quantum dots made by ligand exchange. Taking oleate-capped CdSe quantum dots as a model system,[23] we first show by nuclear magnetic resonance (NMR) spectroscopy that exposure to other fatty acids results in a one-for-one exchange that leaves the net ligand/excess cadmium balance unchanged. In the case of single chain saturated carboxylic acids, this results in a progressive exchange where a two-component ligand shells are formed that have the same composition as the reaction mixture. With a branched carboxylic acid, on the other hand, only part of the original ligands can be exchanged, regardless of the concentration of the branched acid. Describing the quantum-dot surface using a two dimensional lattice model, we attribute this to a combination of a tit-for-tat exchange reaction and a difference in chain volume. Whereas such a model cannot distinguish a randomly distributed from a phase-separated two-component ligand shell, Classical Molecular Dynamics simulations support an interpretation where the particular surface chemistry of CdSe QDs restricts the adsorption of branched carboxylic acids to the edges of crystal facets. This indicates that in the case of quantum dots of binary semiconductors, two-component ligand shells can phase separate by the joined effect of facet-specific adsorption, ligand-ligand interaction and ligand densities imposed by the surface excess of metal cations.

6.2 Experimental

CdSe/ODESe Synthesis. CdSe quantum dots were synthesized similar to Jasieniak *et al.*[26] In brief, a mixture of cadmium oleate (0.36 mmol), oleic acid (2.16 mmol) and 1-octadecene (total volume = 12mL) were stirred un-

der a nitrogen flow for 30 min at 100°C. The nitrogen flow was stopped, and still under nitrogen, the temperature was raised to 260°C. 3.6mL of a 0.1M ODESe solution (0.36 mmol) was injected and the reaction was performed at 235°C. To purify the CdSe nanocrystals, equal amounts of toluene, 2-propanol and methanol were added to the synthesis mixture in a 1:1 ratio with respect to the amount of 1-octadecene. the mixture was centrifuged and the pellet was redispersed in toluene. In a second and third purification step, the nanocrystals were precipitated and resuspended using methanol and toluene as the non-solvent and the solvent, respectively. For the synthesis work, toluene (> 99.8%), methanol (> 99.85%) and 2-propanol (> 99.7%) were purchased from Fiers; oleic acid (90%) and cadmium oxide (CdO; > 99.99% metals bases) were purchased from Sigma-Aldrich; selenium (99.999%) and 1-octadecene (tech.) were purchased from Alfa Aesar.

Nuclear Magnetic Resonance Spectroscopy. NMR samples of purified nanocrystal (NC) dispersions are prepared by evaporation of the solvent with a strong nitrogen flow in the glove box. The resulting dry NCs are dispersed in deuterated toluene-d8 (99, 50% D, purchased at Euriso-top) or deuterated 1, 2-dichlorobenzene-d4 (99, 50% D, purchased at Euriso-top) and transferred to an NMR tube (5 mm). High resolution Nuclear Magnetic Resonance (NMR) measurements were recorded on a Bruker Avance III Spectrometer operating at a ^{1}H frequency of 500.13 MHz and equipped with a BBI-Z probe or on a Bruker Avance II Spectrometer operating at a ^{1}H frequency of 500.13 MHz and equipped with a TXI-Z probe (channels are ^{1}H, ^{1}3C, ^{3}1P). The sample temperature was set to 298.15, 333.15, 348.15 or 393.15 K. Quantitative ^{1}H spectra were recorded with a 20 s delay between scans to allow full relaxation of all NMR signals. The quantification was done by using the Digital ERETIC method. All resonances were corrected prior to integration by subtracting a background from the measured intensity.

Classical Molecular Dynamics Simulations Classical Molecular Dynamics uses the numerical solution of the Newtonian equations of motion, where macroscopic equilibrium properties are directly retrieved using statistical mechanics. All simulations have been carried out on a non-stoichiometric $Cd_{1012}Se_{911}$ nanocrystal of about 4.0 nm in diameter cleaved from a bulk zinc-blende structure that exposes the (100), the Cd-rich (111), the Se-rich (111) and the (101) staircase facets. 202 X-type formiate ligands were generated to charge balance the excess of cationic charge of the native $Cd_{1012}Se_{911}$ nanocrystals. The COM of the carboxylate groups of these ligands were randomly placed on the surface of an imaginary sphere of 6 nm

of diameter centered in the COM of the nanocrystal. This places the X-type ligands at $\sim$ 1 nm from the surface and loosely pointing at it. All formiates were then substituted by either oleate ions or 2-hexyldecanoate ions, depending on the fraction of bound 2-hexyldecanoates, $x_{\mathrm{HDAc,b}}$, chosen with the carboxylates groups in the same positions. A relatively long energy minimization of 15000 steps was then performed to eliminate possible overlaps between the organic tails by using the very robust conjugate gradient and line search algorithm implemented in namd. During this energy minimization, the positions of the atoms in the nanocrystal and of the carboxylate groups in the imaginary sphere were constrained, *i.e.* fixed in their initial position. The X-type ligands were then relaxed onto the nanocrystal surface by performing microcanonical or NVE simulations of 15 ns for each $x_{\mathrm{HDAc,b}}$. Relaxations were performed first in vacuum to accelerate ligand approach to the surface. Atomic velocities were initialized to reach a temperature of 500 K, a bit lower than the temperature at which colloidal CdSe nanocrystal are synthesized. In this relaxation step, the integrity of the non-passivated nanocrystal was maintained by restraining Cd and Se atom positions with very stiff harmonic potential using (k=15000 kJ/mol). The fully-passivated QDs were thereafter simulated in dichloromethane. Solvated boxes were 11nm x 11nm x 11nm. Solvent and ligand tails were initially relaxed in the new environment by performing a complete steep descent minimization toward the closest minimum followed by a Molecular Dynamics simulation (Isothermal-isobaric ensemble or NpT) of 1.5 ns at 500 K and 1 atm (Berendsen thermostat and barostat were used). In both passages, the nanocrystal and the carboxylate ligand atoms were restrained in the positions obtained from the previous ligand relaxation step. In the subsequent step, finally all atoms were allowed to completely relax by annealing the temperature from 500 K to 298 K in 20 ns (velocity rescaling thermostat) and maintaining pressure at 1 atm (Parinello-rahman barostat). After the annealing, each system was simulated for additional 20 ns at the final temperature (298 K). The last 17 ns were used for the analyses.

6.3 Results and Discussion

6.3.1 Carboxylic Acid Exchange Stoichiometry

In this study, we use CdSe quantum dots (QDs) synthesized following Jasieniak *et al.* from cadmium oleate and elemental selenium in a reaction where oleic acid is the sole ligand.[26] The method typically yields ≈ 3.5 nm CdSe QDs stabilized by oleates,[23] as attested by the ^{1}H NMR spectrum of a purified dispersion in 1,2-dichlorobenzene-d_4 represented in Figure 6.1a.

Similar to previously published work,[23] the spectrum features the broadened resonances that characterize bound oleate, where especially the alkene resonance at ≈ 5.65 ppm stands out as it shows no overlap with any other resonance in the dispersion. As the spectrum is acquired under quantitative conditions, the integrated intensity of this resonance indicated by the shaded area in the inset of Figure 6.1a is directly proportional to the amount of bound ligands in the dispersion. From this number, we calculate a ligand density of 3.32 ± 0.31 nm^{-2} for the example shown.

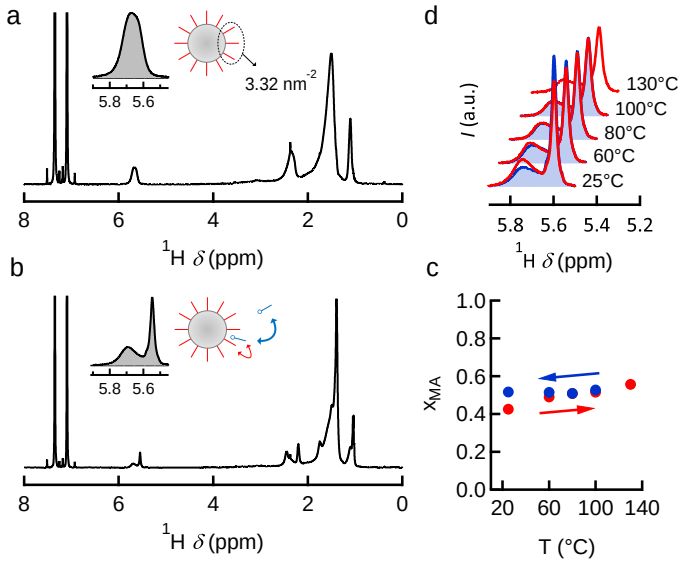

Figure 6.1: a) 1D ^{1}H NMR spectrum of oleate capped CdSe QDs synthesized according to ref. 26 in 1,2-dichlorobenzene-d_4. A zoom on the resonance of the alkene protons at ≈5.65 ppm is shown in the inset. b) 1D ^{1}H NMR spectrum of oleate capped CdSe nanocrystals after addition of 1 equiv of myristic acid in 1,2-dichlorobenzene-d_4. Again, the alkene resonance is shown in the inset, together with a cartoon representation of the resulting exchange between bound oleate and free oleic acid. c) 1D ^{1}H NMR spectrum of alkene resonance after myristic acid addition (oleic acid:myristic acid 1:1) when sweeping the temperature from 25 to 130°C (red) and back to 60°C (blue, filled). (d) The fraction of bound myristic acid in function of temperature, when sweeping the temperature from 25 to 130°C (red) and back to 60°C (blue), showing a dynamic equilibrium at temperatures above 60°C.

Upon addition of a primary saturated carboxylic acid - myristic acid (MAc) in this case - each of the broadened resonances acquire a second, sharper resonance at their upfield side, see Figure 6.1b. This is clearly visible in the inset in Figure 6.1b, which shows a zoom on the alkene region. This additional resonance has been amply discussed before in the literature.[23] As shown by the cartoon inset in Figure 6.1b, it is a population-averaged resonance, assigned to free oleic acid in rapid exchange with oleic acid physisorbed to the CdSe QDs (blue arrow). Moreover, also the bound oleate making up the broad resonance was shown to exchange, albeit slowly, with this pool of free oleic acid (red arrow). Figure 6.1c indicates that an increase in temperature from 25 to 130°C changes the shape and intensity of both resonances. These changes, however, show no hysteresis when sweeping the temperature from 60 to 130°C and back. We thus conclude that the addition of myristic acid induces the release of oleic acid from the CdSe QDs and establishes a dynamic equilibrium between bound and free ligands for temperatures exceeding ≈ 60°C.

Carboxylic acids bind to CdSe QDs as carboxylates in a charge-balanced 2:1 ratio with respect to the excess Cd cations on the CdSe surface. Given the need of colloidal QDs in apolar solvents to preserve charge neutrality,[27] one thus expects the release of oleic acid upon addition of myristic acid to concur with the binding of myristate to the CdSe surface. Writing the core CdSe QD as [CdSe], a carboxylic acid in general as HX and a surface cadmium carboxylate as (CdX_2), the presumed exchange reaction can then be written as:

$$[\mathrm{CdSe}](\mathrm{CdX_2}) + \mathrm{HX'} \rightleftharpoons [\mathrm{CdSe}](\mathrm{CdXX'}) + \mathrm{HX} \tag{6.1}$$

Whereas such exchange reactions have already been verified for the replacement of carboxylates by alkyl phosphonates on CdSe QDs,[24], we titrated as-synthesized CdSe QDs using 1-undecenoic acid to explicitly establish the exchange equilibrium expressed by Equation 6.1 for carboxylate/carboxylate replacement. Similar to oleic acid, 1-undecenoic acid has alkene resonances that show little overlap with other resonances. This enables the concentration of all bound and free ligands to be determined from the same, quantitative ^{1}H spectrum from the integrated intensity of the respective resonances.

Figure 6.2a shows four examples of 1D ^{1}H NMR spectra recorded during a titration of oleate capped CdSe QDs with 1-undecenoic acid. Starting from the bound-oleate-only spectrum of the as-synthesized QDs, the spectra clearly show the decrease in intensity of the bound oleate (OAc_b)

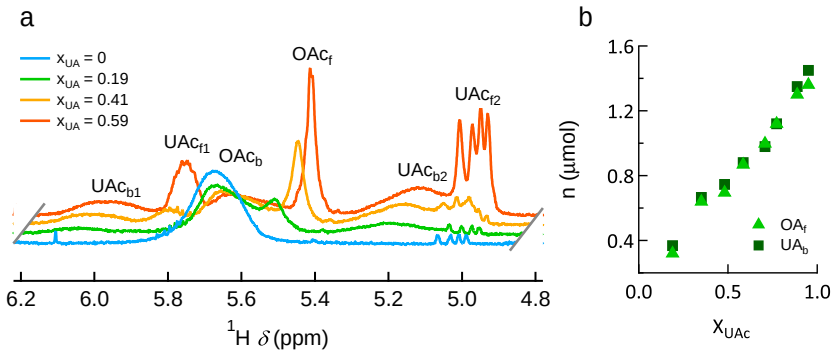

Figure 6.2: a) 1D ^{1}H NMR spectra of a dispersion of oleate capped CdSe QDs after addition of different amounts of 1-undecenoic acid, yielding overall 1-undecenoic mole fractions as indicated. OAc and UAc indicate resonances pertaining to oleic and 1-undecenoic acid, respectively, whereas the subscript *b* and *f* refere to pools of bound and free ligands. b) The one-for-one exchange between two carboxylic acids is verified by evaluating the amount of bound 1-undecenate and the amount of free oleic acid in function of the titration steps.

resonance and the concomitant increase of the free oleic acid (OAc_f) and bound 1-undecenoate (UAc_b) resonances when the overall mole fraction of 1-undecenoic acid is raised. Figure 6.2b represents the amount of UAc_b and the amount of OAc_f as a function of the fraction of 1-undecenoic acid, calculated from all spectra recorded during the titration. Clearly, both species are present in a 1:1 ratio, which confirms the presumed stoichiometry of the carboxylate/carboxylate replacement as expressed by Equation 6.1.

6.3.2 Oleic Acid / Primary Carboxylic Acid Replacement

Figure 6.3a shows a zoom on the alkene region of the NMR spectrum of originally oleate-capped CdSe QDs during successive steps of a titration with myristic acid at 60°C. Upon increasing the overall mole fraction x_{MAc} from 0 to 0.95, one sees that the upfield resonance of rapidly exchanging oleic acid gains intensity at the expense of the broad resonance of bound oleate. At the same time, the exchanging oleic acid alkene resonance develops the fine structure typical for free oleic acid, indicative of the free oleic acid increasingly dominating the averaged resonance. Similar observations are made upon titrating with other primary carboxylic acids - generally written

as XAc - such as nonanoic acid and 1-undecenoic acid (see Figure 6.4).

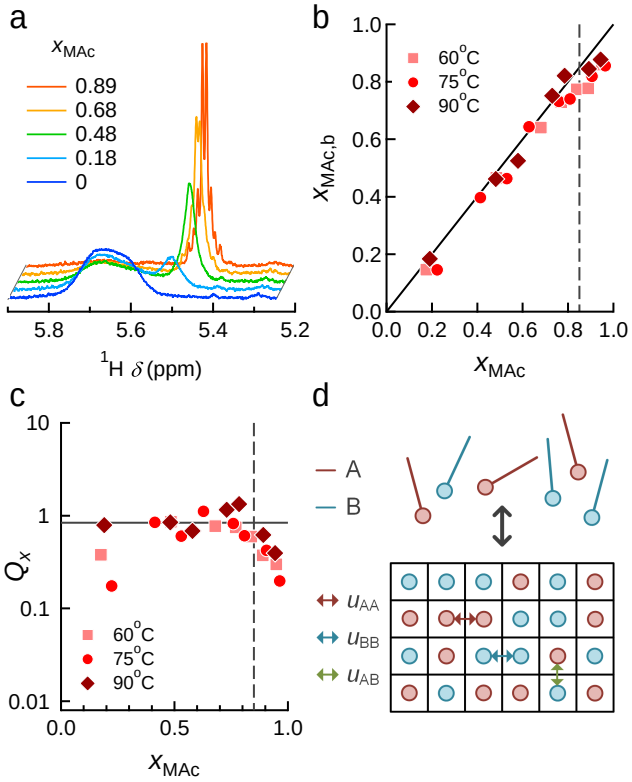

Figure 6.3: a) 1D ^{1}H NMR spectra of a dispersion of oleate capped CdSe QDs after addition of different amounts of myristic acid at $60°C$ b) The fraction of bound myristate to bound carboxylate $x_{\mathrm{MAc,b}}$ as function of the fraction of myristic acid with respect to the total amount of acid x_{MAc} at $60, 75$ and $90°C$ c) The equilibrium constant for each step in the titration at $60, 75$ and $90°C$ is plotted in function of the fraction of myristic acid x_{MAc}. d) Lattice model representation of a binary shell containing bound oleate and bound myristate.

Since any release of oleic acid is matched by the equivalent adsorption of myristate, the NMR spectra as shown in Figure 6.3a can be used to determine the composition of the ligand shell. To do so, we use the amount of bound oleate ($n_{\mathrm{OAc,b}}$) and released oleic acid ($n_{\mathrm{OAc,f}}$) as determined from the NMR spectra to calculate the mole fraction $x_{\mathrm{XAc,b}}$ of the newly bound carboxylate:

$$x_{\mathrm{XAc,b}} = \frac{n_{\mathrm{XAc,b}}}{n_{\mathrm{OAc,b}} + n_{\mathrm{XAc,b}}} = \frac{n_{\mathrm{OAc,f}}}{n_{\mathrm{OAc,b}} + n_{\mathrm{OAc,f}}} \tag{6.2}$$

In Figure 6.3b, $x_{\mathrm{XAc,b}}$ thus determined during myristic acid titrations at 3 different temperatures, *i.e.*, 60, 75 and 90°C, is plotted as a function of the overall mole fraction x_{MAc} of the added myristic acid. Overall, it follows that $x_{\mathrm{MAc,b}}$ is almost identical to x_{MAc}, meaning that the composition of the ligand shell mimics the overall composition of the dispersion under these conditions. Moreover, no pronounced trend as a function of temperature can be discerned. Only at the highest mole fraction of myristic acid ($x_{\mathrm{MAc}} > 0.85$), it appears that the ligand shell is somewhat enriched in oleate as compared to the overall composition of the mixture. This, however, could also reflect remaining kinetic limitations to the exchange reaction, in particular if oleate exhibits a distribution of adsorption enthalpies where the most strongly bound ligands remain bound to the nanocrystals. Titrations with nonanoic and 1-undecenoic acid at 60°C yield essentially the same picture (see Figure 6.4).

For the oleate/carboxylate exchange given by Equation 6.1, the mole fractions of the different bound and free species can be used to calculate a reaction quotient Q_x, defined as:

$$Q_x = \frac{x_{\mathrm{XAc,b}} \times x_{\mathrm{OAc,f}}}{x_{\mathrm{XAc,f}} \times x_{\mathrm{OAc,b}}} = \frac{n_{\mathrm{OAc,f}}^2}{n_{\mathrm{OAc,b}} \times (n_{\mathrm{MAc}} - n_{\mathrm{OAc,f}})} \tag{6.3}$$

Here, in particular the second equality enables us to calculate Q_x from the experimental data. Except for two outliers, Figure 6.3c demonstrates that the thus determined reaction quotient is largely constant at $Q_x = 0.84 \pm 0.65$ when $x_{\mathrm{MAc}} < 0.85$. This implies that mole fractions make for proper activities for both dissolved carboxylic acids and bound carboxylates. For the former, this is no surprise as the mixture can be considered as ideal-dilute at the given concentrations. In the case of the bound carboxylates, however, it indicates that the capping can be seen as an ideal mixture of two carboxylates where the activity essentially stems from the entropy of mixing.

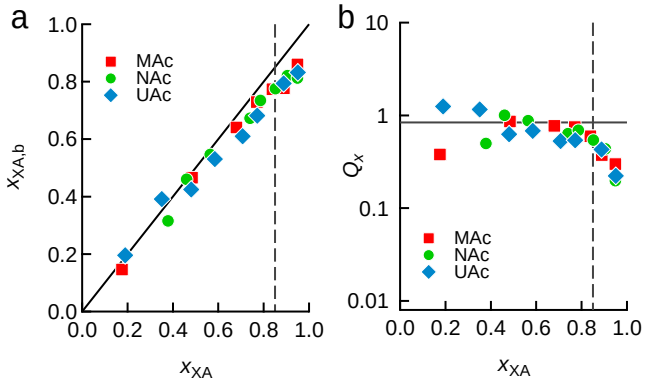

Figure 6.4: a) The fraction of bound primary acid to bound carboxylate $x_{\mathrm{XAc,b}}$ as function of the fraction of primary acid with respect to the total amount of acid x_{XAc} for myristic acid (red), nonanoic acid (green) and 1-undecenoic acid (blue) b) The equilibrium constant for each step in the titration with myristic acid (red), nonanoic acid (green) and 1-undecenoic acid (blue) is plotted in function of the fraction of primary acid x_{XAc}.

Using a lattice model representation of a binary ligand shell containing bound oleate and bound myristate as shown in Figure 6.3d, this suggests that the oleate-myristate nearest neighbor interaction (indicated as u_{AB} in Figure 6.3d) equals the average of the oleate-oleate and myristate-myristate nearest neighbor interaction. Indeed, if such conditions apply, the chemical potential of either of the bound carboxylates can be written as $\mu_{\mathrm{XAc,b}} = \mu^{\circ}_{\mathrm{XAc,b}} + RT \ln x_{\mathrm{XAc,b}}$, where the standard state refers to the respective one-component ligand shell. Such an expression immediately accounts for the mole fractions of the bound species appearing in the reaction quotient when the exchange reaction is seen as the 1-on-1 replacement of bound oleate by bound myristate:

$$\mathrm{OAc}_b + \mathrm{MAc}_f \rightleftharpoons \mathrm{MAc}_b + \mathrm{OAc}_f \tag{6.4}$$

Interpreting the average value of Q_x as the equilibrium constant of the exchange reaction expressed by Equation 6.1 yields a standard exchange free energy $\Delta_{ex}G^{\circ}$ of $0.5\,\mathrm{kJ\,mol^{-1}}$ at 60°C. Since the average of Q_x shows little temperature dependence, this all but vanishing $\Delta_{ex}G^{\circ}$ results from a combination of close to zero exchange enthalpy and exchange entropy. Under such conditions, the composition of the ligand shell will match the overall mole fraction of both carboxylic acids in the dispersion - corresponding to a maximized entropy of mixing - since the exchange reaction involves no net

change in ligand-solvent and ligand-ligand interaction energy.

6.3.3 Oleic Acid / Branched Carboxylic Acid Replacement

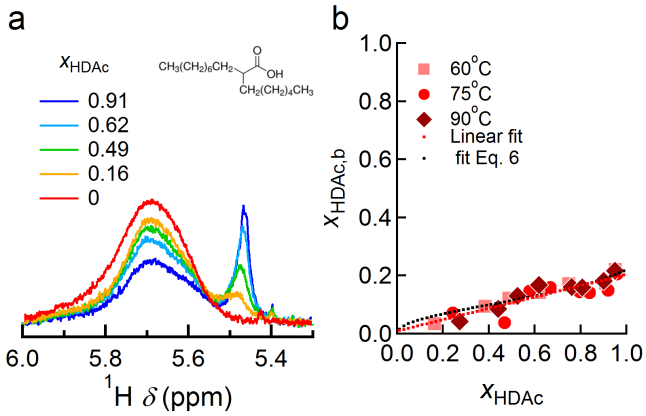

Figure 6.5: a) 1D ^{1}H NMR spectra of a dispersion of oleate capped CdSe QDs after addition of different amounts of 2-hexyldecanoic acid at $60°C$, yielding overall 2-hexyldecanoic mole fractions as indicated. b) The exchange between a linear and a branched carboxylic acid is verified by evaluating the amount of bound 2-hexyldecanoate $x_{\mathrm{HDAc,b}}$ in function of the amount of 2-hexyldecanoic acid x_{HDAc} at $60, 75$ and $90°C$. In addition, the best fit of the experimental data to a linear function (red dots) and Equation 6.6 is shown as well (black dots).

Since two-component ligand shells consisting of oleate and a second primary carboxylate behave as almost ideal mixtures, we extended this study to titrations of as-synthesized oleate-capped CdSe QDs with 2-hexyldecanoic acid (HDAc). This is a commercially available branched carboxylic acid (see Figure 6.5a), such that steric hindrance may affect its distribution over the ligand shell. 2-Hexyldecanoic acid is referred to as an *entropic ligand* by Yang *et. al.* since it maximizes the intramolecular entropic effects, leading to outstanding processability.[12] Upon addition of 2-hexyldecanoic acid, the development of a relatively sharp and shifted resonance upfield from the alkene resonance of bound oleate again attests the exchange between oleic acid and 2-hexyldecanoic acid according to Equation 6.1. In this case, however, a considerable fraction of oleate remains bound even if the overall mole fraction of 2-hexyldecanoic acid is raised to 0.95. More precisely,

Figure 6.5b indicates that the mole fraction of bound 2-hexyldecanoate in the ligand shell levels off at $x_{\mathrm{HDAc,b}} \approx 0.2$, in strong contrast to what was found for primary carboxylic acids.

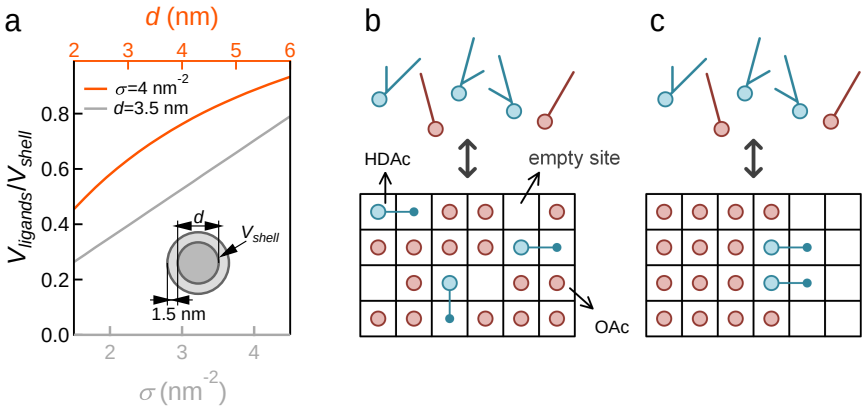

Figure 6.6: a) The fraction of the volume occupied by oleate ligands and the volume available in the ligand shell is plotted in function of the diameter of spheres with a ligand coverage of $\sigma = 4nm^{-2}$ (blue) and in function of the ligand coverage for spheres with ($d = 3.5nm$). b) lattice model representation of a binary shell with a random mixture of free lattice sites and sites occupied by bound oleate and bound 2-hexyldecanoate. c) lattice model representation of a binary shell with free lattice sites at the edges only.

Given the 1-for-1 exchange between carboxylic acids (Equation 6.1), the exchange of a primary for a branched carboxylic acid will raise the volume occupied by the alkyl chains in the ligand shells. In this respect, steric hindrance may cap the amount of 2-hexyldecanoate that can be accommodated in the ligand shell. Indeed, a straightforward calculation assuming a ligand molar volumes characteristic of oleic acid, indicates that the volume of the bound ligands can amount to $50-70\%$ of the volume available in the ligand shell for 3.5 nm spheres with a ligand coverage σ of $3-4\,\mathrm{nm}^{-2}$, see Figure 6.6a. Hence, it is well possible that the limited accessible volume in the ligand shell imposes an upper limit on the oleic acid/2-hexyldecanoic acid exchange.

Different approaches can be put forward to account for the remaining free volume in the ligand shell in a lattice model description of the QD surface. A first involves describing the surface of the original, oleate-capped QDs as a random mixture of lattice sites occupied by oleate ligands and unoccupied

sites (see Figure 6.6b), the latter reflecting the remaining available space in the ligand shell. Whereas the exchange of oleate for a primary carboxylate will leave the number of unoccupied sites unchanged, this will be different if oleate is replaced by a branched carboxylate like 2-hexyldecanoate. Assuming that bound 2-hexyldecanoate occupies 2 lattice sites, we can than rewrite the oleic acid/2-hexyldecanoic acid exchange as a reaction in which bound oleate and a free site are exchanged for bound 2-hexyldecanoate (Equation 6.5). In this equation, the free lattice site is represented by ◯.

$$\mathrm{OAc}_b + \mathrm{HDAc}_f + \bigcirc \rightleftharpoons \mathrm{HDAc}_b + \mathrm{OAc}_f \tag{6.5}$$

If we continue to use mole fractions for activities, the exchange equilibrium expressed by Equation 6.5 can be turned into a relation between the mole fractions of bound and total 2-hexyldecanoic acid (see Appendix 6.A):

$$x_{\mathrm{HDAc,b}} = \frac{-K' x_{\mathrm{HDAc}} - \sqrt{K'^2 x_{\mathrm{HDAc}}^2 + 4\Delta K' x_{\mathrm{HDAc}}(1 - x_{\mathrm{HDAc}})}}{2(1 - x_{\mathrm{HDAc}})} \tag{6.6}$$

Here, K' is the equilibrium constant and Δ is the density of originally empty lattice sites. A fit of the experimental data to Equation 6.6 has been added to Figure 6.5b, where the density of originally empty lattice sites is used as an adjustable fitting parameter. As anticipated, the lattice model can account for the partial exchange in the limit $x_{\mathrm{HDAc}} \to 1$, where a best fit is obtained when initially 22% of the lattice sites are unoccupied. The estimates summarized in Figure 6.6a, however indicate that 50% of the ligand shell volume should be available at a ligand coverage of $3.0\,\mathrm{nm}^{-2}$ for a 3.5 nm QD. As this implies that full coverage by 2-hexyldecanoate should still be possible, a limiting value of $x_{\mathrm{HDAc,b}} = 0.2$ seems rather low.

An alternative interpretation of the restricted oleic acid/2-hexyldecanoic acid exchange starts from the idea that the typical ligand coverage of $3.0 - 3.5\,\mathrm{nm}^{-2}$ reflects an average of over densely packed facets and facets that hardly bind any ligand. Looking at cadmium oleate as the actual binding moiety, this is not an unreasonable conjecture given the facet dependent coordination number of surface selenium atoms. The (100) surface, for example, features 2-coordinated surface selenium atoms that offer two bonds for each cadmium oleate ligand while the Se(111) surface is composed of 3-coordinated surface selenium atoms to which cadmium oleate can be expected to bind more weakly. This is confirmed by the Classical Molecular Dynamics simulations which were discussed in Section 5.6 of Chapter 5. In this picture, the combination of steric hindrance on the densely packed facets and weak binding to the free facets may limit the oleic acid/2-hexyldecanoic

acid exchange to the edges of the densely packed facets (see Figure 6.6c). Assuming ideal mixture behavior at these accessible surface sites, $x_{\mathrm{HDAc,b}}$ will then increase proportionally with x_{HDAc}, where the limiting value at $x_{\mathrm{HDAc}} = 1$ again reflects the fraction of accessible sites. Clearly, the experimental dataset does not enable us to distinguish between such a linear dependence of $x_{\mathrm{HDAc,b}}$ on x_{HDAc} and the more involved variation predicted by Equation 6.6.

6.3.4 Classical Molecular Dynamics Simulations

To understand why branched ligands like 2-hexyldecanoate only replace a small fraction of native oleate ligands as revealed in the above section, Classical Molecular Dynamics simulations were performed by the group of Ivan Infante at the VU of Amsterdam. All simulations have been carried out on a non-stoichiometric $Cd_{1012}Se_{911}$ nanocrystal of about 4.0 nm in diameter cleaved from a bulk zinc-blende structure that exposes the (100), the Cd-rich (111), the Se-rich (111) and the (101) staircase facets. Simulations have been performed for the following fraction of bound 2-hexyldecanoates at the NC surface, $x_{\mathrm{HDAc,b}}$: 1, 0.75, 0.5, 0.25, 0.16, 0, where the range extremes are homogeneous shells (2-hexyldecanoate and oleate, respectively) and the remaining are heterogeneous shells with different proportions of 2-hexyldecanoate and oleate. All simulation details can be found in the experimental section.

First of all, complete coverage of the nanocrystal by only 2-hexyldecanoate ($x_{\mathrm{HDAc,b}} = 1$) is sterically allowed. In contrast to the oleate ligand shell discussed in Chapter 5, the 2-hexyldecanoate now take different positions on the QD surface. The ligand shell is less packed and 2-hexyldecanoate could also bind to Se-rich (111) facets more often than oleates, stabilizing structural defects characterized by Cd atoms that have diffused towards the surface. Figure 6.7a shows the simulations for $x_{\mathrm{HDAc,b}} = 0, 0.5$ and 1, where oleates are shown in grey and 2-hexyldecanoates in pink. The following features have been constantly found in the simulations at room temperature: 1) oleate ions mostly occupy (100) facets, creating very compact, almost pure sub-domains, 2) sub-domains of mixed composition (oleate/2-hexyldecanoate) are usually found on the Cd-(111) facets, 3) 2-hexyldecanoate ions are the main ligands found at the edges and on the Se-(111) facets. These features are clearly visible in Figure 6.7b, where the distribution of the ligands on the different facets is shown for $x_{\mathrm{HDAc,b}} = 0.5$. This implies that the lattice model shown in Figure 6.6c will be is most suited for the representation of the surface. Hence, $x_{\mathrm{HDAc,b}}$ will increase proportionally with x_{HDAc}, where the limiting value at $x_{\mathrm{HDAc}} = 1$ again

reflects the fraction of accessible sites. Phase separation appears as being favored both enthalpically, due to better intermolecular interactions, and entropically, because of the greater mobility of oleate in the homogeneous phase. All results provided by simulations strongly suggest that the experimental low exchange rates of branched ligands (2-hexyldecanoic acid) can be explained by the existence of a domain separation of the organic ligands at the nanocrystal surface.

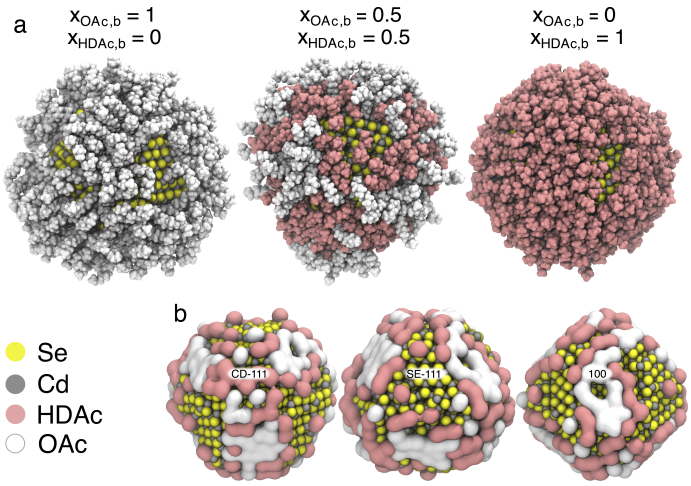

Figure 6.7: a) Distribution of the ligands on the surface for $x_{\mathrm{HDAc,b}} = 0, 0.5$ and 1. Oleates are shown in grey, 2-hexyldecanoates in pink. Carboxylate groups are shown, their position averaged over the last 15 ns of the final simulations at room temperature. b) Distribution of the ligands on the surface for $x_{\mathrm{HDAc,b}} = 0.5$ for the Cd-rich (111), Se-rich (111) and the (100) factes.

6.4 Conclusion

The ligand shell composition of the model system CdSe/oleate was studied by NMR spectroscopy and Classical Molecular Dysnamics simulations when a second carboxylic acid was added. First, a one-for-one exchange is observed between two ligands that can be monitored separately by NMR spectroscopy, oleic acid and 1-undecenoic acid. For single chain carboxylic acid systems, oleic acid/myristic acid, oleic acid/1-undecenoic acid and oleic acid/nonanoic acid, it was found that the composition of the ligand shell mimics the overall fraction of the acids in solution.

A different observation is made when a branched carboxylic acid is added to the CdSe/oleate dispersion. For 2-hexyldecanoic acid we found that only 22% of the oleates can be replaced, even when adding a huge excess of the branched carboxylic acid. This is attributed to the one-for-one exchange in combination with the larger volume of the branched carboxylic acid. Classical Molecular Dysnamics simulations help us to understand the origin of this behavior. The simulations show that there are pure oleate sub-domains on the 100 facets, mixed sub-domains (oleic acid/2-hexyldecanoic acid) on the Cd-(111) facets, whereas edges and the Se-(111) facets are covered with mainly 2-hexyldecanoate ions. All results provided by simulations strongly suggest that the experimental low exchange rates of branched ligands (2-hexyldecanoic acid) can be explained by the existence of a domain separation of the organic ligands at the nanocrystal surface.

This study confirms that binary ligand shells can be accomplished by simply adding a ligand mixture with desired composition to the nanocrystal dispersion when working with single chain carboxylic acids. However, for more voluminous ligands, this study proves that obtaining a mixed ligand shell is not that straightforward. Hence, it stresses the importance of the miscibility of the bound and the exchanging species in designing an efficient ligand exchange reaction.

6.A Oleic Acid / Branched Carboxylic Acid Replacement: Exchange equilibrium

In this section, Equation 6.6 on page 140 will be derived. Therefore, a number of parameters are defined in Table 6.1.

Table 6.1: Parameters for derrivation of Equation 6.6.

N_0	number of sites ($= N_{OAc,0} + N_{V,0}$)
N_{acid}	number of acid molecules ($= N_{OAc} + N_V$)
N_{OAc}	number of oleic acid molecules
$N_{OAc,b}$	number of sites occupied by oleic acid
$N_{OAc,f}$	number of free oleic acid molecules
$N_{OAc,0}$	number of sites occupied by oleic acid at the start
$N_{V,b}$	number of unoccupied sites
$N_{V,0}$	number of unoccupied sites at the start
$N_{HDAc,b}$	number of sites occupied by 2-hexyldecanoic acid
$N_{HDAc,f}$	number of free 2-hexyldecanoic acid molecules
$N_{HDAc,0}$	number of sites occupied by 2-hexyldecanoic acid at the start
N_{HDAc}	number of 2-hexyldecanoic acid molecules
Δ	the density of originally empty lattice sites ($= \frac{N_{V,0}}{N_{OA,0}}$)
$\nu_{HDAc,b}$	number of sites occupied by one HDAc
$\nu_{OAc,b}$	number of sites occupied by one OA
ϕ_{HDAc}	volume fraction HDAc $= \frac{N_{HDAc}\,\nu_{HDAc}}{N_{HDAc}\,\nu_{HDAc} + N_{OAc}\,\nu_{OAc}}$
x_{HDAc}	fraction of HDAc

Assuming that bound 2-hexyldecanoate occupies 2 lattice sites, we can than rewrite the oleic acid/2-hexyldecanoic acid exchange as a reaction in which

bound oleate and a free site are exchanged for bound 2-hexyldecanoate as shown in Section 6.3.3:

$$\mathrm{OAc}_b + \mathrm{HDAc}_f + \bigcirc \rightleftharpoons \mathrm{HDAc}_b + \mathrm{OAc}_f \tag{6.7}$$

For this reaction, a mass balance can be composed, whit the extend of the reaction α ($0 < \alpha < V_0$):

	$N_{HDAc,f}$	$N_{OAc,b}$	N_V	$N_{HDAc,b}$	$N_{OAc,f}$
0	N_{HDAc,f_0}	N_{OAc,b_0}	N_{V_0}	0	0
α	$N_{HDAc,f_0} - \alpha$	$N_{OAc,b_0} - \alpha$	$N_{V_0} - \alpha$	α	α

If we use mole fractions for activities, the exchange equilibrium of Equation 6.7 can be expressed by:

$$K = \frac{N_{OAc,f}}{N_{HDAc,f}} \; \frac{\phi_{HDAc,b}}{\phi_{OAc,b}(\frac{\phi_V}{N_0})^{\nu_{HDAc,b}-1}} \tag{6.8}$$

Since ν_{HDAc} equals 2, and the volume fractions can be rewritten in function of the number of molecules and the amount of sites they occupy, equation 10 can be rewritten as:

$$\frac{K}{N_0} = \frac{N_{OAc,f}}{N_{HDAc,f}} \; \frac{\nu_{HDAc,b}\; N_{HDAc,b}}{\nu_{OAc,b}\; N_{OAc,b}\; \nu_V\; N_V} \tag{6.9}$$

The mass balance at the extend of the reaction α can be inserted:

$$\frac{K}{N_0} = \frac{\alpha^2 \nu_{HDAc}^2}{(N_{HDAc,0} - \alpha)\; (N_{OAc,0} - \alpha)\; (N_{V,0} - \alpha)} \tag{6.10}$$

If we now estimate that $\alpha <<< N_{HDAc,0}$ and $\alpha <<< N_{OAc,0}$, then:

$$\frac{K}{N_0} = \frac{\alpha^2 \nu_{HDAc}^2}{N_{HDAc,0}\; N_{OAc,0}\; (N_{V,0} - \alpha)} \tag{6.11}$$

$N_{HDAc,0}$ can be replaced by $x_{\mathrm{HDAc}} N_{acid}$ and $N_{OAc,0}$ by $(1 - x_{\mathrm{HDAc}}) N_{acid}$:

$$\frac{K\; N_{acid}^2}{N_0} = \frac{\nu_X\; x_{\mathrm{HDAc,b}}^2\; N_{OAc,0}^2}{x_{\mathrm{HDAc}}(1 - x_{\mathrm{HDAc}})\; (N_{V,0} - x_{\mathrm{HDAc,b}} N_{OAc,0})} \tag{6.12}$$

Dividing both lids by $N_{OAc,0}$, rearranging Equation 6.12 and replacing $\frac{N_{V,0}}{N_{OAc,0}}$ by Δ, the density of originally empty lattice sites, gives us:

$$\frac{K\; N_{acid}^2}{N_0\; N_{OAc,0}} = \nu_X\; \frac{x_{\mathrm{HDAc,b}}^2}{\Delta - x_{\mathrm{HDAc,b}}} \tag{6.13}$$

Since N_{acid} equals $\frac{N_{OAc,0}}{1 - x_{\mathrm{HDAc}}}$, Equation 6.13 can be rewritten as:

$$K \frac{N_{OAc,0}}{N_0} \frac{x_{\mathrm{HDAc}}}{1 - x_{\mathrm{HDAc}}} = \nu_X \frac{x^2_{\mathrm{HDAc,b}}}{\Delta - x_{\mathrm{HDAc,b}}} \tag{6.14}$$

The fraction $\frac{N_{OAc,0}}{N_0}$ can now be replaced by Δ, the density of originally empty lattice sites.

$$K \frac{1 - \Delta}{\nu_X} \frac{x_{\mathrm{HDAc}}}{1 - x_{\mathrm{HDAc}}} = \frac{x^2_{\mathrm{HDAc,b}}}{\Delta - x_{\mathrm{HDAc,b}}} \tag{6.15}$$

and $K\frac{1 - \Delta}{\nu_X}$ can be replaced by K'

$$K' \frac{x_{\mathrm{HDAc}}}{1 - x_{\mathrm{HDAc}}} = \frac{x_{\mathrm{HDAc,b}}}{\Delta - x_{\mathrm{HDAc,b}}} \tag{6.16}$$

This equation can be rewritten it in the form of a quadratic equation:

$$(1 - x_{\mathrm{HDAc}})\, x^2_{\mathrm{HDAc,b}} + K' x_{\mathrm{HDAc}}\, x_{\mathrm{HDAc,b}} - \Delta K' x_{\mathrm{HDAc}} = 0 \tag{6.17}$$

The solution to this quadratic equation in $x_{\mathrm{HDAc,b}}$ is:

$$x_{\mathrm{HDAc,b}} = \frac{-K' x_{\mathrm{HDAc}} - \sqrt{K'^2 x^2_{\mathrm{HDAc}} + 4\Delta K' x_{\mathrm{HDAc}}(1 - x_{\mathrm{HDAc}})}}{2(1 - x_{\mathrm{HDAc}})} \tag{6.18}$$

This is Equation 6.6 on page 140 in Section 6.3.3.

References

[1] Y. Yin and A. P. Alivisatos. *Colloidal Nanocrystal Synthesis and the Organic-Inorganic Interface.* Nature, 437(7059):664–670, 2005.

[2] Maksym V Kovalenko, Liberato Manna, Andreu Cabot, Zeger Hens, Dmitri V Talapin, Cherie R Kagan, Victor I Klimov, Andrey L Rogach, Peter Reiss, Delia J Milliron, Philippe Guyot-Sionnnest, Gerasimos Konstantatos, Wolfgang J Parak, Taeghwan Hyeon, Brian A Korgel, Christopher B Murray, and Wolfgang Heiss. *Prospects of Nanoscience with Nanocrystals.* ACS Nano, 9(2):1012–1057, 2015.

[3] Sofie Abe, Richard K. Capek, Bram De Geyter, and Zeger Hens. *Reaction Chemistry/Nanocrystal Property Relations in the Hot Injection Synthesis, the Role of the Solute Solubility.* ACS Nano, 7(2):943–949, 2013.

[4] Kim De Nolf, Richard K. Capek, Sofie Abe, Michael Sluydts, Youngjin Jang, Jose C. Martins, Stefaan Cottenier, Efrat Lifshitz, and Zeger Hens. *Controlling the Size of Hot Injection Made Nanocrystals by Manipulating the Diffusion Coefficient of the Solute.* Journal of the American Chemical Society, 137(7):2495–2505, 2015.

[5] Xiaogang Peng, Liberato Manna, Weidong Yang, Juanita Wickham, Erik Scher, Andreas Kadavanich, and Paul Alivisatos. *Shape control of CdSe nanocrystals.* Nature, 404(6773):59–61, 2000.

[6] Luigi Carbone, Concetta Nobile, Milena De Giorgi, Fabio Delia Sala, Giovanni Morello, Pierpaolo Pompa, Martin Hytch, Etienne Snoeck, Angela Fiore, Isabella R. Franchini, Monica Nadasan, Albert F. Silvestre, Letizia Chiodo, Stefan Kudera, Roberto Cingolani, Roman Krahne, and Liberato Manna. *Synthesis and Micrometer-Scale Assembly of Colloidal CdSe/CdS Nanorods Prepared by a Seeded Growth Approach.* Nano Letters, 7(10):2942–2950, 2007.

[7] Tae-Ho Kim, Kyung-Sang Cho, Eun Kyung Lee, Sang Jin Lee, Jungseok Chae, Jung Woo Kim, Do Hwan Kim, Jang-Yeon Kwon, Gehan AMaratunga, Sang Yoon Lee, Byoung Lyong Choi, Young Kuk, Jong Min Kim, and Kinam Kim. *Full-Colour Quantum Dot Displays Fabricated by Transfer Printing.* Nature Photonics, 5(3):176–182, 2011.

[8] Chia-Hao M. Chuang, Patrick R. Brown, Vladimir Bulovic, and Moungi G. Bawendi. *Improved performance and stability in quantum dot solar cells through band alignment engineering.* Nature Materials, 13(8):796–801, 2014.

[9] Gerasimos Konstantatos and Edward H. Sargent. *Nanostructured materials for photon detection.* Nature Nanotechnology, 5(12), 2010.

[10] Krishnendu Saha, Sarit S. Agasti, Chaekyu Kim, Xiaoning Li, and Vincent M. Rotello. *Gold Nanoparticles in Chemical and Biological Sensing.* Chemical Reviews, 112(5):2739–2779, 2012.

[11] Jonathan De Roo, Isabel Van Driessche, José C. Martins, and Zeger Hens. *Colloidal Metal Oxide Nanocrystal Catalysis by Sustained Chemically Driven Ligand Displacement.* Nature Materials, 15():517–521, 2016.

[12] Yu Yang, Haiyan Qin, Maowei Jiang, Long Lin, Tao Fu, Xingliang Dai, Zhenxing Zhang, Yuan Niu, Hujia Cao, Yizheng Jin, Fei Zhao, and Xiaogang Peng. *Entropic Ligands for Nanocrystals: From Unexpected Solution Properties to Outstanding Processability.* Nano Letters, 16(4):2133–2138, 2016.

[13] Jong-Soo Lee, Maksyn V. Kovalenko, Jing Huang, Dae Sung Chung, and Dmitri V. Talapin. *Band-like transport, high electron mobility and high photoconductivity in all-inorganic nanocrystal arrays.* Nature Nanotechnology, 6(6):348–352, 2011.

[14] Patrick R. Brown, Donghun Kim, Richard R. Lunt, Ni Zhao, Moungi G. Bawendi, Jeffrey C. Grossman, and Vladimir Bulovic. *Energy Level Modification in Lead Sulfide Quantum Dot Thin Films through Ligand Exchange.* ACS Nano, 8(6):5863–5872, 2014.

[15] Chia-Hao M. Chuang, Patrick R. Brown, Vladimir Bulovic, and Moungi G. Bawendi. *Improved performance and stability in quantum dot solar cells through band alignment engineering.* Nat. Mater., 13(8):796–801, 2014.

[16] Allen Templeton, W. Peter Wuelfing, and Royce W. Murray. *Monolayer Protected Cluster Molecules.* Accounts of Chemical Research, 33(1):27–36, 2000.

[17] Frank Schreiber. *Structure and Growth of Self-Assembling Monolayers.* Progress in Surface Science, 65(5-8):151–256, 2000.

[18] Thomas Buergi. *Properties of the Gold-Sulphur Interface: from Self-Assembled Monolayers to Clusters.* Nanoscale, 7(38):15553–15567, 2015.

[19] Stephan J. Stranick, A. N. Parikh, Ye Tao, D. L. Allara, and Paul S. Weiss. *Phase Separation of Mixed-Composition Self-Assembled Monolayers into Nanometer Scale Molecular Domains.* Journal of Physical Chemistry, 98(31):7636–7646, 1994.

[20] Alicia M. Jackson, Jacob W. Myerson, and Francesco Stellacci. *Spontaneous Assembly of Subnanometre-Ordered Domains in the Ligand Shell of Monolayer-Protected Nanoparticles.* Nature Materials, 3(5):330–336, 2004.

[21] Quy Khac Ong, Javier Reguera, Paulo Jacob Silva, Mauro Moglianetti, Kellen Harkness, Maria Longobardi, Kunal S. Mali, Christoph Renner, Steven De Feyter, and Francesco Stellacci. *High-Resolution Scanning Tunneling Microscopy Characterization of Mixed Monolayer Protected Gold Nanoparticles.* ACS Nano, 7(10):8529–8539, 2013.

[22] Claire Vilain, Frederic Goettmann, Audrey Moores, Pascal Le Floch, and Clement Sanchez. *Study of Metal Nanoparticles Stabilised by Mixed Ligand Shell: a Striking Blue Shift of the Surface-Plasmon Band Evidencing the Formation of Janus Nanoparticles.* Journal of Materials Chemistry, 17(33):3509–3514, 2007.

[23] Bernd Fritzinger, Richard K. Capek, Karel Lambert, José C. Martins, and Zeger Hens. *Utilizing Self-Exchange To Address the Binding of Carboxylic Acid Ligands to CdSe Quantum Dots.* Journal of the American Chemical Society, 132(29):10195–10201, 2010.

[24] Raquel Gomes, Antti Hassinen, Agnieszka Szczygiel, Qiang Zhao, Andre Vantomme, Jose C. Martins, and Zeger Hens. *Binding of Phosphonic Acids to CdSe Quantum Dots: A Solution NMR Study.* Journal of Physical Cemistry Letters, 2(3):145–152, 2011.

[25] Ashley M. Smith, Lauren E. Marbella, Kathryn A. Johnston, Michael J. Hartmann, Scott E. Crawford, Lisa M. Kozycz, Dwight S. Seferos, and Jill E. Millstone. *Quantitative Analysis of Thiolated Ligand Exchange on Gold Nanoparticles Monitored by ^{1}H NMR Spectroscopy.* Analytical Chemistry, 87(5):2771–2778, 2015.

[26] Jacek Jasieniak, Craig Bullen, Joel van Embden, and Paul Mulvaney. *Phosphine-Free Synthesis of CdSe Nanocrystals.* Journal of Physical Cemistry B, 109(44):20665–20668, 2005.

[27] Marco Cirillo, Filip Strubbe, Kristiaan Neyts, and Zeger Hens. *Thermal Charging of Colloidal Quantum Dots in Apolar Solvents: a Current Transient Analysis.* ACS Nano, 5(2):1345–1352, 2011.

7

Overall Conclusion

7.1 Synthesis Kinetics and reaction mechanism

The transition of a *black box synthesis* to actually understanding the synthesis mechanism and its kinetics is of key importance for the production of new materials or the path towards cheaper and better synthesis routes for already existing materials. This type of research can accelerate the process towards the implementation of materials in various applications. In the first chapter, the reaction of aminophosphines and indium halides to form InP nanoparticles was studied. This reaction is not straightforward due to the oxidation states of the indium and phosphorous. The reaction of In^{III} and P^{III} has to be preceded by a reduction of P^{III} to P^{-III}. First, it was proven by single crystal XRD and NMR spectroscopy that the aminophosphine undergoes a transamination reaction, whereby the diethylamino groups are substituted for the amine used as a solvent. The InP synthesis reached full yield with respect to indium when the ratio between the aminophosphine and the indium halide was 4:1. Furthermore, NMR measurements of aliquots taken during the synthesis revealed the formation of a byproduct. This byproduct was formed at the same rate as the InP formation. It was

isolated and identified by means of mass spectrometry and NMR as being a fully transaminated phosphonium salt. This was in perfect agreement with the earlier established ratio between the the aminophosphine and the indium halide to obtain full yield. Hence, a reaction equation was formulated:

$$InX_3 + 4\,P(NHR)_3 \rightleftharpoons InP + 3\,P(NHR)_4X \tag{7.1}$$

In this reaction, one aminophosphine is used to form the InP unit and is reduced from P^{III} to P^{-III}. The three remaining aminophosphines serve as reducing agents and are thus transformed into phosphonium salts (P^{V}). These findings can be used to produce other III-V materials such as InAs or InSb via this relatively cheap synthesis route. In turn, it can lead to the integration of quantum dots into various applications.

Synthesis kinetics is another subject that is underestimated too often. Such studies render an understanding about what happens during the synthesis and what factors, even if they might seem trivial at first sight, are the key to obtain the best end result. The second chapter dealt with understanding the role of the ligand chain length in CdSe nanocrystal synthesis. First, the observation that particles obtained at the end of the reaction increase in size with decreasing chain length of the carboxylic acid used as a ligand was confirmed for two synthesis methods. Importantly, the reaction rate was equal for all experiments. We therefore attributed the observed size tuning to a change of the moment where nanocrystal nucleation is overtaken by nanocrystal growth. Subsequently, the influence of the chain length on the parameters in the equations for nucleation and growth was studied by means of well thought experiments. It was proven that the diffusion coefficient of the solute is determined by the chain length while the surface tension and the rate constant for solute adsorption are not. Since the diffusion coefficient of the monomer plays a very similar role as the monomer solubility in the nucleation and growth equation, the increase of d_{NC} most likely resulted from the joint increase of the diffusion coefficient and the solubility of the solute when reducing the chain length of the carboxylic acids. These findings demonstrated that a change in diameter will occur only if the ligands interact to some extent with the solute - either through direct (inner sphere) or a more loose (outer sphere) coordination. Finally, the chain length of other additives like amines and phosphine oxides was altered. Especially in the case of amines, the ligand chain length had no noticeable effect on d_{NC}. This suggested little interaction with the solute, which is in line with the weak, dynamic stabilization of CdSe nanocrystals by amines. Hence, this study showed that changing the ligand chain length provides a practical way to tune the nanocrystal diameter at full yield in a hot injection synthesis and enhance the size dispersion. This is key to the

application of nanocrystals as light emitters, for example in display applications. On the other hand, the ligand chain length can now be used to probe the interaction between a reaction additive and the solute, which can lead to better insight in the hot injection synthesis itself.

7.2 Surface chemistry

The surface chemistry is enormously important for quantum dots - and nanocrystals in general - to be used in applications. Although a lot of research has already been conducted, there are always more challenges to be overcome. For example, little is know about the arrangement of the ligands across different facets of the nanocrystal surface. In the third chapter the surface chemistry of CdSe and PbSe nanocrystals capped with oleate ligands was studied by means of spectral hole burning experiments targeting the alkene resonance. For both systems, a prominent hole was observed, signifying that the NMR resonances of oleate ligands are heterogeneously broadened. Variation of the hole burning position indicated that the alkene resonance consisted of a manifold of resonances. A clear difference between PbSe and CdSe was observed by executing hole burning recovery experiments. The PbSe quantum dots clearly consisted of two (or more) submanifolds. The irradiation spread within each submanifold yet little or no transfer of saturation occurred between the two submanifolds. However, both submanifolds displayed very similar recovery behavior. We related the submanifolds to two types of facets with very similar ligand densities. For the CdSe sample, the spectral hole changed shape during the recovery. It was found that the CdSe nanocrystals exhibited two submanifolds with a clear difference between the submanifolds. One of the submanifolds behaved similar to the PbSe submanifolds. The saturation transfer in the second submanifold was almost entirely absent. In line with our conclusions in the case of PbSe QDs and the classical molecular dynamics simulations, the broad resonance could be attributed to ligands bound to a densely packed crystal facet ((100) facet). Attributing the second is more speculative. It could either correspond to oleate ligands bound to the edges or the center of the Cd-rich(111) facets or both. In either case, surface curvature or lower ligand densities can indeed enhance the solvation of ligands, thus creating the range of more homogeneous chemical environments that is needed to explain the experimental observations. The combination of experiment and simulations provided useful information about the arrangement of ligands on the nanocrystal surface. This can offer more insights when ligand shell modifications are necessary.

In the last chapter, the surface chemistry of binary ligand shells was studied. CdSe nanocrystals capped with oleate ligands were used as starting material for every experiment. When a single chain carboxylic acid was added to the dispersion, the composition of the ligand shell mimicked the overall composition of the acids in solution. A one-for-one exchange was observed between two ligands that can be monitored separately by NMR spectroscopy, oleic acid and 1-undecenoic acid. For three single chain carboxylic acid systems, OAc/MAc, OAc/UAc and OAc/NAc, it was found that the ligand shell composition equals that of the dispersion. For example, when one equivalent of myristic acid is added to a CdSe/OA dispersion, the ligand shell will contain equal amounts of oleate and myristate. A different observation was made when a branched carboxylic acid was added to the CdSe/OA dispersion. For 2-hexyldecanoic acid we found that only a small part of the oleates can be replaced, even when adding a huge excess of the branched carboxylic acid. This was attributed to the tit-for-tat exchange in combination with the larger volume of the branched carboxylic acid. Simulations performed by the group of Ivan Infante at the VU Amsterdam helped us to understand the origin of this behavior. First, a simulation was performed to check if all branched carboxylic acids have enough space to bind to the nanocrystal surface. Indeed, the simulation shows that complete coverage of the nanocrystal by 2-hexyldecanoates is sterically allowed. Subsequently, simulations have been performed at a different HDAc fractions $x_{\mathrm{HDAc,b}}$. It shows that oleates mostly occupy (100) facets, creating very compact, almost pure sub-domains. In addition, sub-domains of mixed composition (OAc/HDAc) are usually found at the Cd-(111) facets, whereas edges and the Se-(111) facets are covered with mainly 2-hexyldecanoates. Phase separation appears as being favored both enthalpically, due to better intermolecular interactions, and entropically, because of the greater mobility of oleate in the homogeneous phase. All results provided by simulations strongly suggest that the experimental low exchange of branched ligands (HDAc) can be explained by the existence of a domain separation of the organic ligands at the nanocrystal surface. This study confirms that binary ligand shells can be accomplished by simply adding a ligand mixture with desired composition to the nanocrystal dispersion when working with single chain carboxylic acids. However, for more voluminous ligands, this study proves that obtaining a mixed ligand shell is not that straightforward. Hence, it stresses the importance of the miscibility of the bound and the exchanging species in designing an efficient ligand exchange reaction.

In conclusion, diverse research topics in the field of synthesis and characterization of quantum dots were studied, leading to an overall better understanding of a variety of quantum dot syntheses. NMR spectroscopy was the

main research technique used throughout this phD work. It stresses the importance of this elaborate technique. 20 years after its introduction in the nanocrystal field, new NMR techniques are continuously being developed specifically for nanocrystal research, introducing new insights in the surface chemistry.

7.3 perspectives

In the past four years, my research has contributed to a better understanding of the nanocrystals which is crucial to obtain commercially available applications for nanocrystals. The CdSe quantum dots have become a model system to study all kinds of reaction chemistry/nanocrystal properties relations like the study of the influence of the ligand chain length on the nanocrystal size and size dispersion in the fourth chapter. However, strict regulations on the use of cadmium in commercial devices has lead a trending evolution towards the use of less toxic and more sustainable nanocrystals. Concepts, explained in this thesis, could be easily extended towards these novel generations of heavy-metal free quantum dots.

NMR spectroscopy was the main research technique used throughout this PhD work and its limits are definitely not reached yet. Numerous studies could still be performed to obtain insights in the surface chemistry of the novel generation nanocrystals and to study ligand exchanges. The option to alter the temperature at which the NMR measurement is conducted could give us information about the stability of the nanocrystals at elevated temperatures and it could, for example, visualize why some ligand exchanges are only happening at higher temperatures. The NMR studies explained in chapter five and six could be expanded to nanocrystal platelets since they have larger uniform facets, which could lead to interesting conclusions.

The future and possible applications of this work - and quantum dots in general - depends on the economical feasibility of the production of nanocrystals. Therefore, we need to obtain cheaper syntheses which are easily scalable to larger volumes. Replacement of expensive precursors such as like tris(trimethylsilyl)phosphine by aminophosphines has been a vital and necessary step towards the synthesis of cost-efficient InP quantum dots. However, there is still room for improvement as an excess of phosphorous precursor makes for a higher reagent cost. This issue can, for example, be solved by incorporation of an additional reducing agent. Since we elucidated the InP mechanism, the production of other III-V materials such as InAs or InSb could be achieved via this relatively cheap synthesis route. This can lead to the integration of quantum dots into various applications.

I know that I don't wanna know
Who I am without you

-

Bear's Den

A

Acknowledgements

Aan allen die mijn doctoraatsthesis volledig gelezen hebben: proficiat.
Aan allen die enkel het dankwoord gelezen hebben: ook proficiat.

Since this will be the most read part of my thesis, I started writing it more than one year ago and it is also the last part to be finished. Doing a PhD is something you cannot do by yourself. You need a big team around you. And I was lucky to have such a team. Without a promotor, one cannot start a PhD and I can assure you, you can also not finish it without. I was lucky to have two promotors. They both helped me in their own way, complementary to each other. Zeger always had a(n) (funny) answer ready to any of my (scientific) questions and we had nice discussions. I am still grateful he accepted me, first as a master thesis student - even without that being an incredible success - and later as a PhD student. José was always ready to help me with any NMR problem. Of course, without the necessary funding, this PhD would not have been possible. Therefore, I would like to thank FWO as well.

I want to thank all PCN'ers for being amazing colleagues and many of you also great friends. Already from the start, I was immediately part of the

crew. Thanks to Marco, Sofietje, Pieter G., Pieter A. (you could have been defending a thesis yourself!), Antti and Yolanda for that. I also want to thank Antti for teaching me 'how to NMR' and Sofie for guiding me with everything else as godmother. Of course people leave the group and new ones arrive. This brings me to Kishu and Daniel, I liked hanging out with you guys a lot! Thank you Kishu for the nice cooperation on HgSe. Then Suzanne arrived as a shy girl, who turned out to be a great support and an AWESOME friend. Jonathan, thank you for your NMR insights and our discussions. Two years after I started, Emile, Willem and Jorick joined the group and before I knew it the concept of the 'cool', 'sick' and 'fun' office was introduced.

Emile, you were always my favorite person in the fun office. It was nice to share the NMR work with you. Pieter G., thanks to you I understand concepts as gain and stimulated emission. Shalini, Igor, Renu and Natalia, although I don't know all of you that well, you are all nice additions to our group.

Mickael and Dorian, without you guys there would be no such thing as the sick office. Thanks for sharing beers with me during our Thursday drinks and thanks for the nice cooperation for the work on the InP synthesis mechanism. I hope this can be continued in some way. My dear Chen, thanks for all the gifts from China and the friendship. Kishu, you rock! Arnau, I know we didn't have a great start but I think that is all in the past now.

I couldn't have been more grateful with the cool office crew. Valeriia, you are a very nice person. I like doing NMR work with you. Thanks to Suzanne for being my friend, for listening when I needed it the most, for the trips we have made together. Even though your research is not really related to mine, you were always willing to help me overcome (little) struggles. Willem, thanks for taking the desk right in front of me, imagine what would have happened if you wouldn't have. Thanks for socializing and I am grateful for all your efforts at the TEM as well. Jorick, thanks for all the fun, the laughter. You're not only a good friend by now but also a great colleague. It was a pleasure working with you. Yolanda, you helped me so much during highs and lows. On top of that it was so nice to work with you because whatever we did together, we would complement each other perfectly. Thanks for being such a good friend, even when we are not working together. And now I can't even remember how it was before I've met these people, thanks to all PCN'ers, including our thesis students (Pieter S., Hannes and Wally).

The NMR group means a lot to me too. Freya, without you I would still

doubt what settings I need to use in an NMR experiment. Thanks for all the chats we had and making S4 a nice place to work. Tim, thank you for answering the million questions I had (Tiiiiiiiiiim, mag ik iets vragen???) and Dieter and Niels, to answer the other million questions when I couldn't locate Tim. Thanks to Krizstina for being interested in my work and helping me with some experiments. Davy, thank you for helping me with the ^{31}P measurements. Also a big thanks to all other (former) NMRSTR members.

I was very lucky to share an FWO project with Michael Sluydts. Otherwise I would have had to do my own simulations. Big thanks Michael. In that respect I also have to thank Salvatore and Ivan. The simulations you did are awesome! Thanks to Emory for supervising me when I was in Berkeley. Pieter Surmont and Jan Goeman, thanks for all the MS measurements. I am grateful to Katrien H. to analyze all my TEM samples. Thanks to all other members of the departement like Katrien D.K., Els, Hannes, Ward and Isabelle for being such nice colleagues.

Thanks to all the people who helped me in some way with writing my dissertation. Suzanne, thanks for reading parts, helping me decide which colors to use, ect. Jorick, thanks for your valued opinion as well. Willem, thanks for the translations. Shalini, thanks for reading my introduction when I was too scared to send it to Zeger. Sofie Van Damme, thanks for the comments on the Dutch summary. Sofie Abé and Jonathan, thanks for the figures you provided. Pieter S., thanks for your suggestions. Zeger and José, thanks for the extensive comments and help. Thanks to all others for supporting and enduring me when I was stressed.

Next to scientific work there was always administrative work to be done too. There I have to thank An, Pierre, Kathleen and Claudine for helping me with everything. Bart and Pat, thank you for fixing all my issues with computers, glove boxes, etc. Thanks to Chokry and the entire cleaning team for keeping my work space *spick-and-span*. Last but not least, thanks to all the resto ladies and gentlemen for feeding me every day (especially on Wednesdays when there was SPAGHETTI!).

Zonder plezier in het leven is een doctoraat afwerken onmogelijk. Bedankt aan de drie dames die al ruim 25 jaar mijn vriendinnen zijn. Ine, Wibe en Wendy, ik kan jullie niet wegdenken uit mijn leven. Lieve vriendjes van de chemie (Debbie, Isabelle♡, Laura, Sophie, Bart, Jonathan, Matthias, Maxime, Nick, Nelson, Nicolas, Pieter en Wannes), jullie zijn ondertussen al mijn trouwe vrienden sinds 2007. Bedankt voor alle etentjes, feestjes en reisjes die we samen maakten. Bedankt aan Sara en Sophie voor de onvergetelijke momenten.

Familie, Bedankt om er te zijn voor mij. Nu al ruim 27 jaar zijn jullie er altijd voor me. Mama, bedankt om me vrij te laten in alle keuzes die ik al moeten maken heb. Saar, dank je om plezier te maken met me. Dank je voor de reizen die we al samen hebben gemaakt (in binnen-en buitenand, letterlijk en figuurlijk). Sas, Noa, Fee en Birger jullie zijn een topgezinnetje in onze familie. Dank je voor alle liefde die ik al van jullie gekregen heb. Lo mismo vale para Akim, Karla, Mali y Alec, están en mi corazón! Bedankt Dirk, voor alle duwtjes in de juiste richting. Dank je aan de tantes en nonkels voor alle steun en warmte. Bedankt aan mijn Cactus familie en vrienden voor de leuke momenten. Marieke, bedankt om mijn *big sis* te zijn. Zef, Bedankt om me te steunen tijdens onze 5 jaar.

Bedankt voor alles.

Gent, September 2016
Kim De Nolf